Summer 8-5-2013

# Dynamic Electron Control using Light and Nanostructure

Wayne Cheng-Wei Huang
*University of Nebraska-Lincoln*, s-chuang2@unl.edu

# DYNAMIC ELECTRON CONTROL USING LIGHT AND NANOSTRUCTURE

by

Huang Cheng-Wei

A DISSERTATION

Presented to the Faculty of

The Graduate College at the University of Nebraska

In Partial Fulfilment of Requirements

For the Degree of Doctor of Philosophy

Major: Physics and Astronomy

Under the Supervision of Professor Herman Batelaan

Lincoln, Nebraska

August, 2013

DYNAMIC ELECTRON CONTROL USING LIGHT AND NANOSTRUCTURE

Huang Cheng-Wei, Ph.D.

University of Nebraska, 2013

Adviser: Herman Batelaan

The advent of nano-technology has made possible the manipulation of electron or light through nanostructures. For example, a nano-tip in near-field optical microscopy allows imaging beyond the diffraction limit, and a nano-fabricated hologram is used to produce electron vortex beam. While most schemes of electron control utilize only static components, dynamic electron beam control using both light and nanostructures has not yet been realized. In this dissertation, we explore this possibility and study the interplay between electron, light, and nanostructures. A understanding of such a system may facilitate dynamic electron beam control or even bring new insights to fundamental quantum mechanics.

The direct interaction between light and free electrons is weak, but the presence of nanostructures may modify the electron-light interaction in different ways. First, nanostructures may change a free electron's behavior by deforming the local vacuum field. When the electron's behavior is modified, its interaction with light could change too. Second, the illumination of light on nanostructures may give rise to induced surface charges or surface plasmon polaritons. The near-field of these charge structures could couple strongly with free electrons.

To learn about electron dynamics in the vacuum field, we start with a classical harmonic oscillator. When the oscillator is immersed in the vacuum field, its interaction with light could be modified. Our study shows that the harmonic oscillator exhibits an integer-spaced spectrum instead of a single resonance. On the other hand,

to study how induced surface charges could mediate interaction between light and free electrons, we illuminated different surfaces with a low-intensity laser. As an electron beam is brought close to a surface that is illuminated with light, electron deflection was observed. This is considered to be a preliminary study to the effect of light on the electrons in the presence of nanostructures.

The implications of our studies are as follows. First, coherent electron-beam splitting may be possible through using spatial-temporal light modes on nanostructures. Second, electron beams could be used to probe optically induced surface near-fields. Further studies in these directions seem promising and may result in interesting discoveries.

# DEDICATION

May all the glory be to the Lord God.

To my father Huang Ming-Hsien and my mother Chu Huey-Chen.

*By faith we understand that the worlds were prepared by the word of God, so that what is seen was not made out of things which are visible. (Hebrews 11:3)*

# PREFACE

- Chapter 1 is accepted by Journal of Computational Methods in Physics.
- Chapter 2 is submitted to Physical Review A.
- Chapter 3 is submitted to Journal of Physics D.
- Chapter 4 is published in Annalen der Physik [Ann. Phys. (Berlin) 524, 1 (2012)].

We gratefully acknowledge funding supports from the National Science Foundation.

# ACKNOWLEDGMENTS

*"In der Beschränkung zeigt sich der Meister."*

(*The master shows himself in his limitation.*)

My five-year doctoral study has been filled with adventures and excitement. At the same time, it has also been a humbling experiencing, expanding my scope as a scientist. As an apprentice under Prof. Batelaan, I have felt blessed to work in an environment where exciting discussions of physics never end. Thank you, Herman, for much inspiration and the mentorship that have helped me grow into maturity.

I would like to thank the members of my Ph.D. committee, who have been supportive of me in finishing my degree. Thank you, Prof. Herman Batelaan, Prof. Kees Uiterwaal, Prof. Brad Shadwick, Prof. Evgeny Tsymbal, Prof. David Swanson, and Prof. Timothy H. Boyer. I would like to give special thanks to Prof. Swanson and Prof. Shadwick. Prof. Swanson has been a strong support in helping me advance my supercomputing skills, while Prof. Shadwick has alway made time to have long conversations with me and give insightful advice.

I would like to thank all the faculty members of the physics department for making it a nourishing academic environment. Special thanks to Prof. Kirill Belashchenko, Prof. Ilya Fabrikant, Prof. Sy-Hwang Liou, Prof. Peter Dowben, Prof. Anthony Starace, Prof. Martin Centurion, and Prof. Timothy Gay for many physics discussions and practical advice that made my Ph.D. experience successful.

I would like to thank all the staff of the physics department. They have made the stressful life in academia much easier. Especially, I would like to warmly thank our

former department secretary, Kay Haley, for she has rescued my career at one of my most difficult times in life.

I would like to give thanks to the my fellow graduate students, who have helped and inspired me through graduate school. Thank you, Mu Sai, Joan Dreiling, Roger Bach, Scot McGregor, Maria Becker, Eric Jones, Peter Beierle, Kristin Kraemer, Yang Jie, Yin Xiaolu, Keisuke Fukutani, Shashi Poddar, Anil Kumar, Benjamin Hage, and Alex Stamm. I would also like to give special thanks to Mu Sai and Joan Dreiling. While Sai is always the first person I went to for physics helps, Joan's radiant personality has encouraged the graduate community and helped us keep our sanity. Special thanks to Dr. Adam Carprez, for his expertise in supercomputing that has enabled much of my research work.

I would like to give special thank to Dr. Diane Baxter of San Diego Supercomputing Center for unceasing encouragement, to Prof. Federico Capasso of Harvard University for giving support to our work on the plasmonic attenna and vacuum field physics, to Prof. Peter Milonni of Los Alamos National Laboratory for advice and encouragement.

I would like to thank my "family" in Lincoln Nebraska. Thank you, Dan and Angel Schiermann, Samuel and Patience Noonoo, Mike and Sherri Bossard, and Deb Stephens for much love and the memories. Also, special thanks to all the brothers and sisters at the International Student Fellowship, the Lincoln Berean Church, and the Lincoln Chinese Christian Church for being my supporting networks during these years.

Finally, I would like to thank my beloved family in Taiwan. Thank you, Dad, Mom, Amy, Johnny, and Jordan for accompanying me through my Ph.D. years. Your love and support has kept me going strong and enabled me to soar for a brighter future.

# Contents

# List of Figures

# Introduction to Dissertation

## 1. Research Motivation

Over the years, much progress has been made in the field of free electron control using microscopic structure. In 1961, Jönsson first demonstrated electron diffraction with micro-slits [1]. Then, Barwick *et al.* [2] used a nano-grating to obtain a high-quality electron interference pattern up to the 21st order. Verbeeck *et al.* [3] used a nano-hologram to produce electron vortex beams which is analogous to producing an optical vortex beams from micro-hologram. Recently, Bach *et al.* [4] used a movable mask to cover a double-slit and showed the transition between the double-slit and single-slit diffraction patterns. While static control of free electrons using material structures is a maturing field, dynamic control of free electrons using light has not made much progress. The major obstacle is the requirement for a high-intensity laser, as the direct interaction between light and free electrons is weak [5]. However, light affected by a material surface can behave much differently from that in free space, and the electron-light interaction there may be modified as well. In view of the rapid advancement of plasmonics and nanophotonics [6, 7, 8, 9], we envision dynamic electron control using both light and nanostructures.

With the presence of nanostuctures, the electron dynamics can be altered in two ways. First, the local vacuum field as deformed by nanostructures can change the

behavior of an electron [10, 11, 12, 13, 14, 15]. In the past decade, much interest was generated in measuring the Casimir force [15, 16, 17, 18, 19, 20, 21, 22, 23, 24]. As the Casimir force is a result of deforming the vacuum field with material boundaries, measurements of Casimir forces using micro- or nano-structures confirm that microscopic structures can cause enough deformation of the vacuum field to produce measurable effects. Thus, it may be reasonable to assume that the use of nanostructures changes the local vacuum field, and that electron dynamics near nanostructures, as well as its interaction with light could change accordingly. Second, nanostructures may obtain light-induced surface charge or surface plasmon polaritons when interacting with light. The near-field of these charge structures may affect the interaction with electrons. Thus, the problem of weak interaction between light and free electrons can perhaps be remedied by the use of the nanostructure.

## 2. Research Overview

In the first part of our study, we consider the interaction between electrons and the vacuum field. Here we use a classical theory as an approximation instead of the full quantum electrodynamics. The theoretical framework of electron-vacuum interaction was first formulated in 1947 right after the experimental discovery of the Lamb shift [10, 11]. While the discovery of the vacuum field marks a milestone in the development of fundamental quantum mechanics [25, 26], some also considered how classical mechanics should be modified under the constant disturbance of the omnipresent vacuum field [27, 28]. The classical theory that accounts for the vacuum field effect is generally known as stochastic electrodynamics (SED)[1]. Being a fully classical theory, SED does not employ any quantization condition and thus is expected

[1]This name is sometimes used interchangeably with random electrodynamics (RED).

to only approximate the quantum mechanical results. However, it has been shown in certain physical systems that SED reproduces the exact quantum mechanical results [29, 30, 31]. As SED accounts for the Casimir force correctly [32, 33, 34], it may be easier to approach our problem using this classical theory instead of the full quantum electrodynamics.

We started with examining the detailed dynamics of a classical harmonic oscillator in the vacuum field. Computer simulation is used to visualize the temporal evolution of the oscillator and study how the Gaussian probability distribution emerges. Especially, the relation between sequential and ensemble samplings is studied. We also use the harmonic oscillator to study how the vacuum field can change the electron-light interaction. The excitation spectrum of a classical harmonic oscillator is recorded with and without the vacuum field. The results are also compared with a quantum mechanical calculation.

The second part of our study is an experimental investigation of nanostructures' response to laser light. In one experiment, a surface of nano-grooves is illuminated with a low-power laser and compared to the behavior of a flat surface. We record the deflection of a free electron beam as it is brought near the surface. In another experiment, we use a femtosecond laser to probe the temporal response of a surface patterned with nano-rods. The cross-correlation signal of the input and reflected light is analyzed to infer the nano-rods' response time scale. We infer that the surface charge on the nano-rods can respond to the femtosecond laser promptly.

# 3. Research Highlights

There are four chapters in this dissertation, and each chapter corresponds to a research topic. The first two chapters are theoretical studies that deal with the inter-

action between the vacuum field and a classical harmonic oscillator. The last two chapters are experimental studies that investigate the interaction between light and nanostructures. The following presents the main results of each chapter.

## 3.1 Dynamics of a Classical Harmonic Oscillator in Vacuum Field

In Chapter 1, we acquaint ourselves with vacuum field physics using a test system of a classical harmonic oscillator. The numerical study focused on the visualization and the analysis of the trajectory (see Figure 1). In studying the trajectory, we looked for the underlying mechanism of the oscillator's Gaussian probability distribution. We found that the Gaussian probability distribution is formed from many classical double-peak probability distributions with different oscillating amplitudes. Oscillations that are at least one coherence time apart become weakly correlated, thus the sequential sampling gives the same result as the ensemble sampling. Collecting the various oscillation amplitudes at time points separated by several coherence time, the Gaussian probability distribution can be reconstructed from classical double-peak distributions.

## 3.2 Quantized Excitation Spectrum of a Classical Particle

Chapter 2 illustrates how electron-light interaction can be modified by the presence of vacuum field using the example of a driven harmonic oscillator. As a light pulse is shone on a harmonic oscillator, the excitation energy is recorded as a function of pulse frequency. In the absence of vacuum field, the classical excitation spectrum possesses a single resonance peak. With the presence of vacuum field, the excitation spectrum becomes integer-spaced and the peak heights agree with the quantum calculation (see

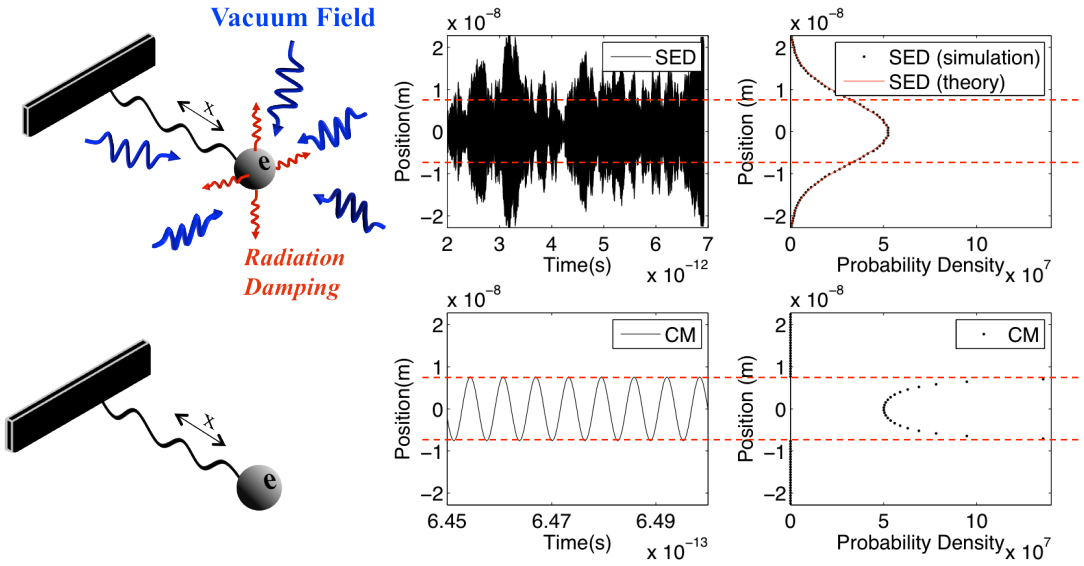


Figure 1: Trajectory and probability distribution of an harmonic oscillator with (top) and without (bottom) the perturbation from vacuum field.

Figure 2). A perturbation analysis is performed in addition to the numerical simulation, which confirms the underlying mechanism for the integer-spaced spectrum to be parametric resonance. The peak heights are determined by the ensemble statistics which are related to the details of the vacuum field.

## 3.3 Electron Deflection by Light-Induced Surface Near-Field

In Chapter 3, we turn to experimental studies of interaction between nanostructures and light. When a surface of nano-grooves is illuminated with light, the intensity gradient produces a surface charge pattern that mimics the beam shape. A free electron beam is brought close to the surface. As light is turned on, large deflection is observed. This deflection is much stronger than that through image charge [2]. The difference between the two deflection processes is shown by chopping the laser light (see Figure 3). The power of the laser used in the experiment is as low as several mW, so the direct interaction between laser and free electron is negligible.

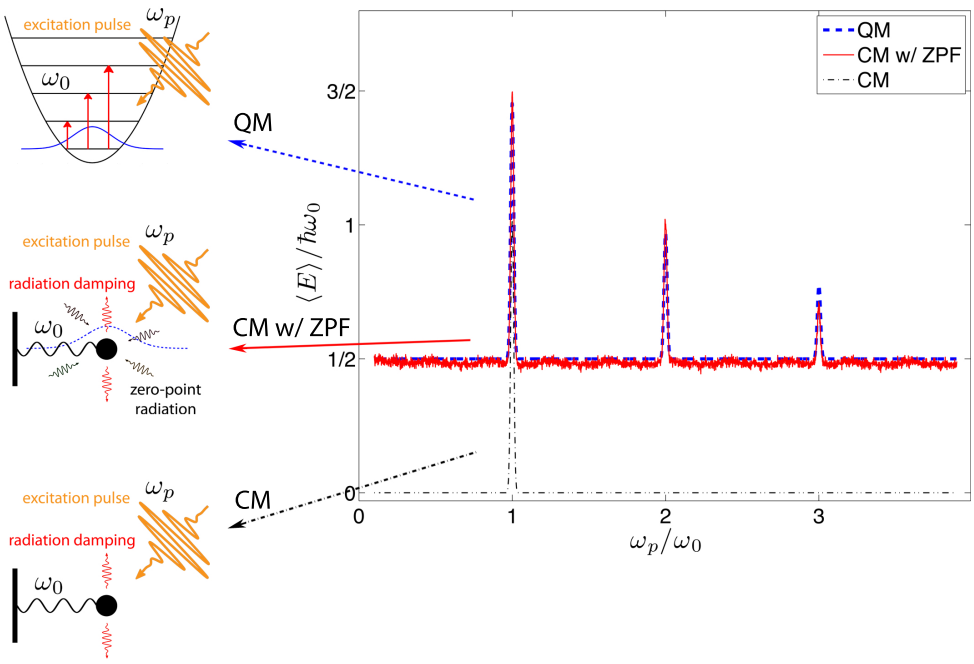


Figure 2: Excitation spectrum of a classical harmonic oscillator in vacuum field.

## 3.4 Ultrafast Temporal Response of a Plasmonic Structure

The optical response of a nanostructure is studied in Chapter 4. To determine how fast a nanostructure can respond to a driving field, a silicon nitride surface patterned with nano-rods is illuminated with a femtosecond laser pulse. We analyzed the cross-correlation signal of the input and the reflected light to infer the response time of the nanostructure (see Figure 4). It is found that the nanostructure responds promptly to the driving field. Although we do not know yet if the temporal response depends on the geometry or the size of the nanostructures, we speculate that ultrashort pulse may be used together with specially designed nanostructure to achieve ultrafast dynamic control of free electron.

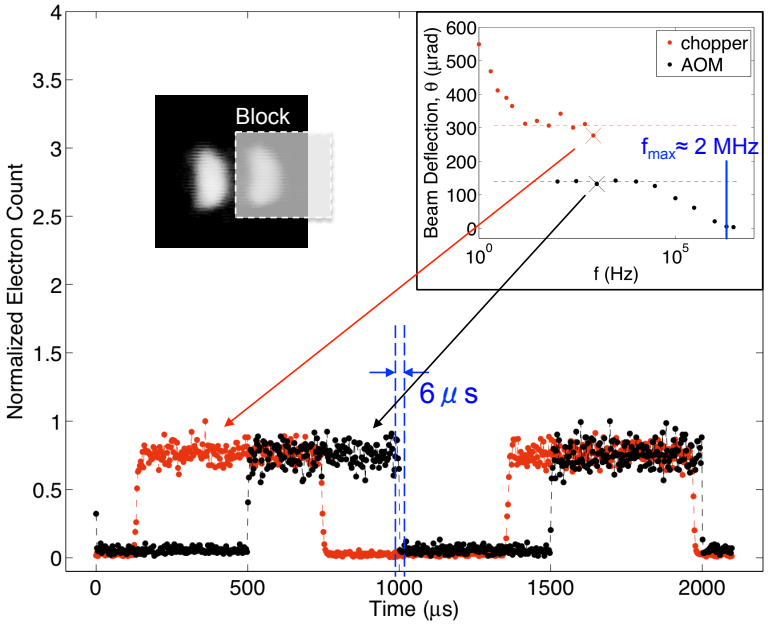


Figure 3: Electron deflection by a surface illuminated with low-intensity light.

# 3. Conclusions and Outlook

In our theoretical studies, we showed that vacuum field can play a major role in classical electron dynamics. Properties that are considered as intrinsic, such as excitation spectra or the uncertainty relation between position and momentum, may be subject to change when the vacuum field is modified. In our experimental studies, a surface was shown to cause significant deflection of free electron through an optically induced surface near-field. This may be seen as a precursor that motivates a study of dynamic electron control using light and nanostructures. We speculate that designed nanostructures and ultrashort light pulses may be used to achieve ultrafast dynamic control of free electrons.

As the next step of our theoretical study, it may be interesting to further explore the role of the vacuum field in quantum mechanical properties of matter. An interesting topic would be double-slit diffraction. There have been claims in the literature

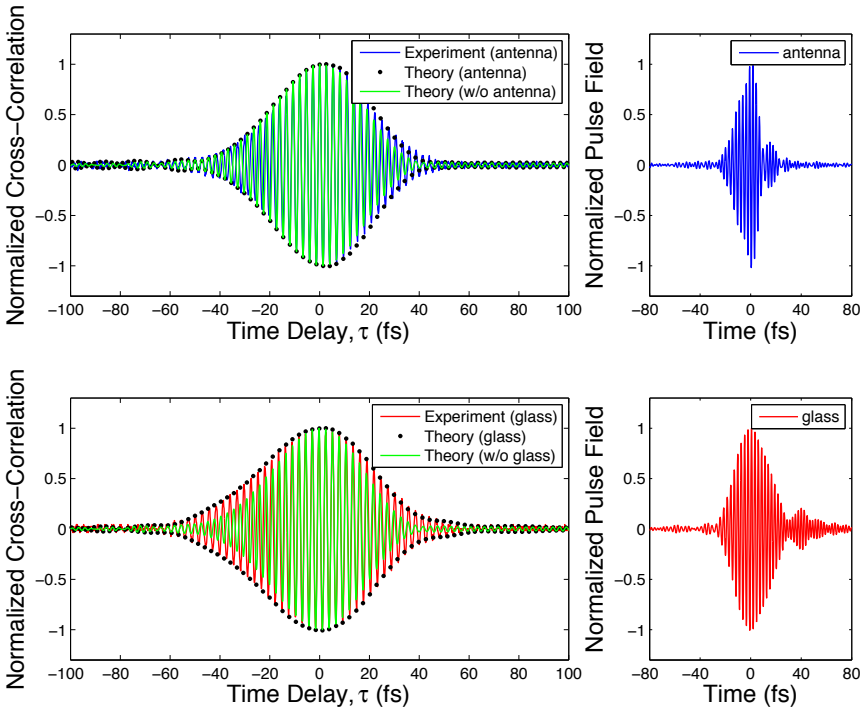


Figure 4: Field reconstruction from the cross-correlation signal.

that the wave-particle duality can be derived in a SED system [35, 36]. However, no solid evidence was provided. In view that the Heisenberg uncertainty relation and quantized excitation spectrum can both be obtained from such a classical system, it may be reasonable to consider if a similar mechanism exists to produce slit-diffraction. Such a study will touch on the heart of quantum mechanics [37], and a positive result may motivate many interesting experiments in foundational quantum mechanics.

As a natural extension of our electron deflection experiment, two laser beams may be used on a nano-structured surface with independent controls on the beams' frequencies, polarizations, phase, and incident angles. Different combinations of the above parameters can produce different spatial and temporal profiles of light on the surface. As the profile of light changes, the induced surface-charge distribution follows too. It is interesting to investigate the interaction between the free electron beam with

various near-field patterns. We anticipate that it may even be possible to use induced near-field light as a light grating and split an electron beam coherently. Moreover, it may be possible to make a traveling light-grating from the near-field and impart a discrete amount of momentum on a free electron beam.

# Bibliography

[1] C. Jönsson, *Elektroneninterferenzen an mehreren knstlich hergestellten Feinspalten*, Z. Phys. **161**, 454 (1961).

[2] B. Barwick, G. Gronniger, Y. Lu, S.-H. Liou, and H. Batelaan, *A measurement of electron-wall interactions using transmission diffraction from nanofabricated gratings*, J. Appl. Phys. **100**, 074322 (2006).

[3] J. Verbeeck, H. Tian, and P. Schattschneider, *Production and application of electron vortex beams*, Nature **467**, 301 (2010).

[4] R. Bach, D. Pope, S.-H. Liou, and H. Batelaan, *Controlled double-slit electron diffraction*, New J. Phys. **15**, 033018 (2013).

[5] H. Batelaan, *Colloquium: Illuminating the Kapitza-Dirac effect with electron matter optics*, Rev. Mod. Phys. **79**, 929 (2007).

[6] P. Genevet, J-P. Tetienne, E. Gatzogiannis, R. Blanchard, M. A. Kats, M. O. Scully, and F. Capasso, *Large enhancement of nonlinear Optical phenomena by plasmonic nanocavity gratings*, Nano Lett. **10**, 4880 (2010).

[7] P. Genevet, J-P. Tetienne, R. Blanchard, M. A. Kats, J. P. B. Müller, M. O. Scully, and F. Capasso, *Enhancement of optical processes in coupled plasmonic nanocavities* , Appl. Opt. **50**, 56 (2011).

[8] P. Genevet, J. Lin, M. A. Kats, and F. Capasso, *Holographic detection of the orbital angular momentum of light with plasmonic photodiodes*, Nat. Commun. **3**, 1278 (2012).

[9] J. Lin, J. Dellinger, P. Genevet, B. Cluzel, F. de Fornel, *Cosine-Gauss Plasmon Beam: A Localized Long-Range Nondiffracting Surface Wave*, Phys. Rev. Lett. **109**, 093904 (2012).

[10] W. E. Lamb Jr. and R. C. Retherford, *Fine Structure of the Hydrogen Atom by a Microwave Method*, *Phys. Rev.* **72**, 241 (1947).

[11] H. A. Bethe, *The Electromagnetic Shift of Energy Levels*, Phys. Rev. **72**, 339 (1947).

[12] P. Goy, J. M. Haimond, M. Gross, and S. Haroche, *Observation of Cavity-Enhanced Single-Atom Spontaneous Emission*, Phys. Rev. Lett. **50**, 1903 (1983).

[13] W. Jhe, A. Anderson, E. A. Hinds, D. Meschede, L. Moi, and S. Haroche, *Suppression of Spontaneous Decay at Optical Frequencies: Test of Vacuum Field Anisotropy in Confined Space*, Phys. Rev. Lett. **58**, 666 (1987).

[14] V. Sandoghdar, C. I. Sukenik, S. Haroche, and E. A. Hinds, *Spectroscopy of atoms confined to the single node of a standing wave in a parallel-plate cavity*, Phys. Rev. A. **53**, 1919 (1996).

[15] P. W. Milonni, *The Quantum Vacuum: An Introduction to Quantum Electrodynamics*, (Academic Press, Boston, 1994), Ch6.

[16] H. B. G. Casimir and D. Polder, *The Influence of Retardation on the London-van der Waals Forces*, Phys. Rev. **73**, 360 (1948).

[17] H. B. G. Casimir, *On the Attraction between Two Perfectly Conducting Plates*, Proc. Kon. Nederland. Akad. Wetensch. **B51**, 793 (1948).

[18] S. K. Lamoreaux, *Demonstration of the Casimir Force in the 0.6 to 6?m Range*, Phys. Rev. Lett. **78**, 5 (1997).

[19] U. Mohideen and A. Roy, *Precision Measurement of the Casimir Force from 0.1 to 0.9?m*, Phys. Rev. Lett. **81**, 4549 (1998).

[20] T. Ederth, *Template-stripped gold surfaces with 0.4-nm rms roughness suitable for force measurements: Application to the Casimir force in the 20100-nm range*, Phys. Rev. A **62**, 062104 (2000).

[21] G. Bressi, G. Carugno, R. Onofrio, and G. Ruoso, *Measurement of the Casimir Force between Parallel Metallic Surfaces*, Phys. Rev. Lett. **88**, 041804 (2002).

[22] R. S. Decca, D. López, E. Fischbach, and D. E. Krause, *Measurement of the Casimir Force between Dissimilar Metals*, Phys. Rev. Lett. **91**, 050402 (2003).

[23] F. Capasso, J. N. Munday, D. Iannuzzi, and H. B. Chan *Casimir Forces and Quantum Electrodynamical Torques: Physics and Nanomechanics*, IEEE J. Select. Top. Quant. Electron. 13, 400 (2007).

[24] J. N. Mundy, F. Capasso, and V. A. Parsegian, *Measured long-range repulsive CasimirLifshitz forces*, Nature **457**, 170 (2009).

[25] D. Lindley, *Focus: LandmarksLamb Shift Verifies New Quantum Concept*, Physics, **5**, 83 (2012)

[26] A. Salam, *From a Life of Physics*, (World Scientific, Singapore, 1989) p.27.

[27] T. W. Marshall, *Random Electrodynamics*, Proc. R. Soc. Lond. A **276**, 475 (1963).

[28] T. H. Boyer, *Random electrodynamics: The theory of classical electrodynamics with classical electromagnetic zero-point radiation*, Phys. Rev. D **11**, 790 (1975).

[29] T. H. Boyer, *General connection between random electrodynamics and quantum electrodynamics for free electromagnetic fields and for dipole oscillator systems*, Phys. Rev. D **11**, 809 (1975).

[30] T. H. Boyer, *Diamagnetism of a free particle in classical electron theory with classical electromagnetic zero-point radiation*, Phys. Rev. A **21**, 66 (1980).

[31] T. H. Boyer, *Derivation of the blackbody radiation spectrum from the equivalence principle in classical physics with classical electromagnetic zero-point radiation*, Phys. Rev. D **29**, 1096 (1984).

[32] T. H. Boyer, *Asymptotic Retarded van der Waals Forces Derived from Classical Electrodynamics with Classical Electromagnetic Zero-Point Radiation*, Phys. Rev. A, **5**, 1799 (1972).

[33] T. H. Boyer, *Unretarded London-van der Waals Forces Derived from Classical Electrodynamics with Classical Electromagnetic Zero-Point Radiation*, Phys. Rev. A, **6**, 314 (1972).

[34] T. H. Boyer, *Retarded van der Waals Forces at All Distances Derived from Classical Electrodynamics with Classical Electromagnetic Zero-Point Radiation*, Phys. Rev. A, **7**,1832 (1973).

[35] A. F. Kracklauer, *Pilot wave steerage: A mechanism and test*, Found. Phys. Lett. **12**, 441 (1999).

[36] G. Cavalleri, F. Barbero, G. Bertazzi, E. Cesaroni, E. Tonni, L. Bosi, G. Spavieri and George Gillies, *A quantitative assessment of stochastic electrodynamics with spin (SEDS): Physical principles and novel applications*, Front. Phys. China **5**, 107 (2010).

[37] R. P. Feynman, R. B. Leighton, and M. Sands, *The Feynman Lectures on Physics: Quantum Mechanics*, Vol. 3,(Addison-Wesley, Reading, MA, 1965), p.1-1.

# Chapter 1

# Dynamics of a Classical Harmonic Oscillator in Vacuum Field

Stochastic electrodynamics (SED) predicts a Gaussian probability distribution for a classical harmonic oscillator in the vacuum field. This probability distribution is identical to that of the ground state quantum harmonic oscillator. Thus, the Heisenberg minimum uncertainty relation is recovered in SED. To understand the dynamics that gives rise to the uncertainty relation and the Gaussian probability distribution, we perform a numerical simulation and follow the motion of the oscillator. The dynamical information obtained through the simulation provides insight to the connection between the double-peak probability distribution and the Gaussian probability distribution.

## 1.1 Introduction

According to quantum electrodynamics, the vacuum is not a tranquil place. A background electromagnetic field, called the electromagnetic vacuum field, is always present, independent of any external electromagnetic source [1]. The first experimental evidence of the vacuum field dates back to 1947 when Lamb and his graduate student Retherford found an unexpected shift in the hydrogen fine structure spectrum [2, 3]. The physical existence of the vacuum field has inspired an interesting modification to the classical mechanics. The modified theory is generally known as stochastic electrodynamics (SED) [4]. As a variation of classical electrodynamics, SED adds a background electromagnetic vacuum field to the classical mechanics. The vacuum field as formulated in SED has no adjustable parameters except that each field mode has a random initial phase and that the field strength is set by the Planck constant, $\hbar$. With the aid of this background field, SED is able to reproduce a number of results that were originally thought to be pure quantum effects [1, 4, 6, 7, 8, 9].

In the case of a classical harmonic oscillator, the vacuum field forcing has caused the particle's dynamics to change. Boyer showed that the moments $\langle x^n \rangle$ of a classical harmonic oscillator in vacuum field are identical to those of the ground state quantum harmonic oscillator [10]. As a consequence, its probability distribution obtains a Gaussian shape (see Figure 1.1), and the Heisenberg minimum uncertainty relation is satisfied. These interesting results were obtained analytically several decades ago. If one wishes to draw a direct connection between the probability distribution and a single particle's dynamical behavior, some subtle issues still need to be addressed. To be specific, as the probability distribution was obtained through averaging over the phase that is in the vacuum field, it can reflect only the statistical behavior of particles. To make a connection between the probability distribution and a single particle's

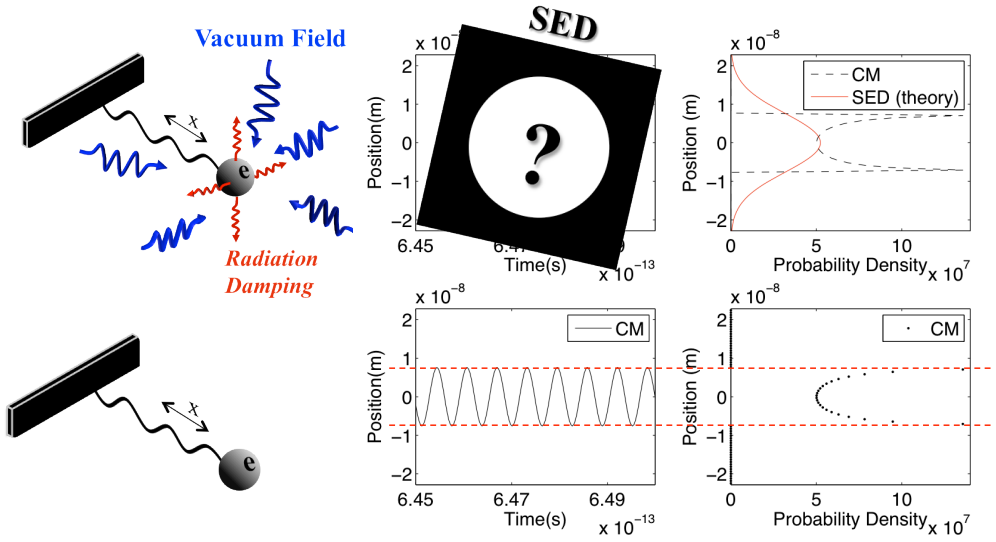


Figure 1.1: A comparison between the harmonic oscillators with and without the vacuum field. Top: Without any external force except for the vacuum field, the SED harmonic oscillator undergoes a motion that results in a Gaussian probability distribution. This motion is investigated with our simulation. Bottom: In the absence of the vacuum field or any external drive, a harmonic oscillator that is initially displaced from equilibrium performs a simple harmonic oscillation with constant oscillation amplitude. The resulting probability distribution has peaks at the two turning points.

dynamical properties in time, one often needs to invoke the concept of ergodicity. As the justification of the ergodic assumption for a SED system is challenging, we will not attempt such an analysis. Instead, we take a numerical approach to obtain the probability distribution directly from a single trajectory[1], and we investigate the relation between such a probability distribution and the particle's dynamical properties. Therefore, the questions that we want to address in this study are three: Is the probability distribution constructed from a single trajectory still a Gaussian? Does it satisfy Heisenberg's minimum uncertainty? If the answers are yes, how does

[1] It may be possible to use the central limit theorem to prove that the probability distribution from a single trajectory is Gaussian. However, here the assumption for the central limit theorem would be that the positions in time are independent random variables. This property can not be easily justified for our system, because the correlation between the motion at two points in time persists beyond many cycles of oscillation.

the driving of the vacuum field turn the classic double-peak distribution (that one finds with the vacuum field) into a Gaussian distribution?

Additionally, most work in the field of SED is analytical, and numerical studies are rare [11, 12, 13]. The advantage of numerical simulation is that it may be extended to physical systems that do not have and analytical solution. The major challenge for the numerical simulation is to account for the physics of the vacuum field that has a spectrum of infinite bandwidth. A representative sampling of the vacuum field modes is thus the key for the success of numerical simulations. In this numerical study, we use a simple physical system (i.e. harmonic oscillator), to develop a numerical method for which the results can be compared to the results of known analytical calculation. We document the details of our simulation so that it can be used by others.

## 1.2 Theory of Stochastic Electrodynamics

### 1.2.1 Brief Review of Boyer's Work

In his 1975 papers [4, 10], Boyer calculated the statistical features of an SED harmonic oscillator, and the Heisenberg minimum uncertainty relation is shown to be satisfied for such an oscillator. The vacuum field used in Boyer's work arises from the homogeneous solution of Maxwell's equations, which is assumed to be zero in classical electrodynamics [4]. In an unbounded (free) space, the vacuum field has an integral

form[2],

$$\mathbf{E}_{vac}(\mathbf{r},t) = \sum_{\lambda=1}^{2} \int d^3k \; \boldsymbol{\varepsilon}(\mathbf{k},\lambda) \frac{\eta(\mathbf{k},\lambda)}{2} \left( a(\mathbf{k},\lambda) e^{i(\mathbf{k}\cdot\mathbf{r}-\omega t)} + a^*(\mathbf{k},\lambda) e^{-i(\mathbf{k}\cdot\mathbf{r}-\omega t)} \right), \quad (1.1)$$

$$\eta(\mathbf{k},\lambda) \equiv \sqrt{\frac{\hbar\omega}{8\pi^3\epsilon_0}}, \quad (1.2)$$

$$a(\mathbf{k},\lambda) \equiv e^{i\tilde{\theta}(\mathbf{k},\lambda)}, \quad (1.3)$$

where $\omega = c|\mathbf{k}|$, and $\tilde{\theta}(\mathbf{k},\lambda)$ is the random phase uniformly distributed in $[0, 2\pi]$. The integral is to be taken over all $\mathbf{k}$-space. The two unit vectors, $\boldsymbol{\varepsilon}(\mathbf{k},1)$ and $\boldsymbol{\varepsilon}(\mathbf{k},2)$, describe a polarization basis in a plane that is perpendicular to the wave vector $\mathbf{k}$,

$$\boldsymbol{\varepsilon}(\mathbf{k},\lambda) \cdot \mathbf{k} = 0. \quad (1.4)$$

Furthermore, the polarization basis vectors are chosen to be mutually orthogonal,

$$\boldsymbol{\varepsilon}(\mathbf{k},1) \cdot \boldsymbol{\varepsilon}(\mathbf{k},2) = 0. \quad (1.5)$$

To investigate the dynamics of the SED harmonic oscillator, Boyer used the dipole approximation,

$$\mathbf{k} \cdot \mathbf{r} \ll 1, \quad (1.6)$$

to remove the spatial dependence in the vacuum field, Eq. (1.1). Therefore, the equation of motion for an SED harmonic oscillator used in Boyer's analysis is

$$m\ddot{x} = -m\omega_0^2 x + m\Gamma\dddot{x} + qE_{vac,\mathrm{x}}(t), \quad (1.7)$$

[2] A detailed account of the vacuum field in unbounded space is given in Appendix A.1.

where $\Gamma \equiv \dfrac{2q^2}{3mc^3}\dfrac{1}{4\pi\epsilon_0}$ is the radiation damping parameter, $m$ is the mass, $q$ is the charge, and $\omega_0$ is the natural frequency. The $x$-component of the vacuum field in Eq. (1.7) is

$$E_{vac,\mathrm{x}}(t) = \sum_{\lambda=1}^{2} \int d^3k \; \varepsilon_{\mathrm{x}}(\mathbf{k},\lambda) \frac{\eta(\mathbf{k},\lambda)}{2} \left( a(\mathbf{k},\lambda) e^{-i\omega t} + a^*(\mathbf{k},\lambda) e^{i\omega t} \right), \tag{1.8}$$

and the steady-state solution is obtained as

$$x(t) = \frac{q}{m} \sum_{\lambda=1}^{2} \int d^3k \; \varepsilon_{\mathrm{x}}(\mathbf{k},\lambda) \frac{\eta(\mathbf{k},\lambda)}{2} \left( \frac{a(\mathbf{k},\lambda)}{C(\mathbf{k},\lambda)} e^{-i\omega t} + \frac{a^*(\mathbf{k},\lambda)}{C^*(\mathbf{k},\lambda)} e^{i\omega t} \right), \tag{1.9}$$

where $C(\mathbf{k},\lambda) \equiv (-\omega^2 + \omega_0^2) - i\Gamma\omega^3$. Additionally, using the condition of sharp resonance,

$$\Gamma\omega_0 \ll 1, \tag{1.10}$$

Boyer further calculated the standard deviation of position and momentum from Eq. (1.9) by averaging over the random phase $\tilde{\theta}$ [10],

$$\sigma_x = \sqrt{\langle x^2 \rangle_{\tilde{\theta}} - \langle x \rangle_{\tilde{\theta}}^2} = \sqrt{\frac{\hbar}{2m\omega_0}}, \tag{1.11}$$

$$\sigma_p = \sqrt{\langle p^2 \rangle_{\tilde{\theta}} - \langle p \rangle_{\tilde{\theta}}^2} = \sqrt{\frac{\hbar m\omega_0}{2}}, \tag{1.12}$$

where the phase averaging $\langle \quad \rangle_{\tilde{\theta}}$ represents the ensemble average over many realizations. In each realization, the random phase $\tilde{\theta}$ of the vacuum field is different. The above result satisfies the Heisenberg minimum uncertainty relation,

$$\sigma_x \sigma_p = \frac{\hbar}{2}. \tag{1.13}$$

From an energy argument, Boyer showed that this uncertainty relation can also be derived from a delicate balance between the energy gain from the vacuum field and the energy loss through radiation damping [4].

### 1.2.2 Probability Distribution

Given the knowledge of the moments $\langle x^n \rangle_{\tilde{\theta}}$, the Fourier coefficients $F_{\tilde{\theta}}(k)$ of the probability distribution $P_{\tilde{\theta}}(x)$ can be determined by Taylor expanding $e^{-ikx}$ in powers of $x^n$,

$$F_{\tilde{\theta}}(k) = \int_{-\infty}^{+\infty} e^{-ikx} P_{\tilde{\theta}}(x)\, dx = \sum_{n=0}^{\infty} \frac{(-ik)^n}{n!} \int_{-\infty}^{+\infty} x^n P_{\tilde{\theta}}(x)\, dx = \sum_{n=0}^{\infty} \frac{(-ik)^n}{n!} \langle x^n \rangle_{\tilde{\theta}}. \tag{1.14}$$

Using Eq. (1.9) and the relation from Boyer's paper [10]

$$\begin{aligned} \left\langle e^{\pm i(\tilde{\theta}(\mathbf{k},\lambda)+\tilde{\theta}(\mathbf{k}',\lambda'))} \right\rangle_{\tilde{\theta}} &= 0, \\ \left\langle e^{\pm i(\tilde{\theta}(\mathbf{k},\lambda)-\tilde{\theta}(\mathbf{k}',\lambda'))} \right\rangle_{\tilde{\theta}} &= \delta_{\lambda',\lambda}\delta^3(\mathbf{k}'-\mathbf{k}), \end{aligned} \tag{1.15}$$

the moments $\langle x^n \rangle_{\tilde{\theta}}$ can be evaluated,

$$\begin{aligned} \left\langle x^{2m+1} \right\rangle_{\tilde{\theta}} &= 0, \\ \left\langle x^{2m} \right\rangle_{\tilde{\theta}} &= \frac{(2m)!}{m!2^m} \left( \frac{\hbar}{2m\omega_0} \right)^m, \end{aligned} \tag{1.16}$$

where $m$ is a natural number. Consequently, only even-power terms are contributing in Eq. (1.14), and the Fourier coefficients $F_{\tilde{\theta}}(k)$ can be determined,

$$F_{\tilde{\theta}}(k) = \sum_{m=0}^{\infty} \frac{(-ik)^{2m}}{(2m)!} \left\langle x^{2m} \right\rangle = \sum_{m=0}^{\infty} \frac{1}{m!} \left( \frac{-\hbar k^2}{4m\omega_0} \right)^m = \exp\left( -\frac{\hbar}{4m\omega_0} k^2 \right). \tag{1.17}$$

Therefore, although not explicitly given, it is implied by Boyer's work [10] that the probability distribution of the SED harmonic oscillator is

$$P_{\tilde{\theta}}(x) = \frac{1}{2\pi}\int_{-\infty}^{+\infty} e^{ikx} F_{\tilde{\theta}}(k)\, dk = \sqrt{\frac{m\omega_0}{\pi\hbar}}\exp\Big(-\frac{m\omega_0}{\hbar}x^2\Big), \tag{1.18}$$

which is identical to the probability distribution of the quantum harmonic oscillator in the ground state[3].

## 1.3 Methods of Numerical Simulation

### 1.3.1 Vacuum Field in Bounded Space

While the vacuum field in unbounded space is not subject to any boundary condition thus every wave vector $\mathbf{k}$ is allowed [4], the field confined in a space of volume $V$ with zero value boundary condition has a discrete spectrum, and a summation over infinitely many countable wave vectors $\mathbf{k}$ is required [1, 5]. In a simulation, it is convenient to write the vacuum field in the summation form,

$$\mathbf{E}_{vac} = \sum_{\mathbf{k},\lambda}\sqrt{\frac{\hbar\omega}{\epsilon_0 V}}\cos(\mathbf{k}\cdot\mathbf{r} - \omega t + \tilde{\theta}_{\mathbf{k}\lambda})\boldsymbol{\varepsilon}_{\mathbf{k}\lambda}, \tag{1.19}$$

where $a_{\mathbf{k}\lambda} \equiv e^{i\tilde{\theta}_{\mathbf{k}\lambda}}$, $\omega = c|\mathbf{k}|$, $\tilde{\theta}_{\mathbf{k}\lambda}$ is the random phase uniformly distributed in $[0, 2\pi]$, and $V$ is the volume of the bounded space. A derivation of the summation form of the vacuum field in bounded space is given in Appendix A.2.

While the spatial boundary of the vacuum field affects the distance between adjacent wave vectors in $\mathbf{k}$-space, the spectral width of the vacuum field is unlimited.

[3] This result is consistent with the phase space probability distribution given in Marshall's work [14].

In Boyer's analysis, the infinite bandwidth of the vacuum field is reduced to a finite value via the use of the sharp resonance condition. For a direct comparison between the simulation and Boyer's analysis, we also apply the sharp resonance condition and sample only the wave vectors $\mathbf{k}$ whose frequencies is in $[\omega_0 - \Delta/2, \omega_0 + \Delta/2]$. Such approximation is valid as long as the chosen frequency range $\Delta$ completely covers the characteristic resonance width $\Gamma\omega_0^2$ of the harmonic oscillator,

$$\Gamma\omega_0^2 \ll \Delta. \tag{1.20}$$

On the other hand, the distribution of the allowed wave vectors $\mathbf{k}$ depends on the specific shape of the bounded space. In a cubic space of volume $V$, the allowed wave vectors $\mathbf{k}$ are uniformly distributed at cubic grid points, and the corresponding vacuum field is

$$\mathbf{E}_{vac} = \sum_{\lambda=1}^{2} \sum_{(k_x,k_y,k_z)} \sqrt{\frac{\hbar\omega}{\epsilon_0 V}} \cos(\mathbf{k}\cdot\mathbf{r} - \omega t + \tilde{\theta}_{\mathbf{k}\lambda})\boldsymbol{\varepsilon}_{\mathbf{k}\lambda}. \tag{1.21}$$

The sampling density is uniform and has a simple relation with the space volume $V$,

$$\rho_{\mathbf{k}} = \frac{V}{(2\pi)^3}. \tag{1.22}$$

Nevertheless, such uniform cubic sampling is not convenient for describing a frequency spectrum, and it requires large number of sampled modes to reproduce the analytical result. In order to sample only the wave vectors $\mathbf{k}$ in the resonance region, spherical coordinates are used. For the sampling to be uniform, each sampled wave vector $\mathbf{k}$ must occupy the same size of finite discrete volume element $\Delta^3 k \simeq k^2 \sin\theta \Delta k \Delta\theta \Delta\phi$. To sample for modes in the resonance region with each mode occupying the same volume size, we use a set of specifically chosen numbers $(\kappa_{ijn}, \vartheta_{ijn}, \varphi_{ijn})$ to sample the

wave vectors $\mathbf{k}$. For $i = 1 \ldots N_\kappa$, $j = 1 \ldots N_\vartheta$, and $n = 1 \ldots N_\varphi$,

$$\begin{aligned} \kappa_{ijn} &= (\omega_0 - \Delta/2)^3/3c^3 + (i-1)\Delta\kappa, \\ \vartheta_{ijn} &= -1 + (j-1)\Delta\vartheta, \\ \varphi_{ijn} &= R_{ij}^{(0)} + (n-1)\Delta\varphi, \end{aligned} \tag{1.23}$$

where $R_{ij}^{(0)}$ is a random number uniformly distributed in $[0, 2\pi]$, and the stepsizes are constant,

$$\Delta\kappa = \frac{[(\omega_0 + \Delta/2)^3/3c^3 - (\omega_0 - \Delta/2)^3/3c^3]}{N_\kappa - 1}, \tag{1.24}$$

$$\Delta\vartheta = \frac{2}{N_\vartheta - 1}, \tag{1.25}$$

$$\Delta\varphi = \frac{2\pi}{N_\varphi}. \tag{1.26}$$

For fixed $i$ and $j$, the sampled modes are arranged as a ring. The random number $R_{ij}^{(0)}$ should not be confused with the random phase in the vacuum field. In principle, a uniform sampling in angle can be used, but we found the random sampling convenient. A set of numbers $(\kappa_{ijn}, \vartheta_{ijn}, \varphi_{ijn})$ is then used for assigning the spherical coordinates to each sampled wave vector $\mathbf{k}$,

$$\mathbf{k}_{ijn} = \begin{pmatrix} k_\mathrm{x} \\ k_\mathrm{y} \\ k_\mathrm{z} \end{pmatrix} = \begin{pmatrix} k_{ijn} \sin(\theta_{ijn}) \cos(\phi_{ijn}) \\ k_{ijn} \sin(\theta_{ijn}) \sin(\phi_{ijn}) \\ k_{ijn} \cos(\theta_{ijn}) \end{pmatrix}, \tag{1.27}$$

where

$$\begin{aligned} k_{ijn} &= (3\kappa_{ijn})^{1/3}, \\ \theta_{ijn} &= \cos^{-1}(\vartheta_{ijn}), \\ \phi_{ijn} &= \varphi_{ijn}. \end{aligned} \tag{1.28}$$

Therefore, each sampled wave vector $\mathbf{k}_{ijn}$ is in the resonance region and occupies approximately the same size of finite discrete volume element,

$$\Delta^3 k \simeq k^2 \sin\theta \Delta k \Delta\theta \Delta\phi \simeq \Delta\kappa \Delta\vartheta \Delta\varphi. \tag{1.29}$$

The differential limit is approached when $N_\kappa$, $N_\vartheta$, and $N_\varphi$ are large. The numerical result is expected to converge to the analytical solution in this limit. The use of discrete sampling in this work is intended to approximate the analytical integral by a numerical summation. Subsequently, the uncountable number of modes between any sampled wave vectors are not taken into account. By increasing the sampling numbers, what we hope to see is that the numerical simulation approaches to the analytical results. If that turns out to be the case, it would indicate the uncountable modes in between the sample wave vectors are not critical for the physics studied here.

Under the uniform spherical sampling method (described by Eqs. (1.23), (1.27), and (1.28)), the expression for the vacuum field, Eq. (1.19), becomes

$$\mathbf{E}_{vac} = \sum_{\lambda=1}^{2} \sum_{(\kappa,\vartheta,\varphi)} \sqrt{\frac{\hbar\omega}{\epsilon_0 V}} \cos(\mathbf{k}\cdot\mathbf{r} - \omega t + \tilde{\theta}_{\mathbf{k}\lambda}) \boldsymbol{\varepsilon}_{\mathbf{k}\lambda}. \tag{1.30}$$

where $\mathbf{k} = \mathbf{k}_{ijn}$. It is worth noting that when the total number of wave vectors $N_{\mathbf{k}}$ becomes very large, both uniform spherical and cubic sampling approach to each

other because they both sample a large number of wave vectors in the same area of $\mathbf{k}$-space. In the limit of large sampling number $N_{\mathbf{k}} \to \infty$, the two sampling methods are equivalent[4], and Eq. (1.22) can be used for both sampling methods to calculate the volume factor $V$ in Eqs. (1.21) and (1.30),

$$V = (2\pi)^3 \rho_{\mathbf{k}} = (2\pi)^3 \frac{N_{\mathbf{k}}}{V_{\mathbf{k}}}, \tag{1.31}$$

where

$$V_{\mathbf{k}} = \frac{4\pi}{3}\left(\frac{\omega_0 + \Delta/2}{c}\right)^3 - \frac{4\pi}{3}\left(\frac{\omega_0 - \Delta/2}{c}\right)^3. \tag{1.32}$$

In the simulation, the summation indices in Eq. (1.30) can be rewritten as

$$\mathbf{E}_{vac} = \sum_{\lambda=1}^{2}\sum_{i=1}^{N_\kappa}\sum_{j=1}^{N_\vartheta}\sum_{n=1}^{N_\varphi}\sqrt{\frac{\hbar\omega}{\epsilon_0 V}}\cos(\mathbf{k}\cdot\mathbf{r} - \omega t + \tilde{\theta}_{\mathbf{k}\lambda})\boldsymbol{\varepsilon}_{\mathbf{k}\lambda}, \tag{1.33}$$

where the multiple sums indicate a numerical nested loop, and the wave vector $\mathbf{k} = \mathbf{k}_{ijn}$ is chosen according to the uniform spherical sampling method. To reproduce the analytical result, $N_\vartheta$ and $N_\varphi$ need to be sufficiently large so that the wave vector $\mathbf{k}$ at a fixed frequency may be sampled isotropically. In addition, a large $N_\kappa$ is required for representative samplings in frequency. As a result, $N_{\mathbf{k}} = N_\kappa N_\vartheta N_\varphi$ needs to be very large when using uniform spherical sampling for numerical simulation. To improve the efficiency of the computer simulation, we sample $\mathbf{k}$ at one random angle $(\theta_i, \phi_i)$

[4] Keeping $V_{\mathbf{k}}$ as a fixed value, the relation $\rho_{\mathbf{k}} = 1/\Delta^3 k = N_{\mathbf{k}}/V_{\mathbf{k}} = V/(2\pi)^3$ implies that the limit of large sampling number (i.e. $N_{\mathbf{k}} \to \infty$) is equivalent to the limit of unbounded space (i.e. $V \to \infty$). At this limit, the volume element becomes differential (denoted as $d^3k$) and is free from any specific shape associated with the space boundary. Therefore, all sampling methods for the allowed wave vectors $\mathbf{k}$ become equivalent, and the summation approaches the integral. This is consistent with the fact that no volume factor $V$ is involved in the vacuum field integral, as shown in Eq. (1.1).

for each frequency. Namely, for $i = 1 \ldots N_\omega$,

$$\mathbf{k}_i = \begin{pmatrix} k_\mathrm{x} \\ k_\mathrm{y} \\ k_\mathrm{z} \end{pmatrix} = \begin{pmatrix} k_i \sin\theta_i \cos\phi_i \\ k_i \sin\theta_i \sin\phi_i \\ k_i \cos\theta_i \end{pmatrix}, \tag{1.34}$$

where

$$\begin{aligned} k_i &= (3\kappa_i)^{1/3}, \\ \theta_i &= \cos^{-1}(\vartheta_i), \\ \phi_i &= \varphi_i, \end{aligned} \tag{1.35}$$

and

$$\begin{aligned} \kappa_i &= (\omega_0 - \Delta/2)^3/3c^3 + (i-1)\Delta\kappa, \\ \vartheta_i &= R_i^{(1)}, \\ \varphi_i &= R_i^{(2)}. \end{aligned} \tag{1.36}$$

The stepsize $\Delta\kappa$ is specified in Eq. (1.24), $\vartheta = R_i^{(1)}$ is a random number uniformly distributed in $[-1, 1]$, and $\varphi = R_i^{(2)}$ is another random number uniformly distributed in $[0, 2\pi]$. As the number of sampled frequencies $N_\omega$ becomes sufficiently large, the random angles $(\theta_i, \phi_i)$ will approach the angles specified in uniform spherical sampling (Eq. (1.23)). In the limit of $\Delta/\omega_0 \ll 1$, the above sampling method (described by Eqs. (1.34), (1.35), and (1.36)) and the uniform spherical sampling method both approach a uniform sampling on a spherical surface at the radius $r_k = \dfrac{\omega_0}{c}$. In this limit, the addition of the condition in Eq. (1.20) leads to the possible choices for the frequency range $\Delta$,

$$\Gamma\omega_0 \ll \Delta/\omega_0 \ll 1. \tag{1.37}$$

Within this range (Eq. (1.37)), the expression for the vacuum field in Eq. (1.19) becomes

$$\mathbf{E}_{vac} = \sum_{\lambda=1}^{2} \sum_{i=1}^{N_\omega} \sqrt{\frac{\hbar\omega}{\epsilon_0 V}} \cos(\mathbf{k}\cdot\mathbf{r} - \omega t + \tilde{\theta}_{\mathbf{k}\lambda}) \boldsymbol{\varepsilon}_{\mathbf{k}\lambda}. \tag{1.38}$$

where $\mathbf{k} = \mathbf{k}_i$. For large $N_\mathbf{k} = N_\omega$, the volume factor $V$ is calculated using Eq. (1.31).

Finally, for a complete specification of the vacuum field, Eq. (1.38), the polarizations $\boldsymbol{\varepsilon}_{\mathbf{k}\lambda}$ need to be chosen. From Eq. (1.31), we notice that large $N_\mathbf{k}$ gives large $V$. Since for large $V$ the vacuum field is not affected by the space boundary, there should be no preferential polarization direction, and the polarizations should be isotropically distributed. The construction for isotropically distributed polarizations is discussed in detail in Appendix B. Here we give the result that satisfies the property of isotropy and the properties of polarization (described by Eqs. (1.4) and (1.5)),

$$\begin{aligned}
\boldsymbol{\varepsilon}_{\mathbf{k},1} &= \begin{pmatrix} \varepsilon_{1,\mathrm{x}} \\ \varepsilon_{1,\mathrm{y}} \\ \varepsilon_{1,\mathrm{z}} \end{pmatrix} = \begin{pmatrix} \cos\theta_i \cos\phi_i \cos\chi_i - \sin\phi_i \sin\chi_i \\ \cos\theta_i \sin\phi_i \cos\chi_i + \cos\phi_i \sin\chi_i \\ -\sin\theta_i \cos\chi_i \end{pmatrix}, \\
\boldsymbol{\varepsilon}_{\mathbf{k},2} &= \begin{pmatrix} \varepsilon_{2,\mathrm{x}} \\ \varepsilon_{2,\mathrm{y}} \\ \varepsilon_{2,\mathrm{z}} \end{pmatrix} = \begin{pmatrix} -\cos\theta_i \cos\phi_i \sin\chi_i - \sin\phi_i \cos\chi_i \\ -\cos\theta_i \sin\phi_i \sin\chi_i + \cos\phi_i \cos\chi_i \\ \sin\theta_i \sin\chi_i \end{pmatrix},
\end{aligned} \tag{1.39}$$

where $\chi$ is a random number uniformly distributed in $[0, 2\pi]$. With the wave vectors $\mathbf{k}$ (described by Eqs. (1.34), (1.35), and (1.36)) and the polarizations $\boldsymbol{\varepsilon}_{\mathbf{k}\lambda}$ (described by Eq. (1.39)), the endpoints of the sampled vacuum field vector are plotted on a unit sphere as shown in Figure 1.2, which illustrates the isotropy of the distribution.

In summary, the vacuum field mode $(\mathbf{k}, \lambda)$ in Eq. (1.38) can be sampled by a set of four numbers $(\kappa_i, \vartheta_i, \varphi_i, \chi_i)$, which are specified in Eqs. (1.34), (1.35), (1.36), and Eq. (1.39). The only assumption used in determining these numbers is Eq. (1.37),

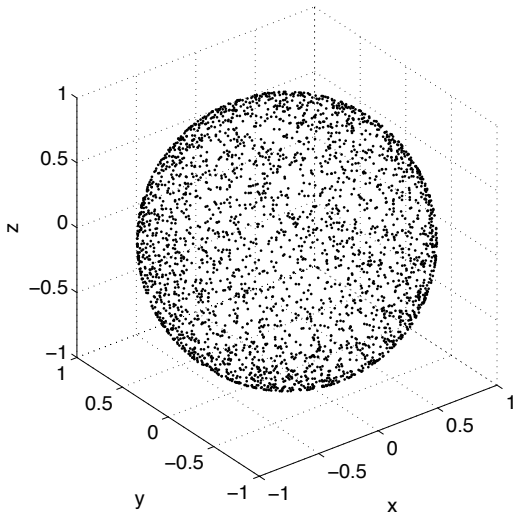


Figure 1.2: The isotropic distribution of the polarization field vectors $\boldsymbol{\varepsilon}_{\mathbf{k},1}$ (number of sampled frequencies number $N_\omega = 3 \times 10^3$). The endpoints of the polarization field vectors, $\boldsymbol{\varepsilon}_{\mathbf{k},1}$, are plotted for a random sampling of modes $(\mathbf{k}, 1)$ according to the methods described in Eqs. (1.34), (1.35), and (1.36).

which is equivalent to the sharp resonance condition (Eq. (1.10)) used in Boyer's analysis.

### 1.3.2 Equation of Motion in Numerical Simulation

In the unbounded (free) space, the equation of motion in Boyer's analysis is,

$$m\ddot{x} = -m\omega_0^2 x + m\Gamma\dddot{x} + qE_{vac,\mathrm{x}}(t), \tag{1.40}$$

where the dipole approximation $\mathbf{k} \cdot \mathbf{r} \ll 1$ (Eq. (1.6)) is used. In the bounded space, the equation of motion remains the same, but the vacuum field is formulated has the summation form (Eq. (1.38)),

$$\mathbf{E}_{vac} = \sum_{\mathbf{k},\lambda} \sqrt{\frac{\hbar\omega}{\epsilon_0 V}} \frac{1}{2} \left( a_{\mathbf{k}\lambda} e^{-i\omega t} + a^*_{\mathbf{k}\lambda} e^{i\omega t} \right) \boldsymbol{\varepsilon}_{\mathbf{k}\lambda}, \tag{1.41}$$

where $a_{\mathbf{k}\lambda} \equiv e^{i\tilde{\theta}_{\mathbf{k}\lambda}}$. The steady-state solution to Eq. (1.40) in the bounded space can be found following Boyer's approach,

$$x(t) = \frac{q}{m} \sum_{\mathbf{k},\lambda} \sqrt{\frac{\hbar\omega}{\epsilon_0 V}} \frac{1}{2} \left( \frac{a_{\mathbf{k}\lambda}}{C_{\mathbf{k}\lambda}} e^{-i\omega t} + \frac{a^*_{\mathbf{k}\lambda}}{C^*_{\mathbf{k}\lambda}} e^{i\omega t} \right) \varepsilon_{\mathbf{k}\lambda,x}, \tag{1.42}$$

where $C_{\mathbf{k}\lambda} \equiv (-\omega^2 + \omega_0^2) - i\Gamma\omega^3$. While this analytical solution can be evaluated using our method of vacuum mode selection (Eqs. (1.34), (1.35), (1.36), and Eq. (1.39)), our goal with the numerical simulation is to reproduce Boyer's analytical results (Eq. (1.9)) so that the methods can be applied to other physical systems in future studies. One major obstacle for the numerical approach is the third-order derivative in the the radiation damping term, $m\Gamma\dddot{x}$. To circumvent this problem, we follow the perturbtive approach in [15, 16, 17]. According to classical electrodynamics, the equation of motion for an electron with radiation damping is

$$m\ddot{x} = F + m\Gamma\dddot{x}, \tag{1.43}$$

where $F$ is the force and $\Gamma \equiv \dfrac{2e^2}{3mc^3} \dfrac{1}{4\pi\epsilon_0}$ is the radiation damping coefficient. Under the assumption $m\Gamma\dddot{x} \ll F$, the zero-order equation of motion is

$$m\ddot{x} \simeq F. \tag{1.44}$$

The justification for the assumption $m\Gamma\dddot{x} \ll F$ is that a point particle description of the electron is used in classical electrodynamics [15, 17]. Using Eq. (1.44), the radiation damping term may be estimated by

$$m\Gamma\dddot{x} \simeq \Gamma\dot{F}, \tag{1.45}$$

which can be iterated back to the original equation (Eq. (1.43)) and get a perturbative expansion,

$$m\ddot{x} \simeq F + \Gamma\dot{F}. \tag{1.46}$$

Thus, in this approximated equation of motion we replace the third derivative of position $x$ by the first derivative of the force $F$. Applying Eq. (1.46) to Eq. (1.40), the equation of motion becomes

$$m\ddot{x} \simeq -m\omega_0^2 x - m\Gamma\omega_0^2\dot{x} + qE_{vac,\mathrm{x}}(t) + q\Gamma\dot{E}_{vac,\mathrm{x}}(t). \tag{1.47}$$

The order of magnitude for each term on the right-hand side is,

$$O(m\omega_0^2 x) = m\omega_0^2 x_0, \tag{1.48}$$

$$O(qE_{vac,\mathrm{x}}) = eE_0, \tag{1.49}$$

$$O(m\Gamma\omega_0^2\dot{x}) = (\Gamma\omega_0)m\omega_0^2 x_0, \tag{1.50}$$

$$O(q\Gamma\dot{E}_{vac,\mathrm{x}}) = (\Gamma\omega_0)qE_0. \tag{1.51}$$

where $x_0$ and $E_0$ are the order of magnitude for the particle motion $x$ and the vacuum field $E_{vac,\mathrm{x}}$. The order of magnitude for the time scale of particle motion is given by $1/\omega_0$ because of the sharp resonance condition Eq. (1.10). In order to compare the two radiation damping terms (Eqs. (1.50) and (1.51)), we use a random walk model to estimate $x_0$ and $E_0$. For a fixed time $t = t_0$, the order of magnitude for $E_{vac,\mathrm{x}}(t_0)$ and $x(t_0)$ (see Eqs. (1.41) and (1.42)) is equal to $E_0$ and $x_0$. Written as complex numbers, the mathematical form of $\tilde{E}_{vac,\mathrm{x}}(t_0)$ and $\tilde{x}(t_0)$ is analogous to a two-dimensional random walk on the complex plane with random variable $\Theta_{\{\mathbf{k},\lambda\}}$, where $\{\mathbf{k},\lambda\}$ denotes a set of modes $(\mathbf{k},\lambda)$. Averaging over $\{\mathbf{k},\lambda\}$, the order of magnitude for $E_{vac,\mathrm{x}}(t_0)$ and $x(t_0)$ can be estimated by the root-mean-squared distance of $\tilde{E}_{vac,\mathrm{x}}(t_0)$

and $\tilde{x}(t_0)$. In a two-dimensional random walk model [18], the root-mean-squared distance $D_{rms}$ is given by

$$D_{rms} = \sqrt{N_s} \cdot \Delta s, \tag{1.52}$$

where $N_s$ is the number of steps taken, and $\Delta s$ is a typical stepsize; for $D^{(E)}_{rms}$, $\Delta s = \frac{1}{2}\sqrt{\frac{\hbar\omega_0}{\epsilon_0 V}}$, and for $D^{(x)}_{rms}$, $\Delta s = \frac{1}{2}\left(\frac{q}{m\Gamma\omega_0^3}\sqrt{\frac{\hbar\omega_0}{\epsilon_0 V}}\right)$. Hence, the order of magnitude, $E_0$ and $x_0$, may be estimated as[5]

$$\begin{aligned} E_0 &\simeq D^{(E)}_{rms} = \sqrt{2N_\omega} \cdot \frac{1}{2}\sqrt{\frac{\hbar\omega_0}{\epsilon_0 V}}, \\ x_0 &\simeq D^{(x)}_{rms} = \sqrt{2N_\omega} \cdot \frac{1}{2}\left(\frac{q}{m\Gamma\omega_0^3}\sqrt{\frac{\hbar\omega_0}{\epsilon_0 V}}\right). \end{aligned} \tag{1.53}$$

The order of magnitude for the two radiation damping term is evaluated accordingly,

$$\begin{aligned} O(m\Gamma\omega_0^2\dot{x}) &\simeq q\sqrt{\frac{N_\omega}{2}} \cdot \sqrt{\frac{\hbar\omega_0}{\epsilon_0 V}} \\ O(q\Gamma\dot{E}_{vac,\mathrm{x}}) &\simeq (\Gamma\omega_0) q\sqrt{\frac{N_\omega}{2}} \cdot \sqrt{\frac{\hbar\omega_0}{\epsilon_0 V}}. \end{aligned} \tag{1.54}$$

Using the sharp resonance condition $\Gamma\omega_0 \ll 1$ (Eq. (1.10)), we approximate the equation of motion (Eq. (1.47)) to its leading order,

$$m\ddot{x} \simeq -m\omega_0^2 x - m\Gamma\omega_0^2\dot{x} + qE_{vac,\mathrm{x}}(t). \tag{1.55}$$

As an additional note, given the estimation of $E_0$ and $x_0$ in Eq. (1.53), the three force terms in Eq. (1.55) have the following relation,

$$O(m\omega_0^2 x) \gg O(m\Gamma\omega_0^2\dot{x}) \simeq O(qE_{vac,\mathrm{x}}). \tag{1.56}$$

[5] Using $V = (2\pi)^3 N_\omega / V_{\mathbf{k}}$ and $V_{\mathbf{k}} \simeq 4\pi\omega_0^2 \left(\Gamma\omega_0^2\right)/c^3$ (Eqs. (1.31) and (1.32)), the value of $x_0$ in Eq. (1.53) can be estimated as $x_0 \simeq \sqrt{3/\pi}\sqrt{\hbar/2m\omega_0}$, which is consistent with Boyer's calculation for the standard deviation of position in Eq. (1.11).

Thus, the linear restoring force $m\omega_0^2 x$ is the dominating drive for a SED harmonic oscillator, while the vacuum field $qE_{vac,\mathrm{x}}$ and radiation damping $m\Gamma\omega_0^2\dot{x}$ act as perturbations. The balance between the vacuum field and the radiation damping constrains the oscillation amplitude to fluctuate in the vicinity of $x_0$.

Finally, as we have established an approximated equation of motion (Eq. (1.55)) for numerical simulation, the total integration time $\tau_{int}$ (i.e. how long the simulation is set to run) needs to be specified. Upon inspection, two important time scales are identified from the analytical solution of Eq. (1.55),

$$x(t) = e^{-\Gamma\omega_0^2 t/2}(Ae^{i\omega_R t} + A^* e^{-i\omega_R t}) + \frac{q}{m}\sum_{\mathbf{k},\lambda}\sqrt{\frac{\hbar\omega}{\epsilon_0 V}}\frac{1}{2}\left(\frac{a_{\mathbf{k}\lambda}}{B_{\mathbf{k}\lambda}}e^{-i\omega t} + \frac{a^*_{\mathbf{k}\lambda}}{B^*_{\mathbf{k}\lambda}}e^{i\omega t}\right)\varepsilon_{\mathbf{k}\lambda,\mathrm{x}}, \tag{1.57}$$

where $A$ is a coefficient determined by the initial conditions, and

$$\omega_R \equiv \omega_0\sqrt{1-(\Gamma\omega_0/2)^2}, \tag{1.58}$$

$$B_{\mathbf{k}\lambda} \equiv \left(-\omega^2+\omega_0^2\right) - i\left(\Gamma\omega_0^2\right)\omega, \tag{1.59}$$

$$a_{\mathbf{k}\lambda} \equiv e^{i\tilde{\theta}_{\mathbf{k}\lambda}}. \tag{1.60}$$

The first term in Eq. (1.57) represents the transient motion and the second term represents the steady-state motion. The characteristic time for the transient motion is

$$\tau_{tran} = \frac{2}{\Gamma\omega_0^2}. \tag{1.61}$$

Thus, the simulation should run beyond $\tau_{tran}$ if one is interested in the steady-state motion. As the steady-state solution is a finite discrete sum of periodic functions, it would have a non-physical repetition time $\tau_{rep}$. The choice of $\tau_{int}$ should satisfy $\tau_{int} \leq \tau_{rep}$ to avoid repetitive solutions. A detailed discussion about $\tau_{rep}$ can be found

in Appendix C. Here we give a choice of $\tau_{int}$,

$$\tau_{int} = \frac{2\pi}{\Delta\omega}, \tag{1.62}$$

where $\Delta\omega$ is the frequency gap and it can be estimated using Eqs. (1.24), (1.35), and (1.36),

$$\Delta\omega \simeq \frac{c(3\kappa_0)^{1/3}}{3}\frac{\Delta\kappa}{\kappa_0}, \tag{1.63}$$

where $\kappa_0 \equiv \frac{1}{3}\left(\frac{\omega_0}{c}\right)^3$.

To summarize, Eq. (1.55) is the approximated equation of motion to be used in numerical simulation. The vacuum field $E_{vac,\mathrm{x}}$ in Eq. (1.55) is given by Eq. (1.41). The specifications of the vacuum field modes $(\mathbf{k}, \lambda)$, polarizations $\boldsymbol{\varepsilon}_{\mathbf{k}\lambda}$, and other relevant variables can be found in Sec. 1.3.1. To approximate Eq. (1.40) by Eq. (1.55), two conditions need to be used, namely the dipole approximation Eq. (1.6) and the sharp resonance condition Eq. (1.10). The parameters $q$, $m$, and $\omega_0$ simulation should be chosen to satisfy these two conditions, as these two conditions are also used in Boyer's analysis. Lastly, the integration time $\tau_{int}$ for the simulation is chosen to be within the range $\tau_{trans} \ll \tau_{int} \leq \tau_{rep}$, where $\tau_{tran}$ and $\tau_{rep}$ are given in Eqs. (1.61) and (1.62) respectively.

## 1.4 Simulation Results

In Sec. 1.2, it was shown that the probability distribution for a SED harmonic oscillator is a Gaussian. In Sec. 1.3, we develop the methods for a numerical simulation to investigate the dynamics of the SED harmonic oscillator and how it gives rise to the Gaussian probability distribution. In this section, the results of the simulation are presented, and the relation between the trajectory and the probability distribution is

discussed.

To construct the probability distribution from particle's trajectory, two sampling methods are used. The first method is sequential sampling and the second method is ensemble sampling. In sequential sampling the position or velocity is recorded in a time sequence from a single particle's trajectory, while in ensemble sampling the same is recored only at the end of the simulation from an ensemble of particle trajectories. The recorded positions or velocities are collected in histogram and then converted to a probability distribution for comparison to the analytical result (Eq. (1.18)). Whereas the sequential sampling illustrates the relationship between the buildup of probability distribution and the dynamics of particle trajectory, the ensemble sampling is convenient for statistical interpretation. In addition, the ensemble sampling is suitable for parallel computing, which can be used to improve the computation efficiency.

### 1.4.1 Particle Trajectory and the Probability Distribution

By solving Eq. (1.55) numerically, the steady-state trajectory for the SED harmonic oscillator is obtained and shown in Figure 1.3. For a comparison, the temporal evolution of the vacuum field (Eq. (1.41)) is also included. The ordinary differential equation (Eq. (1.55)) is solved using the adaptive 5th order Cash-Karp Runge-Kutta method [19], and the integration stepsize is set as small as one twentieth of the natural period, $\frac{1}{20}\left(\frac{2\pi}{\omega_0}\right)$ to avoid numerical aliasing. The charge $q$, mass $m$, natural

frequency $\omega_0$, and vacuum field frequency range $\Delta$ are chosen to be

$$\begin{aligned} q &= e, \\ m &= 10^{-4} m_e, \\ \omega_0 &= 10^{16} \text{rad/s}, \\ \Delta &= 220 \times \Gamma \omega_0^2, \end{aligned} \tag{1.64}$$

where $e$ is the electron charge, $m_e$ is the electron mass, and $\Gamma\omega_0^2$ is the the resonance width of the haromanic oscillator. The choice of $m = 10^{-4} m_e$ is made to bring the modulation time and the natural period of the harmonic oscillator closer to each other. In other words, the equation of motion (Eq. (1.55)) covers time scales at two extremes, and the choice of mass $m = 10^{-4} m_e$ brings these two scales closer so that the integration time is manageable without losing the physical characteristics of the problem.

Here we would like to highlight some interesting features of the simulated trajectory (Figure 1.3). First, there appears to be no fixed phase or amplitude relation between the particle trajectory and the instantaneous driving field. Second, the rate of amplitude modulation in the particle trajectory is slower than that in the driving field. To gain insights into these dynamical behaviors, we study the steady-state solution of Eq. (1.57) in the Green function form [20],

$$x(t) = \frac{q}{m\omega_R} \int_{-\infty}^{t} E_{vac,\mathrm{x}}(t') e^{-\Gamma\omega_0^2 (t-t')/2} \sin\left(\omega_R (t-t')\right) dt'. \tag{1.65}$$

where $\omega_R \equiv \omega_0 \sqrt{1 - (\Gamma\omega_0/2)^2}$. The solution indicates that the effect of the driving field $E_{vac,\mathrm{x}}(t')$ at any given time $t'$ lasts for a time period of $1/\Gamma\omega_0^2$ beyond $t'$. In other words, the particle motion $x(t)$ at time $t$ is affected by the vacuum field $E_{vac,\mathrm{x}}(t')$

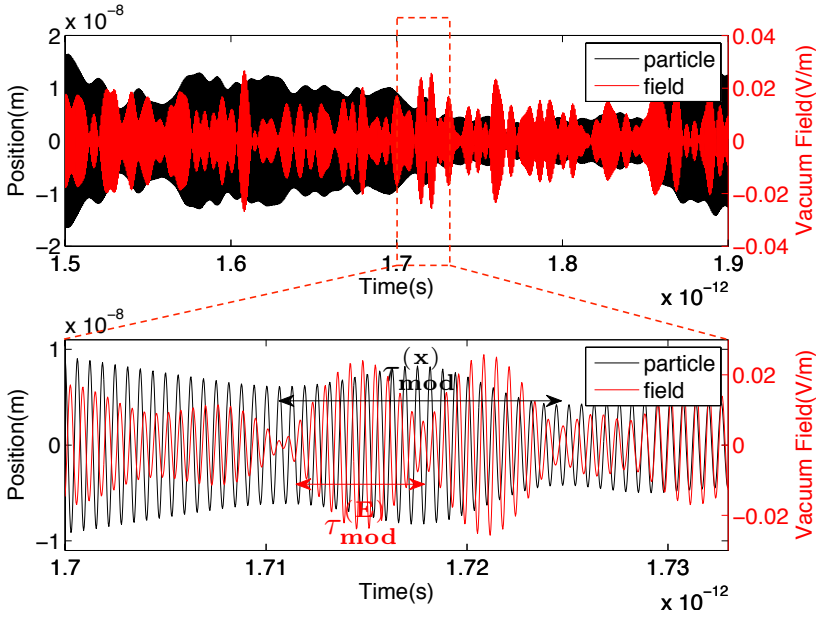


Figure 1.3: A comparison between particle trajectory and the temporal evolution of the vacuum field. Top: The vacuum field (red) is compared to the trajectory of the SED harmonic oscillator (black). Bottom: A magnified section of the trajectory shows that there is no fixed phase or amplitude relation between the particle trajectory and the instantaneous driving field. The modulation time for the field is also shown to be longer than that for the motion of the harmonic oscillator.

from all the previous moments ($t' \leq t$). As the vacuum field fluctuates in time, the fields at two points in time only becomes uncorrelated when the time separation is much longer than one coherence time[6]. This property of the vacuum field reflects on the particle trajectory, and it explains why the particle trajectory has no fixed phase or amplitude relation with the instantaneous driving field. Another implication of Eq. (1.65) is that it takes a characteristic time $1/\Gamma\omega_0^2$ for the particle to dissipate the energy gained from the instantaneous driving field. Thus, even if the field already changes its amplitude, it would still take a while for the particle to follow. This explains why the amplitude modulation in the particle trajectory is slower compared

[6] The coherence time of the vacuum field is calculated in Eq. (1.4.1).

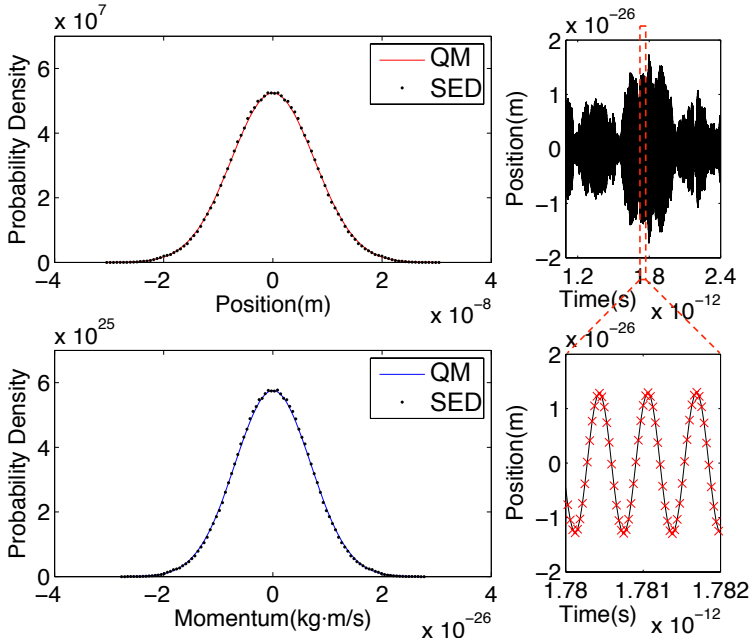


Figure 1.4: The probability distribution constructed from a single particle's trajectory (number of sampled frequencies $N_\omega = 2 \times 10^4$). Left: The position and momentum probability distributions for the SED harmonic oscillator (black dot) and the ground state quantum harmonic oscillator (red and blue line) are compared. Right: An illustration of the sequential sampling shows how positions are recorded at a regular time sequence (red cross). Note that at small time scale the oscillation amplitude is constant, but at large time scale it modulates.

to that in the driving field[7].

The sequential sampling of a simulated trajectory gives the probability distributions in Figure 1.4. While Boyer's result is obtained through ensemble (phase) averaging, the Gaussian probability distribution shown here is constructed from a single trajectory and is identical to the probability distribution of a ground state quantum harmonic oscillator.

To understand how the trajectory gives rise to a Gaussian probability distribution, we investigate the particle dynamics at two time scales. At short time scale, the par-

[7] However, in case of slow field modulation when the field bandwidth shorter than resonance width of the harmonic oscillator, the modulation time of the field and the particle trajectory are the same.

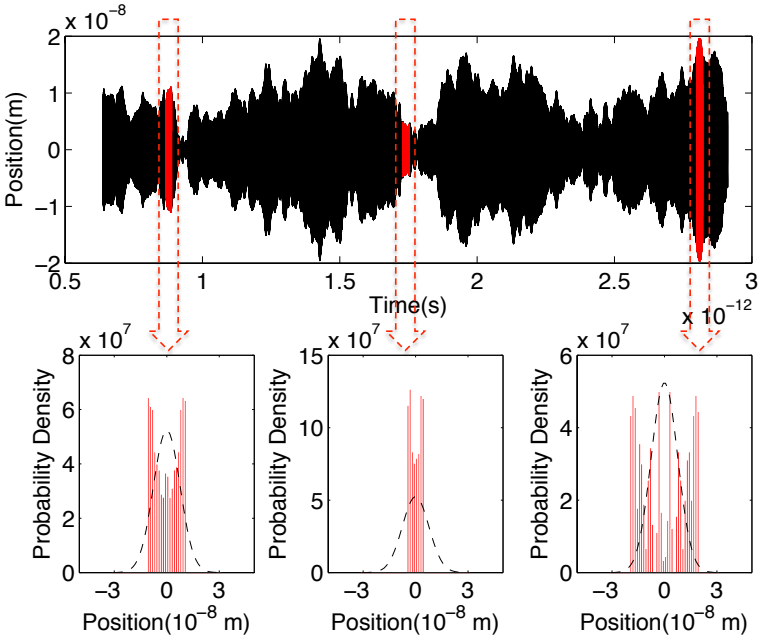


Figure 1.5: Contributions of different oscillation amplitudes in the final probability distribution. Top: Several sections (red) of a steady-state trajectory (black) are shown. A section is limited to the duration of the characteristic modulation time. The oscillation amplitude changes significantly beyond the characteristic modulation time, so different sections of the trajectory obtain different oscillation amplitudes. Bottom: The probability distributions of each section of the trajectory are shown. As the oscillation amplitude is approximately constant in each section, the corresponding probability distribution (red bar) is close to the classic double-peak distribution. The probability distributions in different sections of the trajectory contribute to different areas of the final probability distribution (black dash line). The final probability distribution is constructed from the steady-state trajectory.

ticle oscillates in a harmonic motion. The oscillation amplitude is constant, and the period is $T = 2\pi/\omega_0$. Such an oscillation makes a classical double-peak probability distribution. At large time scale, the oscillation amplitude modulates. As a result, different parts of the trajectory have double-peak probability distributions associated with different oscillation amplitudes, which add to make the final probability distribution a Gaussian distribution as shown in Figure 1.5. To verify this idea, we attempt to reconstruct the Gaussian probability distribution from the double-peak probabil-

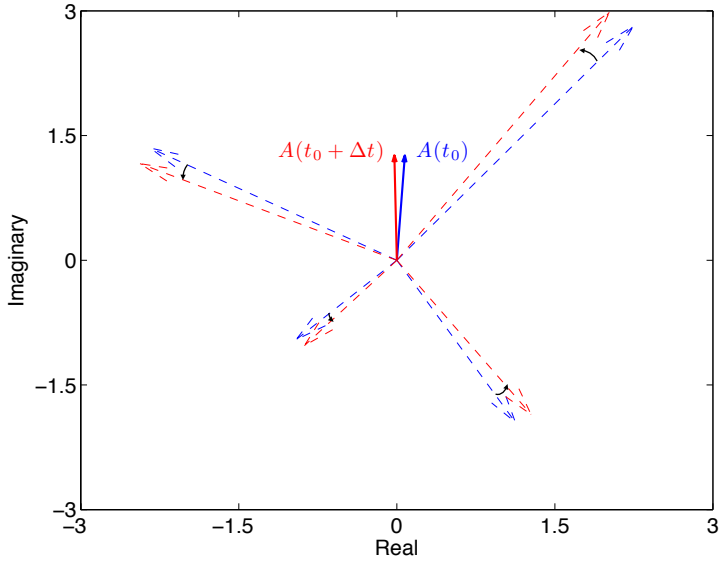


Figure 1.6: A schematic illustration of the oscillation amplitude as a sum of different frequency components in the complex plane. At a particular time $t = t_0$, an oscillation amplitude $A(t_0)$ (blue solid arrow) is formed by a group of frequency components (blue dash arrow), which rotate in the complex plane at different rate. After a time $\Delta t \ll \tau_{coh}$, the angles of the frequency components (red dash arrow) change only a little. Therefore, the oscillation amplitude $A(t_0 + \Delta t)$ (red solid arrow) does not change much within the coherence time.

ity distributions at different sections of the trajectory. We approach this problem by numerically sampling the oscillation amplitudes at a fixed time-step. To determine the appropriate sampling time-step for the oscillation amplitude, we inspect the steady-state solution (Eq. (1.57)) in its complex form,

$$\tilde{x}(t) = \frac{q}{m} \sum_{\mathbf{k},\lambda} \sqrt{\frac{\hbar\omega}{\epsilon_0 V}} \frac{a_{\mathbf{k}\lambda}}{B_{\mathbf{k}\lambda}} e^{-i\omega t} \varepsilon_{\mathbf{k}\lambda,\mathrm{x}}. \tag{1.66}$$

Since the frequency components can be sampled symmetrically around $\omega_0$, we factorize

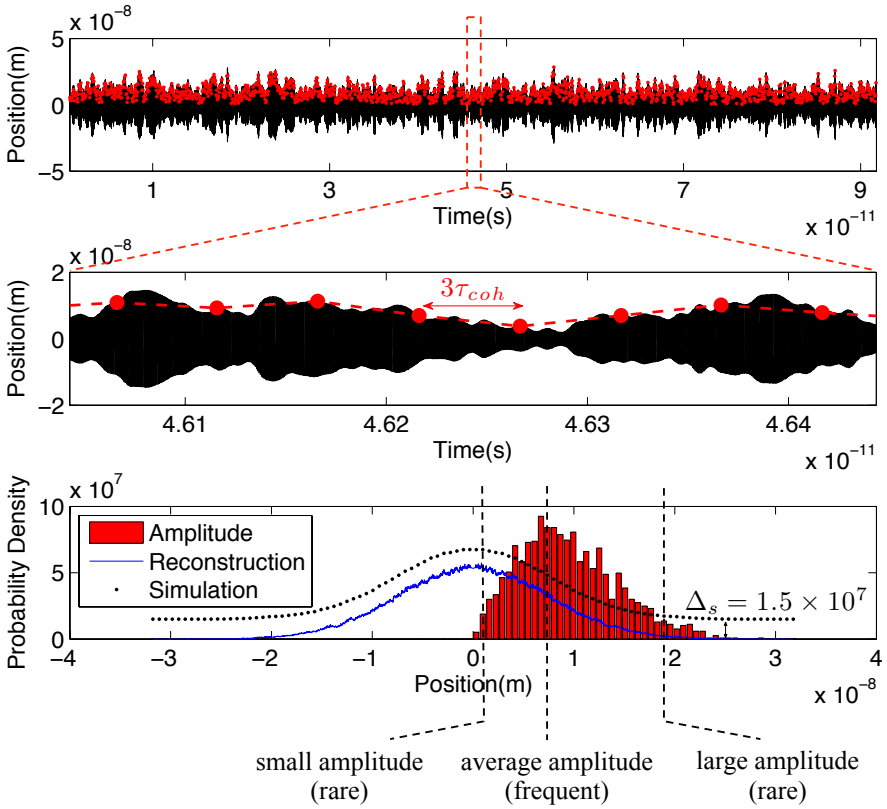


Figure 1.7: Sampled oscillation amplitude and the reconstructed Gaussian probability distribution. Top: The oscillation amplitudes (red dot) are sampled from a steady-state trajectory (black) with a sampling time-step equal to $3\tau_{coh}$, where $\tau_{coh}$ is the coherence time. Middle: A magnified section of the trajectory shows that the sampling time-step (red dot) is $3\tau_{coh}$. Bottom: Using the amplitude distribution (red bar), a probability distribution (blue line) is constructed and shown to agree with the simulated Gaussian probability distribution (black dot). The simulated probability distribution (black dot) is offset by $\Delta_s = 1.5\times10^7$ for better visualization. This result confirms that the underlying mechanism for the Gaussian probability distribution is the addition of a series of double-peak probability distributions according to the amplitude distribution given by the vacuum field. It is also worth noting that the most frequent oscillation amplitude in the amplitude distribution is at the half-maximum of the position distribution (black dot).

$\tilde{x}(t)$ into an amplitude term $A(t)$ and an oscillation term $e^{-i\omega_0 t}$,

$$\begin{aligned} \tilde{x}(t) &= A(t)e^{-i\omega_0 t}, \\ A(t) &= \sum_{\mathbf{k},\lambda} \left( \varepsilon_{\mathbf{k}\lambda,\mathrm{x}} \frac{q}{m} \sqrt{\frac{\hbar\omega}{\epsilon_0 V}} \frac{a_{\mathbf{k}\lambda}}{B_{\mathbf{k}\lambda}} \right) e^{-i(\omega-\omega_0)t}. \end{aligned} \tag{1.67}$$

The complex components $e^{-i(\omega-\omega_0)t}$ rotate in the complex plane at different rates $\omega - \omega_0$. At any given time, the configuration of these components determines the magnitude of $A(t)$, as shown in Figure 1.6. As time elapses, the configuration evolves and the amplitude $A(t)$ changes with time. When the elapsed time $\Delta t$ is much shorter than the shortest rotating period $2\pi/|\omega - \omega_0|_{max}$, the change in the amplitude $A(t)$ is negligible,

$$A(t + \Delta t) \simeq A(t) \quad \text{for} \quad \Delta t \ll \tau_{coh}, \tag{1.68}$$

where $\tau_{coh} = 2\pi/|\omega - \omega_0|_{max}$. Here we denote this shortest rotating period as coherence time[8] $\tau_{coh}$. For our problem at hand, it is clear that the sampling of oscillation amplitudes should use a time-step greater than $\tau_{coh}$.

A representative sampling of the oscillation amplitudes with each sampled amplitudes separated by $3\tau_{coh}$ is shown in Figure 1.7. In this figure, the histogram of the sampled oscillation amplitudes shows that the occurrence of large or small amplitudes is rare. Most of the sampled amplitudes have a medium value. This is because the occurrence of extreme values requires complete alignment or misalignment of the complex components in $A(t)$. For most of the time, the complex components are in partial alignment and thus give a medium value of $A(t)$. Interestingly, the averaged

[8] The coherence time $\tau_{coh}$ as defined here is equivalent to the temporal width of the first-order correlation function (autocorrelation). As the autocorrelation of the simulated trajectory is the Fourier transform of the spectrum according to the Wiener-Khinchin theorem, it has a temporal width the same as the coherence time $\tau_{coh}$ calculated here, as they are both inversely proportional to the spectral width.

value of $A(t)$ is close to the oscillation amplitude $x_0$ as predicted by the random walk model (Eq. (1.53)). Using the amplitude distribution given in Figure 1.7, a probability distribution can be constructed by adding up the double-peak probability distributions,

$$P(x) = \sum_A P_A(x) = \int P_A(x) f(A) dA, \tag{1.69}$$

where $A$ is oscillation amplitude, $f(A)$ is the amplitude distribution, and $P_A(x)$ is the corresponding double-peak probability distribution. This constructed probability distribution is a Gaussian and is identical to the simulation result shown in Figure 1.4. The reconstruction of the Gaussian probability distribution indicates the transition from the double-peak distribution to the Gaussian distribution as due to the amplitude modulation driven by the vacuum field.

### 1.4.2 Phase Averaging and Ensemble Sampling

In many SED analyses [4, 6, 7, 8, 10, 21], the procedure of random phase averaging is often used to obtain the statistical properties of the physical system. A proper comparison between numerical simulation and analysis should thus be based on ensemble sampling. In each realization of ensemble sampling, the particle is prepared with identical initial conditions, but the vacuum field differs in its initial random phase $\tilde{\theta}_{\mathbf{k}\lambda}$. The difference in the initial random phase $\tilde{\theta}_{\mathbf{k}\lambda}$ corresponds to the different physical realizations in random phase averaging. At the end of the simulation, physical quantities such as position and momentum are recorded from an ensemble of trajectories.

The ensemble sampling of the simulation gives the probability distributions in Figure 1.8. The position and momentum distributions satisfy the Heisenberg minimum uncertainty as predicted by the Boyer's analysis. In addition, Boyer proposed a

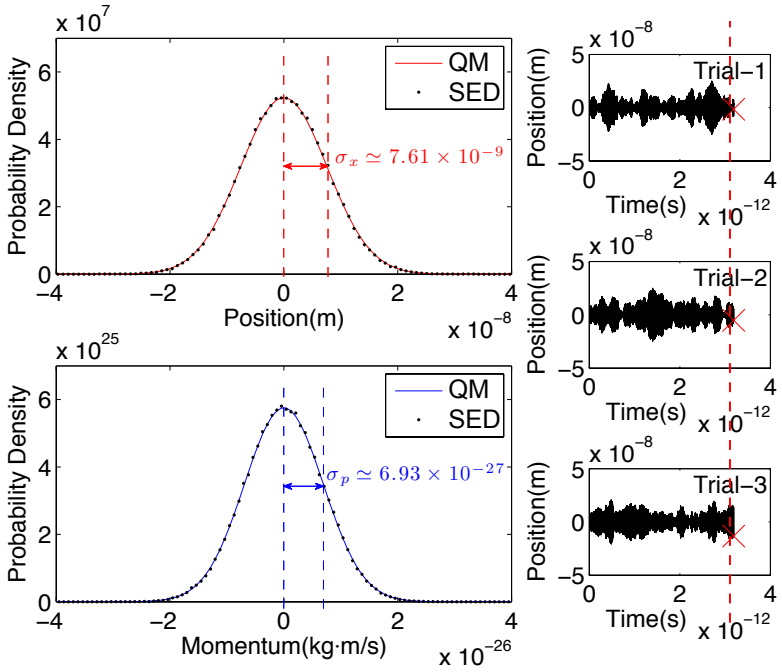


Figure 1.8: The probability distribution constructed from an ensemble sampling (number of particles $N_p = 2 \times 10^5$, number of sampled frequencies $N_\omega = 2 \times 10^3$). Left: The position and momentum probability distributions are shown for the SED harmonic oscillator (black dot) and the ground state quantum harmonic oscillator (red and blue line). The ensemble sampling corresponds to the procedure of random phase averaging (Eqs. (1.11) and (1.12)), so the width of the probability distributions should satisfy Heisenberg's minimum uncertainty relation ($\sigma_x \sigma_p = \hbar/2$) as predicted by the analysis. Right: An illustration of the ensemble sampling shows how positions (red cross) are recorded from an ensemble of trajectories (black line).

mechanism for the minimum uncertainty using an energy-balance argument. Namely, he calculated the energy gain from the vacuum field and the energy loss through radiation damping, and he found that the balance results in the minimum uncertainty relation [4]. We confirm this balancing mechanism by turning off the radiation damping in the simulation and see that the minimum uncertainty relation no long holds (see Figure 1.9).

Unlike sequential sampling, ensemble sampling has the advantage that the recorded data are fully uncorrelated. As a result, the integration time does not need to be very

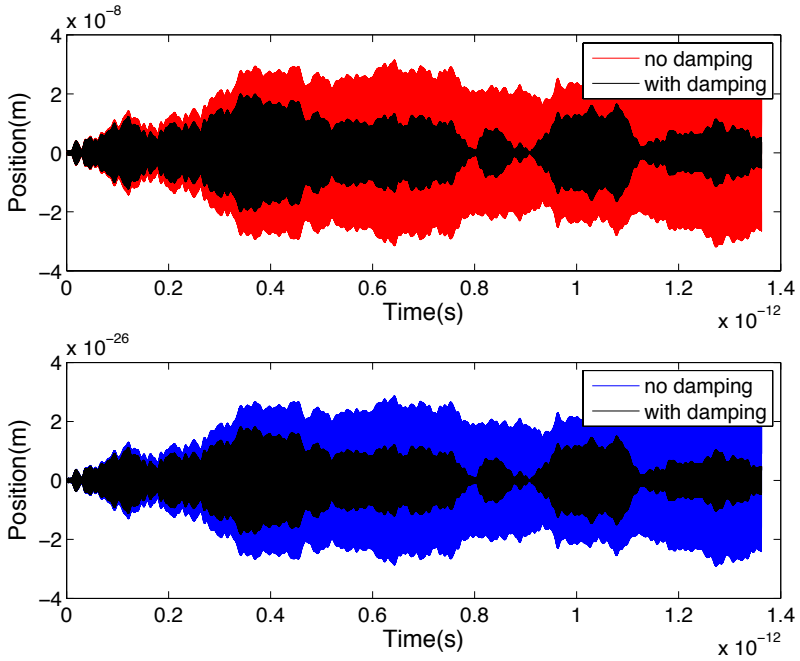


Figure 1.9: Radiation damping and Heisenberg's minimum uncertainty relation. Under the balance between vacuum field driving and the radiation damping, the trajectory of the SED harmonic oscillator (black) satisfies the Heisenberg minimum uncertainty relation. When the radiation damping is turned off in the simulation (red and blue), the minimum uncertainty relation no longer holds, although the range of the particle's motion is still bounded by the harmonic potential.

long compared to the coherence time $\tau_{coh}$. However, since only one data point is recorded from each trajectory, a simulation with ensemble sampling actually takes longer time than with sequential sampling. For example, a typical simulation run with sequential sampling takes 2.3 hours to finish (for number of sampled frequencies $N_\omega = 2 \times 10^4$), but with ensemble sampling it takes 61 hours (for number of particles $N_p = 2 \times 10^5$ and number of sampled frequencies $N_\omega = 5 \times 10^2$). A remedy to this problem is to use parallel computing for the simulation. The parallelization scheme[9] for our simulation with ensemble sampling is straightforward, since each trajectory

[9] The parallelization of the simulation program is developed and benchmarked with assistance from University of Nebraksa Holland Computing Center. The program is written in Fortran and parallelized using Message Passing Interface (MPI) [19, 22]. The compiler used in this work is the GNU Compiler Collection (GCC) `gcc-4.4.1` and the MPI wrapper used is `openmpi-1.4.3`.

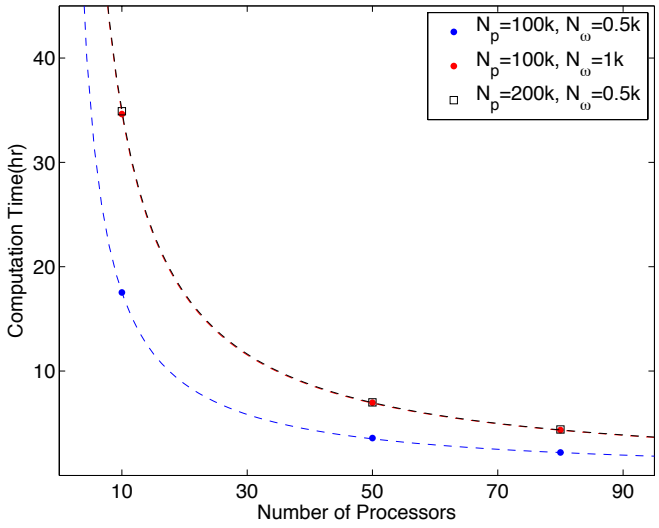


Figure 1.10: The inverse relation between the computation time and the number of processors. The data (black open square, blue and red dot) follow an inverse relation $y = C/x$ (black, blue and red dash line). The proportionality constant $C$ scales with the product of $N_p$ (number of particles) and $N_\omega$ (number of sampled frequencies). The larger the value of $N_p N_\omega$, the longer it takes to finish a simulation with a fixed number of processors.

are independent except for the random initial phases $\tilde{\theta}_{\mathbf{k}\lambda}$. To reduce the amount of interprocessor communication and computation overhead, each processor is assigned an equal amount of work. The parallelized program is benchmarked and shows an inverse relation between the computation time and the number of processors (see Figure 1.10). The computation speedup is defined as $S_p = T_1/T_p$, where $T_1$ is the single processor computation time and $T_p$ is the multi-processor computation time. The inverse relation ($T_p \propto 1/N_{proc}$)between the multi-processor computation time $T_p$ and the number of processors $N_{proc}$, as shown in Figure 1.10, implies a linear speedup, $S_p \propto N_{proc}$. As an additional note, the convergence of the ensemble-averaged energy to the analytical value is shown as a function of sampled frequency number in Figure 1.11. As highlighted in the figure, only $N_\omega = 5 \times 10^2$ sampled modes need to be used for the simulation to reproduce with the analytical result. The fact that $N_\omega$ is

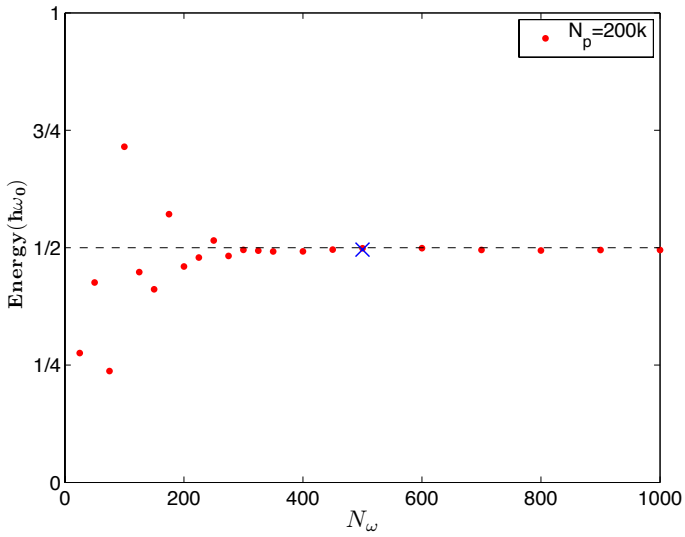


Figure 1.11: The ensemble-averaged energy of the SED harmonic oscillator and its convergence to the analytical value as a function of sampled frequency number $N_\omega$. The number of particles used in the simulation is $N_p = 2 \times 10^5$, and the sampled frequency range is $\Delta = 220 \times \Gamma\omega_0^2$. The energy converges as the number of sampled frequencies $N_\omega$ increases. At $N_\omega = 5 \times 10^2$ (blue cross), the deviation between the energy of the SED harmonic oscillator and the ground state energy of the quantum oscillator is 1%.

low indicates that our method of vacuum mode selection is effective.

## 1.5 Conclusions

The analytical probability distribution of an SED harmonic oscillator is obtained in Sec. 1.2. The details of our numerical methods including vacuum mode selection is documented in Sec. 1.3. Agreement is found between the simulation and the analytical results, as both sequential sampling and ensemble sampling give the same probability distribution as the analytical result (see Figure 1.4 and Figure 1.8). The analytical results such as the ensemble-averaged energy and the probability distribution are reproduced by the numerical simulation using a low number of sampled vacuum field mode ($N_\omega = 5{\times}10^2$), which is an indication that our method of vacuum mode selection

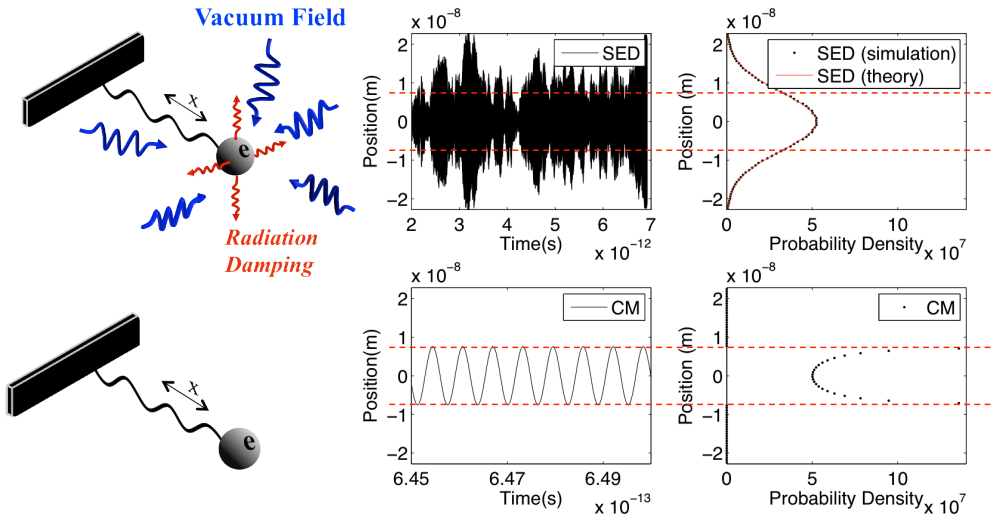


Figure 1.12: A comparison between the harmonic oscillators with and without the vacuum field. Top: Comparing to Figure 1.1, it is clear from this figure that the SED harmonic oscillator undergoes an oscillatory motion with modulating oscillation amplitude. The oscillation amplitude modulates at the time scale of coherence time $\tau_{coh}$ and is responsible for the resulting Gaussian probability distribution. Bottom: In the absence of the vacuum field or any external drive, a harmonic oscillator that is initially displaced from equilibrium performs a simple harmonic oscillation with constant oscillation amplitude. The resulting probability distribution has peaks at the two turning points.

(Eqs. (1.34), (1.35), (1.36), and Eq. (1.39)) is effective in achieving a representative sampling.

As the probability distribution constructed from a single trajectory is a Gaussian and satisfies the Heisenberg minimum uncertainty relation, we investigate the relation between the Gaussian probability distribution and the particle's dynamical properties. As a result, the amplitude modulation of the SED harmonic oscillator is found to be the cause for the transition from the double-peak probability distribution to the Gaussian probability distribution (see Figure 1.7).

## 1.6 Discussions: Application of Simulation to Other Physical Systems

In quantum mechanics, the harmonic oscillator has excited, coherent, and squeezed states. A natural extension of our current work is to search for the SED correspondence of such states. Currently, we are investigating how a Gaussian pulse with different harmonics of $\omega_0$ will affect the SED harmonic oscillator. Can the SED harmonic oscillator support a discrete excitation spectrum, and if so, how does it compare with the prediction from quantum mechanics? Such a study is interesting in the broader view of Milonni's comment that SED is unable to account for the discrete energy levels of interacting atoms [1], and also Boyer's comment that at present the line spectra of atoms is still unexplained in SED [23].

The methods of our numerical simulation may be applicable to study other quantum systems that are related to the harmonic oscillator, such as a charged particle in a uniform magnetic field and the anharmonic oscillator [6, 21]. For the first example, classically, a particle in a uniform magnetic field performs cyclotron motion. Such a system is a two-dimensional oscillator, having the natural frequency set by the Larmor frequency. On the other hand, a quantum mechanical calculation for the same system reveals Landau quantization. The quantum orbitals of cyclotron motion are discrete and degenerate. Such a system presents a challenge to SED. For the second example, a harmonic potential can be modified to include anharmonic terms of various strength. Heisenberg considered such a system a critical test in the early development of quantum mechanics [24, 25]. We think that a study of the anharmonic oscillator is thus a natural extension of our current study and may serve as a test for SED.

Lastly, over the last decades there has been a sustained interest to explain the

origin of electron spin and the mechanism behind the electron double-slit diffraction with SED [26, 27, 28, 29]. Several attempts were made to construct a dynamical model that accounts for electron spin. In 1982, de la Peña calculated the phase averaged mechanical angular momentum of a three-dimensional harmonic oscillator. The result deviates from the electron spin magnitude by a factor of 2 [26]. One year later, Sachidanandam derived the intrinsic spin one-half of a free electron in a uniform magnetic field [27]. Whereas Sachidanandam's calculation is based on the phase averaged canonical angular momentum, his result is consistent with Boyer's earlier work where Landau diamagnetism is derived via the phase averaged mechanical angular momentum of an electron in a uniform magnetic field [6]. Although these results are intriguing, the most important aspect of spin, the spin quantization, has not been shown. If passed through a Stern-Gerlach magnet, will the electrons in the SED description split into two groups of trajectories[10]? At this point, the dynamics becomes delicate and rather complex. To further investigate such a model of spin, a numerical simulation may be helpful.

On the other hand, over the years claims have been made that SED can predict double-slit electron diffraction [4, 28, 29]. In order to explain the experimentally observed electron double-slit diffraction[11] [36, 37, 38], different mechanisms motivated by SED were proposed [28, 29], but no concrete calculation have been given except for a detailed account of the slit-diffracted vacuum field [39]. In 1999, Kracklauer suggested that particles steered by the modulating waves of the SED vacuum field should display a diffraction pattern when passing through a slit, since the vacuum field itself is diffracted [28]. In recent years, another diffraction mechanism is proposed

[10] Electron Stern-Gerlach effect is an interesting but controversial topic in its own right. Whereas Bohr and Pauli asserted that an electron beam can not be separated by spin based on the concept of classical trajectories [30], Batelaan and Dehmelt argue that one can do so with certain Stern-Gerlach-like devices [31, 32, 33, 34].

[11] See [35] for a movie of the single electron buildup of a double-slit diffraction pattern.

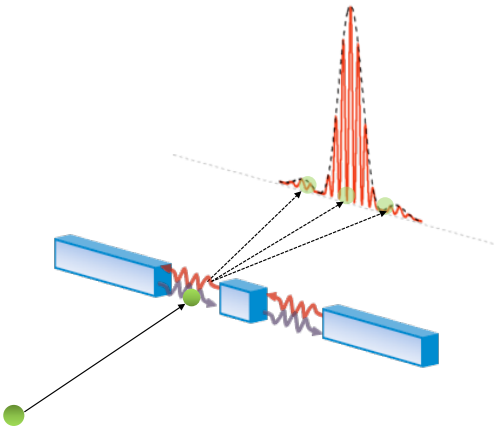

Figure 1.13: Schematic illustration of a vacuum field based mechanism for electron double-slit diffraction. Several authors have proposed different SED mechanisms that explain the electron double-slit diffraction. The central idea is that the vacuum field in one slit is affected by the presence the other slit. As the vacuum field perturbs the electron's motion, an electron passing through only one slit can demonstrate a dynamical behavior that reflects the presence of both slits. Such a mechanism may reconcile the superposition principle with the concept of particle trajectory.

by Cavalleri *et al.* in relation to a postulated electron spin motion [29]. Despite of these efforts, Boyer points out in a recent review article that at present there is still not a concrete SED calculation on the double-slit diffraction [23]. Boyer suggests that as the correlation function of the vacuum field near the slits is modified by the slit boundary, the motion of the electron near the slits should be influenced as well. Can the scattering of the vacuum field be the physical mechanism behind the electron double-slit diffraction (see Figure 1.13)? As Heisenberg's uncertainty relation is a central feature in all matter diffraction phenomena, any proposed mechanism for electron double-slit diffraction must be able to account for Heisenberg's uncertainty relation. In the physical system of the harmonic oscillator, SED demonstrates a mechanism that gives rise to the Heisenberg minimum uncertainty. We hope that the current simulation method may help providing a detailed investigation on the proposed SED mechanisms for the electron slit-diffraction.

# Bibliography

[1] P. W. Milonni, *The Quantum Vacuum: An Introduction to Quantum Electrodynamics* (Academic Press, Boston, 1994), pp. 290–294.

[2] W. E. Lamb Jr. and R. C. Retherford, *Fine Structure of the Hydrogen Atom by a Microwave Method*, *Phys. Rev.* **72**, 241 (1947).

[3] H. A. Bethe, *The Electromagnetic Shift of Energy Levels*, Phys. Rev. **72**, 339 (1947).

[4] T. H. Boyer, *Random electrodynamics: The theory of classical electrodynamics with classical electromagnetic zero-point radiation*, Phys. Rev. D **11**, 790 (1975).

[5] M. Ibison and B. Haisch, *Quantum and classical statistics of the electromagnetic zero-point field*, Phys. Rev. A **54**, 2737 (1996).

[6] T. H. Boyer, *Diamagnetism of a free particle in classical electron theory with classical electromagnetic zero-point radiation*, Phys. Rev. A **21**, 66 (1980).

[7] T. H. Boyer, *Thermal effects of acceleration through random classical radiation*, Phys. Rev. D **21**, 2137 (1980).

[8] T. H. Boyer, *Retarded van der Waals forces at all distances derived from classical electrodynamics with classical electromagnetic zero-point radiation*, Phys. Rev. A **7**, 1832 (1973).

[9] H. E. Puthoff, *Ground state of hydrogen as a zero-point-fluction-determined state*, Phys. Rev. D **35**, 3266 (1987).

[10] T. H. Boyer, *General connection between random electrodynamics and quantum electrodynamics for free electromagnetic fields and for dipole oscillator systems*, Phys. Rev. D **11**, 809 (1975).

[11] D. C. Cole and Y. Zou, *Quantum mechanical ground state of hydrogen obtained from classical electrodynamics*, Phys. Lett. A 317, 14 (2003).

[12] D. C. Cole and Y. Zou, *Simulation study of aspects of the classical hydrogen atom interacting with electromagnetic radiation: Elliptical orbits*, J. Sci. Comput **20**, 379 (2004).

[13] D. C. Cole and Y. Zou, *Simulation study of aspects of the classical hydrogen atom interacting with electromagnetic radiation: Circular orbits*, J. Sci. Comput. **20**, 43 (2004).

[14] T. W. Marshall, *Random Electrodynamics*, Proc. Roy. Soc. A **276**, 475 (1963).

[15] L. D. Landau and E. M. Lifshitz, *The Classical Theory of Fields*, 4th ed. (Pergamon Press, New York, 1987), p. 207, Eq. (75.10).

[16] J. D. Jackson, *Classical Electrodynamics*, 3rd ed. (Wiley, New York, 1998), p. 749, Eq. (16.10).

[17] E. Poisson, *An introduction to the Lorentz-Dirac equation*, http://arxiv.org/abs/gr-qc/9912045, (1999).

[18] G. Woan, *The Cambridge Handbook of Physics Formulas* (Cambridge University Press, New York, 2003), p. 59.

[19] W. H. Press, S. A. Teukolsky, W. T. Vetterling, and B. P. Flannery, *Numerical Recipes in Fortran 77: The Art of Scientific Computing*, 2nd ed. (Cambridge University Press, New York, 1996). For the uniform random number generator, we use "`ran1`" in p. 271. To solve the ordinary differentiation equation, we use the adaptive 5th order Cash-Karp Runge-Kutta method ("`odeint, rkqs, rkck`") in pp. 712–715, with accuracy parameter `esp` set to 0.001.

[20] S. T. Thornton and J. B. Marion, *Classical Dynamics of Particles and Systems*, 5th ed. (Brooks/Cole, Belmont, 2004), p.136.

[21] T. H. Boyer, *Equilibrium of random classical electromagnetic radiation in the presence of a nonrelativistic nonlinear electric dipole oscillator*, Phys. Rev. D **13**, 2832 (1976).

[22] P. S. Pacheco, *Parallel programming with MPI*, (Morgan Kaufmann, San Francisco, 1997).

[23] T. H. Boyer, *Any classical description of nature requires classical electromagnetic zero-point radiation*, Am. J. Phys. **79**, 1163 (2011).

[24] K. Gottfried, *P. A. M. Dirac and the discovery of quantum mechanics*, Am. J. Phys. **79**, 261 (2011).

[25] I. J. R. Aitchison, D. A. MacManus, and T. M. Snyder, *Understanding Heisenberg's "magical" paper of July 1925: A new look at the calculational details*, Am. J. Phys. **72**, 1370 (2004).

[26] L. de la Peña and A. Jáuregui, *The spin of the electron according to stochastic electrodynamics*, Found. Phys. **12**, 441(1982).

[27] S. Sachidanandam, *A derivation of intrinsic spin one-half from random electrodynamics*, Phys. Lett. A **97**, 323 (1983).

[28] A. F. Kracklauer, *Pilot wave steerage: A mechanism and test*, Found. Phys. Lett. **12**, 441 (1999).

[29] G. Cavalleri, F. Barbero, G. Bertazzi, E. Cesaroni, E. Tonni, L. Bosi, G. Spavieri and George Gillies, *A quantitative assessment of stochastic electrodynamics with spin (SEDS): Physical principles and novel applications*, Front. Phys. China **5**, 107 (2010).

[30] W. Pauli, *Proceedings of the Sixth Solvay Conference, 1930*, (Gauthier-Villars, Brussels, 1932), pp. 183–186, 217–220, 275–280.

[31] H. Batelaan, T. J. Gay, and J. J. Schwendiman, *Stern-Gerlach effect for electron beams*, Phys. Rev. Lett. **79**, 4517 (1997).

[32] G. A. Gallup, H. Batelaan, and T. J. Gay, *Quantum-mechanical analysis of a longitudinal Stern-Gerlach effect*, Phys. Rev. Lett. **86**, 4508 (2001).

[33] H. Dehmelt, *Experiments on the structure of an individual elementary particle*, Science **247**, 539 (1990).

[34] H. Dehmelt, *New continuous Stern-Gerlach effect and a hint of "the" elementary particle*, Zeit. f. Phys. **10**, 127 (1988).

[35] Double-slit experiment by R. Bach and H. Batelaan, highlighted in the video: *The Challenge of Quantum Reality*, produced by D. Pope, a film made by Perimeter Institute for Theoretical Physics (2009).

[36] C. Jönsson, *Elektroneninterferenzen an mehreren künstlich hergestellten Feinspalten* ,Z. Phys. **161**(4), 454 (1961).

[37] C. Jönsson, *Electron diffraction at multiple slits*, Am. J. Phys. **42**(1), 4 (1974).

[38] S. Frabboni, C. Frigeri, G. C. Gazzadi, and G. Pozzi, *Two and three slit electron interference and diffraction experiments*, Am. J. Phys. **79**, 615 (2011).

[39] J. Avendaño and L. de la Peña, *Reordering of the ridge patterns of a stochastic electromagnetic field by diffraction due to an ideal slit*, Phys. Rev. E **72**, 066605 (2005).

# Chapter 2

# Quantized Excitation Spectrum of a Classical Particle

The interaction between a light pulse and a classical harmonic oscillator in the vacuum field gives rises to a quantized excitation spectrum. Although quantized spectra are common in nonlinear classical systems, this result is interesting given that the magnitude of excitation peaks agree with those predicted by quantum mechanics.

## 2.1 Introduction

Historically, the discreteness of atomic spectra motivated the early development of quantum mechanics. Because quantum mechanics has made numerous successful predictions on atomic spectra, conventionally the discrete atomic spectrum is attributed to transitions between the quantized energy levels of an atom. Classical theories, such as stochastic electrodynamics (SED), are usually thought of as incapable of generating discrete atomic spectra, or any discrete spectra of the quantum mechanical bound states. Indeed, Peter W. Milonni has commented in his well-known book *The Quantum Vacuum* that "Being a purely classical theory of radiation and matter, SED is unable ... to account for the discrete energy levels of the interacting atoms." [1].

In the case of the harmonic oscillator, quantum mechanics predicts an integer-spaced excitation spectrum, but classical mechanics only supports a single resonance at the oscillator's natural frequency. In this report, we investigate the excitation spectrum of a semi-1D classical harmonic oscillator immersed in the classical electromagnetic zero-point radiation, or the vacuum field. The vacuum field as defined in SED is a nonzero homogenous solution to the Maxwell's equations [2, 3]. The Planck constant $\hbar$ is brought into the classical vacuum field as an overall factor that sets the field strength. Our simulation and perturbation analysis show that a classical harmonic oscillator in the vacuum field exhibits the same integer-spaced, or "quantized", excitation spectrum as its quantum counterpart. The organization of this paper is the following. First, the theories for both driven quantum and classical oscillators are provided. Then, the excitation spectra of the quantum and classical systems are obtained through numerically solving the equation of motion. A classical perturbative analysis is also given to provide insights to the underlying mechanism of the integer-spaced excitation spectrum of the classical oscillator. At the end, the implications of

our results are discussed.

## 2.2 Quantum Harmonic Oscillator

A semi-1D driven quantum harmonic oscillator can be constructed from an anisotropic 3D driven quantum harmonic oscillator. Treating the driving field as classical, the Hamiltonian for the 3D driven quantnum harmonic oscillator has the form [4]

$$\widehat{H}_{qm} = \frac{\left(\hat{\mathbf{p}} - q\mathbf{A}_p(\hat{\mathbf{r}}, t)\right)^2}{2m} + q\phi_p(\hat{\mathbf{r}}, t) + \frac{m\omega_x^2}{2}\hat{x}^2 + \frac{m\omega_y^2}{2}\hat{y}^2 + \frac{m\omega_z^2}{2}\hat{z}^2, \tag{2.1}$$

where $\hat{\mathbf{p}} = -i\hbar\nabla = (\hat{p}_x, \hat{p}_y, \hat{p}_z)$, $\hat{\mathbf{r}} = (\hat{x}, \hat{y}, \hat{z})$, $m$ is the mass, $q$ is the charge of the harmonic oscillator, and $(\phi_p, \mathbf{A}_p)$ is the driving field. The anisotropic harmonic oscillator has natural frequencies $\omega_x \equiv \omega_0$ and $\omega_y = \omega_z \equiv \omega_s$ for the harmonic potentials along the $x$, $y$, and $z$ axes. The use of the Coulomb gauge ($\nabla \cdot \mathbf{A}_p = 0$) makes $\phi_p = 0$ in the absence of external charges and also $\hat{\mathbf{p}} \cdot \mathbf{A}_p = \mathbf{A}_p \cdot \hat{\mathbf{p}}$. Therefore, under the Coulomb gauge the Hamiltonian in Eq. (2.1) can be written as

$$\widehat{H}_{qm} = \left(\widehat{H}_x + \widehat{H}_y + \widehat{H}_z\right) + \widehat{H}', \tag{2.2}$$

where the unperturbed Hamiltonians are

$$\begin{aligned} \widehat{H}_x &\equiv \frac{\hat{p}_x^2}{2m} + \frac{m\omega_0^2}{2}\hat{x}^2, \\ \widehat{H}_y &\equiv \frac{\hat{p}_y^2}{2m} + \frac{m\omega_s^2}{2}\hat{y}^2, \\ \widehat{H}_z &\equiv \frac{\hat{p}_z^2}{2m} + \frac{m\omega_s^2}{2}\hat{z}^2, \end{aligned} \tag{2.3}$$

and the interaction Hamiltonian is

$$\widehat{H}' = -\frac{q}{2m}\left(2\mathbf{A}_p \cdot \hat{\mathbf{p}} - q\mathbf{A}_p^2\right). \tag{2.4}$$

In our study, a propagating Gaussian pulse is used as the driving field,

$$\mathbf{A}_p = A_p \cos\left(\mathbf{k}_p \cdot \hat{\mathbf{r}} - \omega_p \tau\right) \exp\left[-\left(\frac{\mathbf{k}_p \cdot \hat{\mathbf{r}}}{|\mathbf{k}_p|\Delta x} - \frac{\tau}{\Delta t}\right)^2\right] \boldsymbol{\varepsilon}_p, \tag{2.5}$$

where $\tau \equiv t - t_0$, is used for excitation. The temporal width of the pulse is $\Delta t$, and the spatial width is $\Delta x = c\Delta t$. The wave vector of the carrier wave is denoted as $\mathbf{k}_p = \omega_p/c\,(\sin\theta_p, 0, \cos\theta_p)$, and the field polarization is $\boldsymbol{\varepsilon}_p = (\cos\theta_p, 0, -\sin\theta_p)$. In the simulation, the field amplitude is chosen to be $A_p = 1.5 \times 10^{-9}$Vs/m, and the polarization angle is $\theta_p = \pi/4$. While the unperturbed Hamiltonian in Eq. (2.3) defines a unperturbed basis states for the oscillator, the interaction Hamiltonian in Eq. (2.4) can induce transitions between these basis states. The energy levels of the oscillator are

$$E_{nmk} = E_n + E_m + E_k, \tag{2.6}$$

where $E_n = \hbar\omega_0(n + 1/2)$, $E_m = \hbar\omega_s(m + 1/2)$, and $E_k = \hbar\omega_s(k + 1/2)$ are the eigenvalues to the unperturbed Hamiltonians. A transition between the state $|nmk\rangle$ and the state $|abc\rangle$ occurs when $|E_{abc} - E_{nmk}| = j\hbar\omega_p$. Here the parameter $j$ signifies a $j$-th order process. Assuming $\omega_s \gg \omega_0$ and $w_p \simeq \omega_0$, a high-order processes ($j \gg 1$) is required to drive any $\Delta m > 0$ or $\Delta k > 0$ transitions. Given the parameters in our simulation, only the lowest excited states $|n00\rangle$ with eigen-energies $E_{n00} = E_n + \hbar\omega_s$ will be considered. Therefore, the 3D anisotropic harmonic oscillator can be seen as a semi-1D oscillator in the $x$-direction, constrained by the strong potentials in the $y$- and $z$-direction.

As only $|n00\rangle$ states will be considered, we let $\hat{\mathbf{p}} = \hat{p}_x \boldsymbol{\varepsilon}_x$ and $\hat{\mathbf{r}} = \hat{x}\boldsymbol{\varepsilon}_x$, in the Hamiltonian to simplify the notation. The unit vector $\boldsymbol{\varepsilon}_x$ is along the $x$-direction, $\boldsymbol{\varepsilon}_x = (1, 0, 0)$. The oscillator is initially in the ground state. After excitation the state $|\psi\rangle$(t) becomes a superposition of $N$ eigenstates $|n00\rangle$,

$$|\psi\rangle(t) = \sum_{n=1}^{N} c_n |n00\rangle e^{-i\omega_n t} e^{-i\omega_s t}, \tag{2.7}$$

where $\omega_n = \omega_0(n + 1/2)$. To obtain the coefficients of the excited state $|\psi\rangle$(t), we solve the Schrödinger equation,

$$\frac{d}{dt}C(t) = -\frac{i}{\hbar}H^{'}C(t), \tag{2.8}$$

where $C(t)$ is a $N \times 1$ matrix and $H^{'}$ is a $N \times N$ matrix,

$$C = \begin{pmatrix} c_1(t) \\ c_2(t) \\ \vdots \\ c_N(t) \end{pmatrix}, \quad H^{'} = \begin{pmatrix} & \cdots & \\ \vdots & H^{'}_{nm} e^{i\omega_{nm}t} & \vdots \\ & \cdots & \end{pmatrix}. \tag{2.9}$$

For each element in the matrix $H^{'}$, $H^{'}_{nm} = \langle n00|\widehat{H}^{'}|m00\rangle$ and $\omega_{nm} \equiv \omega_n - \omega_m$. The total number of energy levels is chosen to be $N = 20$ for the given parameters, so that the population of the highest energy state is close to zero. Since resonances at higher-harmonics depends critically on the spatial nonlinearity of the pulse field, the dipole approximation is not sufficient for the study of the excitation spectrum, making a numerical approach to this problem convenient. In the simulation, the spatial dependence of the pulse field $\mathbf{A}_p$ is multipole-expanded up to the $20th$-order. Higher-order expansion does not change the computed excitation spectrum. Lastly,

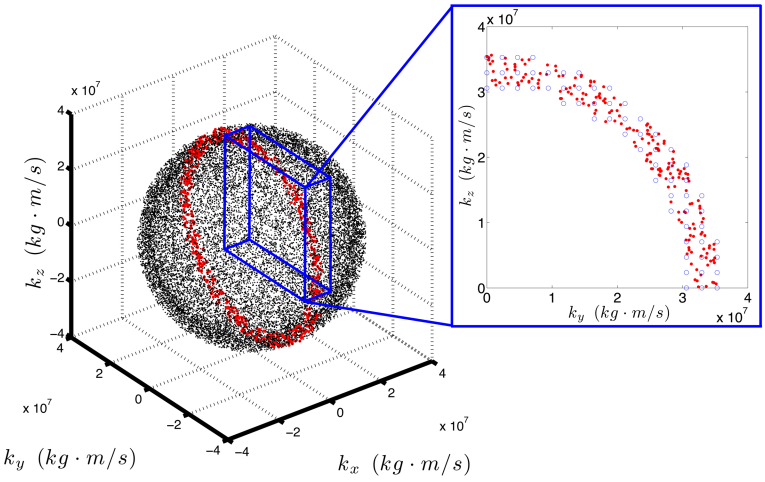


Figure 2.1: The sampled vacuum field modes in **k**-space. Left: The sampled vacuum field modes (black dots) are distributed in a spherical shell with thickness $\Delta/c$. The number of sampled modes shown here is $N_\omega = 2 \times 10^4$. A slice of the spherical shell at $\mathbf{k}_x \simeq 0$ is highlighted (red dots). Right: A quarter of the highlighted slice (red dots) is projected on the $k_y k_z$-plane. The modes sampled with cartesian sampling (blue circles) are shown for comparison.

the matrix element of the operators $\hat{x}$ and $\hat{p}_x$ are specified by

$$\begin{aligned} \langle n00|\hat{x}|m00\rangle &= \sqrt{\frac{\hbar}{2m\omega_0}}\left(\sqrt{n}\delta_{m,n-1} + \sqrt{n+1}\delta_{m,n+1}\right) \\ \langle n00|\hat{p}_x|m00\rangle &= i\sqrt{\frac{\hbar m\omega_0}{2}}\left(\sqrt{n}\delta_{m,n-1} - \sqrt{n+1}\delta_{m,n+1}\right). \end{aligned} \tag{2.10}$$

## 2.3 Classical Harmonic Oscillator in the Vacuum Field

In the classical case, a similar construction can be done to construct a semi-1D driven classical harmonic oscillator. To account for the vacuum field and the radiation reaction, the additional field Hamiltonian $H_F = \dfrac{\epsilon_0}{2}\displaystyle\int d^3\mathbf{r}\left(|\mathbf{E}_p + \mathbf{E}_{vac}|^2 + c^2\,|\mathbf{B}_p + \mathbf{B}_{vac}|^2\right)$ needs to be included. Having a semi-1D harmonic oscillator immersed in the vacuum

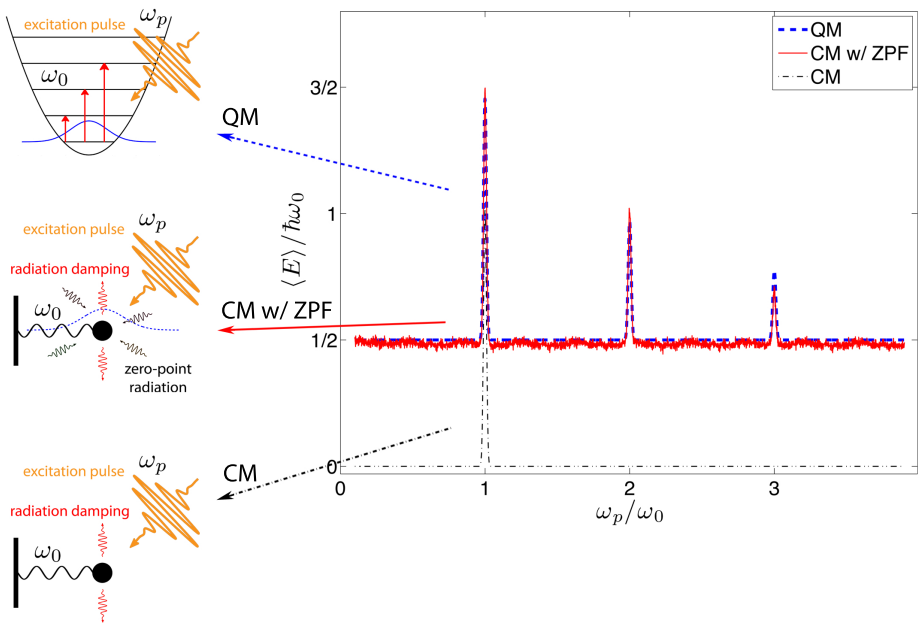


Figure 2.2: The excitation spectra of harmonic oscillators in different theories. Left: Schematics of harmonic oscillators are shown for quantum theory (left-top), for classical theory as modified by the vacuum field, or zero-point field (ZPF) (left-middle), and for the standard classical theory (left-bottom). Right: The averaged value of energy $\langle E \rangle$ after excitation is plotted as a function of pulse frequency $\omega_p$. For the classical theory, the ensemble average is computed. For the quantum theory, the expectation value is computed. The classical oscillator in the vacuum field (red solid line) exhibits an excitation spectrum in agreement with the quantum result (blue broken line). The number of vacuum field modes used in this simulation is $N_\omega = 500$. In the absence of the vacuum field, the classical oscillator has only one single resonance peak at the natural frequency $\omega_0$ (black dotted line). The excitation peak heights and the relative ratio are confirmed by the classical perturbation analysis.

field, the classical Hamiltonian is

$$H_{cl} = \left( \frac{p_x^2}{2m} + \frac{m\omega_0^2}{2} x^2 \right) - \frac{q}{2m} \left( 2\mathbf{A} \cdot \mathbf{p} - q\mathbf{A}^2 \right) + H_F, \tag{2.11}$$

where $\mathbf{A} = \mathbf{A}_p + \mathbf{A}_{vac}$, $\mathbf{p} = p_x \boldsymbol{\varepsilon}_x$, and $\mathbf{r} = x\boldsymbol{\varepsilon}_x$. The vacuum field is specified by

$$\mathbf{A}_{vac} = \sum_{\mathbf{k},\lambda} \sqrt{\frac{\hbar}{\epsilon_0 V \omega}} \cos\left(\mathbf{k} \cdot \mathbf{r} - \omega t + \tilde{\theta}_{\mathbf{k}\lambda}\right) \boldsymbol{\varepsilon}_{\mathbf{k}\lambda}, \tag{2.12}$$

where $\omega = c|\mathbf{k}|$, $\tilde{\theta}_{\mathbf{k}\lambda}$ is the random phase uniformly distributed in $[0, 2\pi]$, and $V$ is the physical volume occupied by the vacuum field. The two unit vectors, $\boldsymbol{\varepsilon}_{\mathbf{k},1}$ and $\boldsymbol{\varepsilon}_{\mathbf{k},2}$, describe a mutually orthogonal polarization basis in a plane perpendicular to the wave vector $\mathbf{k}$. The pulse field $\mathbf{A}_p$ is identical to that in Eq. (2.5) except for $\mathbf{r}$ being a classical quantity rather than an operator,

$$\mathbf{A}_p = A_p \cos\left(\mathbf{k}_p \cdot \mathbf{r} - \omega_p \tau\right) \exp\left[-\left(\frac{\mathbf{k}_p \cdot \mathbf{r}}{|\mathbf{k}_p|\Delta x} - \frac{\tau}{\Delta t}\right)^2\right] \boldsymbol{\varepsilon}_p. \tag{2.13}$$

From the Hamiltonian, the classical equation of motion follows,

$$m\ddot{x} = -m\omega_0^2 x + m\Gamma\dddot{x} + q\Big[\Big(E_{p,\mathrm{x}} + E_{vac,\mathrm{x}}\Big) + \Big(\mathbf{v} \times (\mathbf{B}_p + \mathbf{B}_{vac})\Big)_{\mathrm{x}}\Big], \tag{2.14}$$

where $\Gamma \equiv \dfrac{2q^2}{3mc^3}\dfrac{1}{4\pi\epsilon_0}$ and $m\Gamma\dddot{x}$ represents the radiation reaction field [5, 6]. Under the Coulomb gauge, the electric field is given by $\mathbf{E} = -\dfrac{\partial \mathbf{A}}{\partial t}$ and the magnetic field by $\mathbf{B} = \nabla \times \mathbf{A}$. Because $\mathbf{v} = \boldsymbol{\varepsilon}_x p_x/m$, the magnetic part of the Lorentz force is zero. To avoid numerical runaway solutions, we assume the point-particle description of the charged particle and make the usual approximation $m\Gamma\dddot{x} \simeq -m\Gamma\omega_0^2\dot{x}$ for numerical simulation [7, 8].

To carry out the simulation, an isotropic sampling of $N_\omega$ vacuum field modes $(\mathbf{k}_i, \lambda)$ is needed. The wave vectors $\mathbf{k}_i$ are chosen to have frequencies within the finite range $[\omega_0 - \Delta/2, \omega_0 + \Delta/2]$, where $\Delta$ is the vacuum field frequency bandwidth and it is chosen to be $\Delta = 2.2 \times 10^2 \Gamma\omega_0^2$, much larger than the oscillator's resonance bandwidth $\Gamma\omega_0^2$. The vacuum field modes in $\mathbf{k}$-space are sampled in spherical coordinates. In the following, we give the specific steps of the sampling method. For $i = 1 \ldots N_\omega$, the

wave vector are sampled by

$$\mathbf{k}_i = \begin{pmatrix} k_i \sin\theta_i \cos\phi_i \\ k_i \sin\theta_i \sin\phi_i \\ k_i \cos\theta_i \end{pmatrix}, \tag{2.15}$$

where

$$\begin{cases} k_i = (3\kappa_i)^{1/3} \\ \theta_i = \cos^{-1}(\vartheta_i) \\ \phi_i = \varphi_i, \end{cases} \tag{2.16}$$

and

$$\begin{cases} \kappa_i = (\omega_0 - \Delta/2)^3/3c^3 + (i-1)\Delta\kappa \\ \vartheta_i = R_i^{(1)} \\ \varphi_i = R_i^{(2)}. \end{cases} \tag{2.17}$$

The random number $R_i^{(1)}$ is uniformly distributed in $[-1, 1]$, and $R_i^{(2)}$ is another random number uniformly distributed in $[0, 2\pi]$. The stepsize $\Delta\kappa$ is specified by $\Delta\kappa = \Big[(\omega_0 + \Delta/2)^3 - (\omega_0 - \Delta/2)^3\Big] / \Big[3c^3(N_\omega - 1)\Big]$. Finally, the polarization vectors are sampled by

$$\boldsymbol{\varepsilon}_{\mathbf{k},1} = \begin{pmatrix} \cos\theta_i \cos\phi_i \cos\chi_i - \sin\phi_i \sin\chi_i \\ \cos\theta_i \sin\phi_i \cos\chi_i + \cos\phi_i \sin\chi_i \\ -\sin\theta_i \cos\chi_i \end{pmatrix},$$

$$\boldsymbol{\varepsilon}_{\mathbf{k},2} = \begin{pmatrix} -\cos\theta_i \cos\phi_i \sin\chi_i - \sin\phi_i \cos\chi_i \\ -\cos\theta_i \sin\phi_i \sin\chi_i + \cos\phi_i \cos\chi_i \\ \sin\theta_i \sin\chi_i \end{pmatrix}. \tag{2.18}$$

Such a sampling method is computationally convenient in describing the wave vectors $\mathbf{k}_i$ within certain frequency range (see Figure 2.1). The volume factor V in the vacuum field strength $\sqrt{\frac{\hbar}{\epsilon_0 V \omega}}$ can be estimated by $V \simeq (2\pi)^3 N_\omega / V_{\mathbf{k}}$. Here, the $\mathbf{k}$-space volume $V_{\mathbf{k}} = 4\pi/3c^3\Big[(\omega_0 + \Delta/2)^3 - (\omega_0 - \Delta/2)^3\Big]$ encloses the sampled vacuum field modes $\mathbf{k}_i$ in the spherical shell $\Big[(\omega_0 - \Delta/2)/c, (\omega_0 + \Delta/2)/c\Big]$.

We give the simulation result for the excitation spectrum in Figure 2.2. When the vacuum field is absent, the classical harmonic oscillator has only a single resonance at its natural frequency. With the vacuum field acting as a background perturbation, the classical harmonic oscillator exhibits a integer-spaced excitation spectrum, or if one likes, a "quantized" excitation spectrum. The position and the magnitude of the resonance peaks are in agreement with the quantum mechanical result.

## 2.4 Analysis and Mechanism

Such an agreement between the classical theory (as modified by the vacuum field) and quantum mechanics appears to be astonishing, given that the theory is fully classical and no quantization condition is added. While the quantized excitation spectrum of a quantum harmonic oscillator is explained by the intrinsic quantized energy levels, the quantized excitation of the classical harmonic oscillator is a result of nonlinearity. In the simulation, we can turn on and off the spatial dependence of either the vacuum field or the pulse field. The excitation spectrum was unaffected when only the spatial dependence of the vacuum field is turned off. When turning off only the spatial dependence of the pulse field, the excitation at the higher-harmonics completely disappear. Moreover, the magnitude of the excitation peak at $\omega_0$ is also affected. This suggests that the occurrence of the integer-spaced excitation spectrum is solely due to the spatial nonlinearity of the pulse field. To support this idea, we

consider a classical harmonic oscillator subject to only the pulse field,

$$m\ddot{x} = -m\omega_0^2 x + qE_p(x,t), \tag{2.19}$$

where $E_p(x,t) = E_0 \sin(k_p x - \omega_p \tau) \exp(-\tau^2/\Delta t^2)$, $E_0 = -A_p \omega_p \cos(\theta_p)$, and $k_p = \omega/c_p \sin(\theta_p)$. The spatial dependence in the pulse field can be Taylor expanded around $k_p x = 0$,

$$E_p(x,t) \simeq E_{1\omega_0}(x,t) + E_{2\omega_0}(x,t) + E_{3\omega_0}(x,t), \tag{2.20}$$

where

$$\begin{aligned} E_{1\omega_0}(x,t) &= -E_0 \sin(\omega_p \tau) \exp(-\tau^2/\Delta t^2), \\ E_{2\omega_0}(x,t) &= (k_p x) E_0 \cos(\omega_p \tau) \exp(-\tau^2/\Delta t^2), \\ E_{3\omega_0}(x,t) &= \left(\frac{k_p^2 x^2}{2}\right) E_0 \sin(\omega_p \tau) \exp(-\tau^2/\Delta t^2). \end{aligned} \tag{2.21}$$

To show that the three interaction terms in Eq. (2.21) correspond to excitation at the harmonics $1\omega_0$, $2\omega_0$, and $3\omega_0$, three equations of motion are solved in the following with individual interaction terms as the driving field. The equation for $1\omega_0$-excitation is given by,

$$\begin{aligned} m\ddot{x}_{1\omega_0} &= -m\omega_0^2 x_{1\omega_0} + qE_{1\omega_0}(x,t) \\ &= -m\omega_0^2 x_{1\omega_0} - qE_0 \sin(\omega_p \tau) \exp(-\tau^2/\Delta t^2). \end{aligned} \tag{2.22}$$

The full solution to this equation can be found as [9]

$$x_{1\omega_0} = x_{1c} + x_{1p}, \tag{2.23}$$

with

$$\begin{aligned} x_{1c}(t) &= D_0 \cos(\omega_0 t + \varphi_0), \\ x_{1p}(t) &= -\int_0^\infty d\omega f_1(\omega) \sin(\omega\tau), \end{aligned} \tag{2.24}$$

where

$$\begin{aligned} f_1(\omega) &\equiv \frac{\Delta t}{2\sqrt{\pi}} \frac{qE_0}{m(\omega_0^2 - \omega^2)} \exp\left[ -\left( \frac{\omega - \omega_p}{2/\Delta t} \right)^2 \right], \\ D_0 &= \sqrt{(x_0 - x_p(0))^2 + (v_0 - v_p(0))^2/\omega_0^2}, \\ \cos(\varphi_0) &= (x_0 - x_p(0))/D_0, \\ \sin(\varphi_0) &= -(v_0 - v_p(0))/D_0\omega_0. \end{aligned} \tag{2.25}$$

Here we assume the classical harmonic oscillator has the initial position $x_0$ and velocity $v_0$. The equation for $2\omega_0$-excitation is given by

$$\begin{aligned} m\ddot{x}_{2\omega_0} &= -m\omega_0^2 x_{2\omega_0} + qE_{2\omega_0}(x,t) \\ &= -m\omega_0^2 x_{2\omega_0} + q(k_p x)E_0 \cos(\omega_p \tau) \exp(-\tau^2/\Delta t^2). \end{aligned} \tag{2.26}$$

This equation is solved with a perturbation method up to the first-order in $\varepsilon \equiv qE_0\lambda_0/mc^2$,

$$x_{2\omega_0} \simeq x_{2c}^{(0)} + \varepsilon \left( x_{2c}^{(1)} + x_{2p}^{(1)} \right), \tag{2.27}$$

with

$$\begin{aligned} x_{2c}^{(0)}(t) &= A_0 \cos(\omega_0 t + \phi_0), \\ x_{2c}^{(1)}(t) &= B_0 \cos(\omega_0 t + \xi_0), \\ x_{2p}^{(1)}(t) &= \left( \frac{k_p A_0}{2\varepsilon} \right) \int_0^\infty d\omega f_2(\omega) \cos(\omega\tau - \omega_0 t_0 - \phi_0), \end{aligned} \tag{2.28}$$

where

$$
\begin{aligned}
&f_2(\omega) \equiv \frac{\Delta t}{2\sqrt{\pi}} \frac{qE_0}{m(\omega_0^2 - \omega^2)} \exp\left[ -\left( \frac{\omega - (\omega_p - \omega_0)}{2/\Delta t} \right)^2 \right], \\
&A_0 = \sqrt{x_0^2 + v_0^2/\omega_0^2}, \\
&\cos(\phi_0) = x_0/A_0, \\
&\sin(\phi_0) = -v_0/(A_0\omega_0), \\
&B_0 = \sqrt{(x_p^{(1)}(0))^2 + (v_p^{(1)}(0)/\omega_0)^2}, \\
&\cos(\xi_0) = -x_p^{(1)}(0)/B_0, \\
&\sin(\xi_0) = v_p^{(1)}(0)/B_0\omega_0.
\end{aligned}
\tag{2.29}
$$

Again, $\omega_0$ and $v_0$ are the initial conditions as defined previously. The equation for $3\omega_0$-excitation is given by

$$
\begin{aligned}
m\ddot{x}_{3\omega_0} &= -m\omega_0^2 x_{3\omega_0} + qE_{3\omega_0}(x,t) \\
&= -m\omega_0^2 x_{3\omega_0} + q\left( \frac{k_p^2 x^2}{2} \right) E_0 \sin(\omega_p \tau) \exp(-\tau^2/\Delta t^2).
\end{aligned}
\tag{2.30}
$$

The perturbative solution to is solved to the first-order in $\eta \equiv qE_0A_0/mc^2$,

$$
x_{3\omega_0} \simeq x_{3c}^{(0)} + \eta\left( x_{3c}^{(2)} + x_{3p}^{(2)} \right), \tag{2.31}
$$

with

$$
\begin{aligned}
&x_{3c}^{(0)}(t) = A_0 \cos(\omega_0 t + \phi_0), \\
&x_{3c}^{(2)}(t) = C_0 \cos(\omega_0 t + \zeta_0), \\
&x_{3p}^{(2)}(t) = \left( \frac{k_p^2 A_0^2}{8\eta} \right) \int_0^\infty d\omega f_3(\omega) \sin(\omega\tau - 2\omega_0 t_0 - 2\phi_0),
\end{aligned}
\tag{2.32}
$$

where,

$$
\begin{aligned}
&f_3(\omega) = \frac{\Delta t}{2\sqrt{\pi}} \frac{qE_0}{m(\omega_0^2 - \omega^2)} \exp\left[ - \left( \frac{\omega - (\omega_p - 2\omega_0)}{2/\Delta t} \right)^2 \right], \\
&A_0 = \sqrt{x_0^2 + v_0^2/\omega_0^2}, \\
&\cos(\phi_0) = x_0/A_0, \\
&\sin(\phi_0) = -v_0/(A_0\omega_0), \\
&C_0 = \sqrt{(x_p^{(2)}(0))^2 + (v_p^{(2)}(0)/\omega_0)^2}, \\
&\cos(\zeta_0) = -x_p^{(2)}(0)/C_0, \\
&\sin(\zeta_0) = v_p^{(2)}(0)/C_0\omega_0.
\end{aligned}
\tag{2.33}
$$

The total energy change of the harmonic oscillators as described in Eq. (2.22), (2.26), and (2.30) can be calculated through $\Delta E_\omega = \int_{-\infty}^{+\infty} qE_\omega(x_\omega, t)v_\omega(t)\,dt$, where $\omega = 1\omega_0$, $2\omega_0$, or $3\omega_0$. Using the solutions given above, the energy changes can be obtained for $\omega_p \simeq 1\omega_0$, $2\omega_0$, and $3\omega_0$ respectively,

$$
\begin{aligned}
\Delta E_{\omega_0} &= \frac{\sqrt{\pi}}{2}(A_0\omega_0)(qE_0\Delta t) \exp\left[ - \left( \frac{w_p - \omega_0}{2/\Delta t} \right)^2 \right] \cos(\omega_0 t_0 + \phi_0), \\
\Delta E_{2\omega_0} &= -\frac{\sqrt{\pi}}{4}(k_p A_0)(A_0\omega_0)(qE_0\Delta t) \exp\left[ - \left( \frac{w_p - 2\omega_0}{2/\Delta t} \right)^2 \right] \Big[ \sin(2\omega_0 t_0 + 2\phi_0) \\
&\quad + 2\frac{\varepsilon B_0}{A_0} \sin(2\omega_0 t_0 + \xi_0 + \phi_0) \Big], \\
\Delta E_{3\omega_0} &= -\frac{\sqrt{\pi}}{8} \left( \frac{k_p A_0}{2} \right) (A_0\omega_0)(qE_0\Delta t) \exp\left[ - \left( \frac{w_p - 3\omega_0}{2/\Delta t} \right)^2 \right] \Big[ \cos(3\omega_0 t_0 + 3\phi_0) \\
&\quad + 3\frac{\eta C_0}{A_0} \cos(3\omega_0 t_0 + 2\phi_0 + \zeta_0) \Big].
\end{aligned}
\tag{2.34}
$$

As a result, the excitation at $1\omega_0$ is due to the harmonic resonance of the oscillator with the driving pulse frequency, while excitation at $2\omega_0$ and $3\omega_0$ is due to parametric resonance [10, 11]. For the regular harmonic resonance, the energy change $\Delta E_{1\omega_0}$ is independent of the initial conditions. However, for parametric resonance the energy charges $\Delta E_{2\omega_0}$ and $\Delta E_{3\omega_0}$ depend on the initial conditions. If we assume that the initial conditions are given by the oscillator ensemble in the vacuum field, as provided by the numerical solutions of Eq. (2.14) in the absence of the pulse field or by using the analytical solution [3], the ensemble average of Eq. (2.34) can be calculated,

$$\begin{aligned}
\langle \Delta E_{\omega_0} \rangle &= \frac{\pi}{8} \frac{(qE_0 \Delta t)^2}{m} \exp\left[ -2 \left( \frac{w_p - \omega_0}{2/\Delta t} \right)^2 \right], \\
\langle \Delta E_{2\omega_0} \rangle &= \frac{\pi}{16} \frac{(qE_0 \Delta t)^2}{m} \left( \frac{\hbar \omega_p}{mc^2} \right) \left( \frac{\omega_p}{\omega_0} \right) \sin^2(\theta_p) \times \exp\left[ -2 \left( \frac{w_p - 2\omega_0}{2/\Delta t} \right)^2 \right], \\
\langle \Delta E_{3\omega_0} \rangle &= \frac{3\pi}{16^2} \frac{(qE_0 \Delta t)^2}{m} \left[ \left( \frac{\hbar \omega_p}{mc^2} \right) \left( \frac{\omega_p}{\omega_0} \right) \sin^2(\theta_p) \right]^2 \exp\left[ -2 \left( \frac{w_p - 3\omega_0}{2/\Delta t} \right)^2 \right],
\end{aligned} \tag{2.35}$$

where $E_0 = -A_p \omega_p \cos(\theta_p)$. With the parameters used in our simulation, namely the natural frequency $\omega_0 = 10^{16}$rad/s, particle charge $q = 1.60 \times 10^{-19}$C, particle mass[1] $m = 9.11 \times 10^{-35}$kg, polarization angle $\theta_p = \pi/4$, pulse duration $\Delta t = 10^{-14}$s, and field amplitude $A_p = 1.5 \times 10^{-9}$Vs/m, the perturbation result shown in Eq. (2.35) gives the peak heights at $1\omega_0$, $2\omega_0$, and $3\omega_0$ as

$$\begin{aligned}
\langle \Delta E_{\omega_0} \rangle &\simeq 1.2\hbar\omega_0, \\
\langle \Delta E_{2\omega_0} \rangle &\simeq 0.6\hbar\omega_0, \\
\langle \Delta E_{3\omega_0} \rangle &\simeq 0.3\hbar\omega_0.
\end{aligned} \tag{2.36}$$

[1] The mass value is chosen to keep the integration time manageable without losing the physical characteristics of the problem.

The full spectrum can also be evaluated using Eq. (2.35), and the agreement with the simulation result (Figure 2.2) is about 80%. Therefore, the above perturbation analysis confirms that the occurrence of integer-spaced overtones is due to the parametric resonance through the spatial nonlinearity of the pulse field. Before the arrival of the pulse, the vacuum field prepares the particle ensemble with a particular distribution in the phase space. Such a distribution eventually determines the relative height for the excitation peaks.

## 2.5 Conclusions and Discussion

The occurrence of overtones is common in nonlinear classical systems. Whereas a classical anharmonic oscillator usually possesses non-integer spaced overtones [12, 13, 14], a classical harmonic oscillator can have integer-spaced overtones if the spatial nonlinearity of the excitation pulse is taken into account and the initial energy of the oscillator is nonzero. Such a process is analogous to excitation beyond the dipole approximation in quantum mechanics [15], as also illustrated by the need of a multipole expansion in our quantum mechanical calculation. When a classical harmonic oscillator is immersed in the vacuum field, a special steady state distribution of the initial condition is reached. The initial conditions provided by the vacuum field makes the excitation peak-height agree with those predicted by quantum mechanics (Figure 2.2). Remarkably, the agreement holds for weakly populated low excited states where the quantum-classical correspondence is thought to fail.

In conclusion, we have shown that the classical harmonic oscillator in the vacuum field exhibits the same integer-spaced excitation spectrum as its quantum counterpart. In this study, the classical and the quantum excitation spectra are compared in terms of ensemble averages. According to the quantum postulates, the individual outcomes

of energy measurement should be discrete, while the classical theory in our study gives a continuous distribution of energy outcomes. Thus, expanding on Milonni's comment; although SED can account for discrete energy levels in terms of an averaged energies, it can not, in terms of individual measurement outcomes. Nevertheless, the detailed agreement between the classical theory (as modified by the vacuum field) and quantum mechanics is surprising, as classical particle theories are generally thought to be unable to produce quantized excitation spectra. Extension of numerical work to atomic and molecular system appears to be interesting.

# Bibliography

[1] P. W. Milonni, *The Quantum Vacuum: An Introduction to Quantum Electrodynamics*, (Academic Press, Boston, 1994), p.293.

[2] T. H. Boyer, *Random electrodynamics: The theory of classical electrodynamics with classical electromagnetic zero-point radiation*, Phys. Rev. D **11**, 790 (1975).

[3] T. H. Boyer, *General connection between random electrodynamics and quantum electrodynamics for free electromagnetic fields and for dipole oscillator systems*, Phys. Rev. D **11**, 809 (1975).

[4] P. W. Milonni, *The Quantum Vacuum: An Introduction to Quantum Electrodynamics*, (Academic Press, Boston, 1994), pp. 116-119.

[5] P. W. Milonni, *The Quantum Vacuum: An Introduction to Quantum Electrodynamics*, (Academic Press, Boston, 1994), pp. 51-54, pp. 123-128, pp. 487-488.

[6] D. J. Griffiths, *Introduction to Electrodynamics*, 3rd ed. (Prentice-Hall, Upper Saddle River, 1999), p. 467.

[7] L. D. Landau and E. M. Lifshitz, *The Classical Theory of Fields*, 4th ed. (Pergamon Press, New York, 1987), p. 207, Eq. (75.10).

[8] J. D. Jackson, *Classical Electrodynamics*, 3rd ed. (Wiley, New York, 1998), p. 749, Eq. (16.10).

[9] S. T. Thornton and J. B. Marion, *Classical Dynamics of Particles and Systems*, 5th ed. (Brooks/Cole, Belmont, 2004), pp. 117-128.

[10] L. D. Landau and E. M. Lifshitz, *Mechanics*, 3rd ed. (Butterworth-Heinemann, Oxford, 1976), p. 80.

[11] A. Yariv, *Quantum Electronics*, 3rd ed. (Wiley, New York, 1988), p. 407.

[12] W. Heisenberg, *Über quantentheoretische Umdeutung kinematischer und mechanischer Besiehungen*, Z. Phys. **33**, 879 (1925).

[13] I. J. R. Aitchison, D. A. MacManus, T. M. Snyder, *Understanding Heisenbergs magical paper of July 1925: A new look at the calculational details*, A. J. P. **72**, 11 (2004).

[14] V. Averbukh and N. Moiseyev, Phys. Rev. A **57**, 1345 (1998).

[15] D. J. Griffiths, *Introduction to Quantum Mechanics*, 2nd ed. (Pearson Prentice Hall, Upper Saddle River, 2005), p. 366.

# Chapter 3

# Electron Deflection by Light-Induced Surface Near-Field

An electron beam is deflected when it passes over a silicon nitride surface, if the surface is illuminated by a low-power continuous-wave diode laser. A deflection angle of up-to 1.2 mrad is achieved for an electron beam of 29 $\mu$rad divergence. A mechanical beam-stop is used to demonstrate that the effect can act as an optical electron switch with a rise and fall time of 6 $\mu$s. Such a switch provides an alternative means to control electron beams, which may be useful in electron lithography and microscopy.

## 3.1 Introduction

The motion of electron beams is controlled in technologies such as electron lithography, microscopy, and diffractometry, in which the use of electric and magnetic fields to focus and steer beams are proven techniques. The control of electron motion with laser fields is also possible with the ponderomotive potential [1, 2]. In principle, such a technique offers the interesting possibility that no electrical components or other hardware needs to be placed in the vicinity of the electron beam. In addition, using the spatial control at optical wavelength scales, electron-optical elements can be realized [3, 4]. However, this optical control requires light intensities of $10^{14}\,\mathrm{W/m^2}$. In this paper we report on an optical electron switch that makes use of a small surface and a low power laser. Although some material is placed in the vicinity of the electron beam, no electrical feedthroughs are needed. Moreover, the required laser intensity is reduced by ten orders of magnitude as compared to techniques based on the direct interaction between laser light and electrons.

In this letter, it is shown that an electron beam that passes by a surface deflects when the surface is illuminated by a low-power continuous-wave diode laser. While searching for a nano-scale related effect at grazing incidence, a significant and unexpected beam deflection was observed. Deflection angles reached value of up-to 1.2 mrad. At a distance of 20 cm downstream from the interaction region, this translates to a beam displacement of 240 $\mu$m. A beam-stop can placed in the deflected electron beam, so that chopping the laser light results in complete switching the electron beam on and off. A maximum switching rate of $10^5$ Hz is established. Such an optically controlled electron switch may find applications in electron lithography [5], coherent beam splitting or provide an alternative route to STM-based techniques that probe optically induced near-fields [7, 6].

## 3.2 Experiment Results

A schematic of the experimental setup is shown in Figure 3.1. In our experiment, the electron beam is emitted from a thermionic source with a beam energy of 3.98 keV. After passing through two collimation slits of width 5 $\mu$m and 2 $\mu$m and separation 24 cm, the beam divergence is reduced to 29 $\mu$rad. At 6 cm after the second collimation slit, a surface is placed parallel to the beam path. Three different surfaces were tested. The first is a metallic-coated surface with nano-scale grooves [8, 9]. The other two are a flat amorphous aluminum (with aluminum oxide on surface) and a silicon nitride surface. All three surfaces resulted in electron beam deflection.

Continuous-wave diode lasers with maximum powers of 1 mW, 40 mW, and 5 mW and wavelengths of 532 nm, 685 nm, or 800 nm, respectively, were focused by a cylindrical lens onto the first surface. The other two surfaces were tested with 800 nm light.

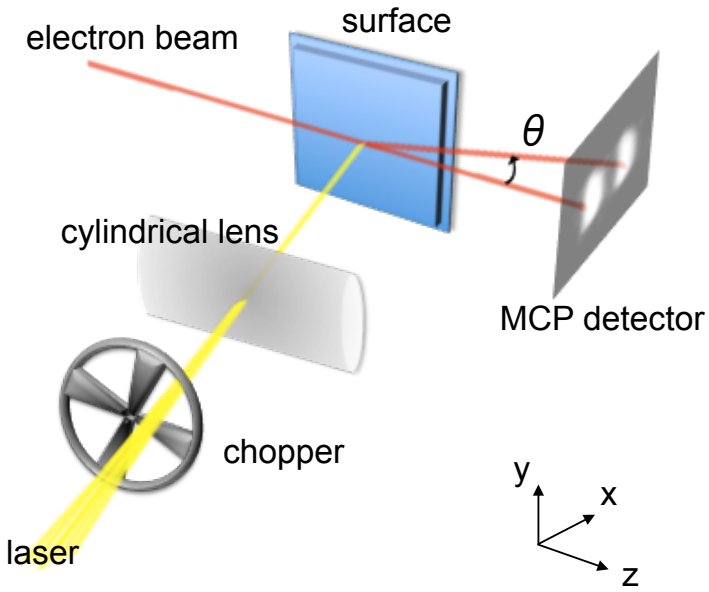


Figure 3.1: Setup of the low-power optical electron switch. An electron beam passing close to a surface is deflected by an angle $\theta$ when the surface is illuminated with a laser beam. The illumination is turned on and off with a mechanical chopper. (For a detailed descriptions see text.)

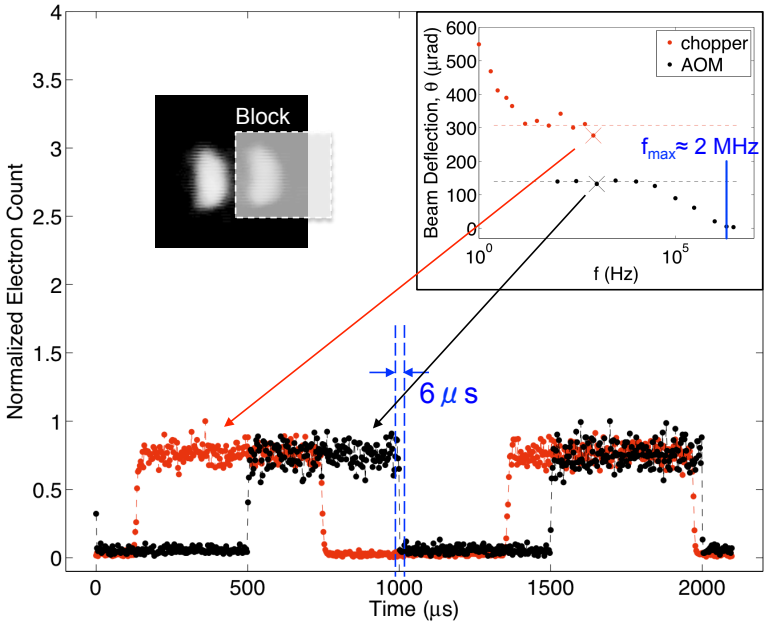


Figure 3.2: Electron counts as a function of time as the laser is switching on and off. Both chopper data (red dots) at 818 Hz and AOM data (black dots) at 1000 Hz are shown. Top-left inset: A time-averaged image shows the initial and deflected electron beam. A semi-transparent rectangle is added to depict a movable electron beam-stop. Top-right inset: The deflection magnitude $\theta$ is plotted as a function of the chopping frequency $f$. The estimated maximum chopping frequency according our heuristic model, $f_{max} \simeq 2\,\mathrm{MHz}$, is also drawn (blue line) for comparison. The red dots are data collected with a mechanical chopper and the black dots with a AOM.

The height of the laser beam and electron beam were matched by using an edge of the surface structure to block part of these beams. The focal distance is 25 cm, and the focused laser beam waist was about $280\,\mu\mathrm{m} \times 1\,\mathrm{mm}$ (FWHM). The waist of the light beam was determined by scanning the intensity profile in situ with a surface edge. A $10\,\mu$m wide electron beam passes at a distance of nominally $20\,\mu$m from the vertically mounted metallic surface. Micrometer stages were used to control the horizontal angle (in the $xz$-plane) as well as the vertical and horizontal travel of the surface. Downstream from the metallic surface, the electron beam passes through a parallel plate electrical deflector that aligns the beam with an electrostatic quadrupole lens.

This lens magnifies the electron beam image in the horizontal direction by a factor of 65. A chevron multi-channel plate (MCP) detector is placed 26 cm downstream from the surface. A phosphorescent screen follows the multichannel plates and a camera is used to record the beam profile. Amplifiers and discriminators are used in conjunction with a data acquisition board to record the electron counts as a function of time. Gaussian fits of the beam profiles are used to find the center positions and the deflection angles.

The vacuum pressure is about $1.5 \times 10^{-7}$ Torr. By chopping the laser, the electron beam image on the MCP detector switches between two positions. The time-averaged image displays two nearly identical electron beam images that are horizontally displaced from each other (Figure 3.2, top-left inset). An electron beam-stop, depicted in the top-left inset of Figure 3.2 as a semi-transparent rectangle, is added. The electron counts are recorded as a function of time (Figure 3.2). The dynamical response of the effect and also the finite electron beam size will limit the rise and fall time. To explore the limit of the response speed, an 40 MHz acousto-optical modulator (AOM) was used [IntraAction Corp. AOM-40N]. The amplitude of the acoustic wave was modulated from 1 Hz to 3 MHz. The inset of Figure 3.2 shows the scaling of the deflection magnitude of the electron beam with the AOM and the chopping frequency. Overall, the deflection magnitude stays constant for frequencies from $10^2$ Hz to $3 \times 10^5$ Hz. When the chopping frequencies are below $10^2$ Hz, the deflection magnitude becomes larger. When the AOM frequency increases above $2 \times 10^5$ Hz, the deflection magnitude decreases to zero.

In Figure 3.3, deflection larger than the beam divergence is observed to a distance of up-to 200 $\mu$m. The Rayleigh length of the focused laser beam is roughly 5 cm for an initial beam width of 1 mm and a the focal length of 25 cm). This is much larger than 200 $\mu$m, thus the illumination of the surface is unchanged as the surface is moved

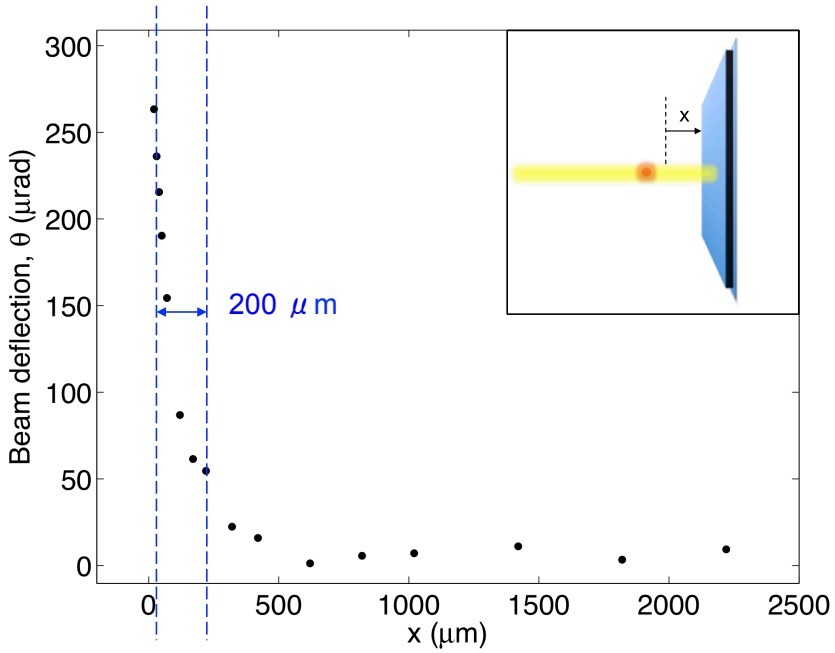


Figure 3.3: Distance dependence of the optical electron switch. As the surface is displaced, the distance $x$ between the surface and the electron beam is increased (inset). The optical electron switch turns completely on and off up-to a distance of $200\,\mu$m.

with respect to the electron beam. This measurement indicates that the deflection originates from the electron-surface interaction rather than the direct electron-laser interaction. As the interaction range is of the order of $200\,\mu$m, the interacting part of the surface is expected to have a length scale of that order of magnitude.

When moving the cylindrical lens in the vertical direction, the laser light crosses the electron beam at different heights. The deflection angle shown in Figure 3.4 changes its sign as the light crosses through the electron beam. This was determined by placing the beam-stop in such a way that the electron beam is half-blocked when the laser is off. If the laser light deflects the beam towards the beam-stop, the electron count rate decreases when the light is on. If the laser light deflect the beam away from the beam-stop, the electron count rate increases when the light is on. The magnitude of the deflection is determined by fitting a double Gaussian to the camera

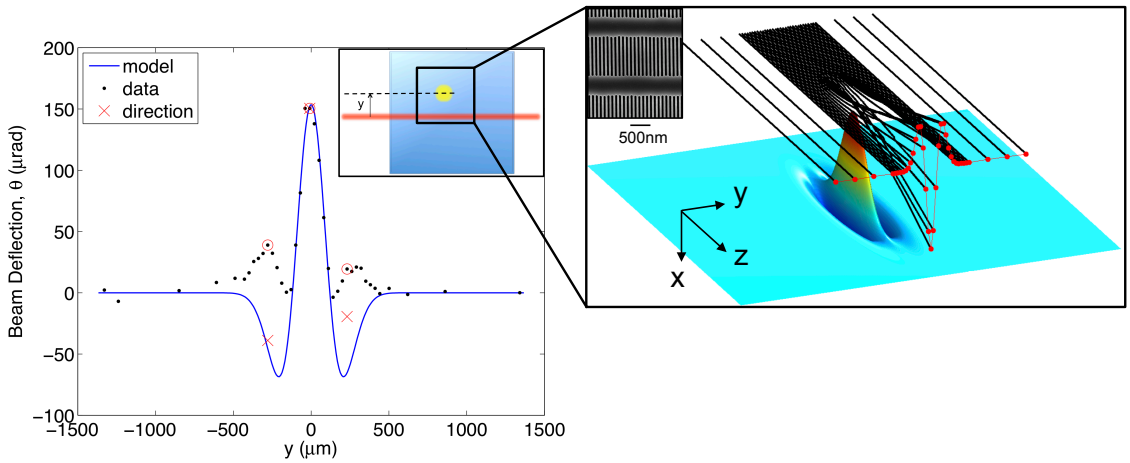


Figure 3.4: Beam deflection. Left: The measured deflection magnitude is given as a function of $y$ (black dots). A measurement of the deflection direction is made at three locations (red circles). The values including sign are indicated (red crosses). Reversals of deflection sign may be explained by our heuristic model (blue line) of light-induced surface charge redistribution. Right: A schematics of electron trajectories (black lines) and surface charge density (color-coded) is shown (See text for model description). Red represents positive charge density. Dark blue represents negative charge density. The red dots indicate the final positions of the electron beams. The interaction between the electron beams and the surface charges is attractive in the middle and repulsive at the sides.

image taken with the beam-stop removed. We observed that as the cylindrical lens is moved vertically and the light approaches the electron beam from one end, the electron beam first is deflected away from the surface, then attracted towards the surface, and back to deflected away again. No significant dependence is observed for surface tilt angles or laser polarizations.

Measurements have also been performed on different material surfaces such as uncoated flat silicon-nitride membrane and bulk aluminum. A repulsive deflection of up-to 1.2 mrad is observed with the silicon-nitride membrane, while at the aluminum surface some small attractive deflection is observed. Given that the deflection effect works with different laser wavelengths at low power, and it can occur at different material surface, we conclude that an optical electron switch based on such a effect

is robust.

## 3.3 Modeling

In the cases of uncoated silicon-nitride surface, the deflection shows only one sign unlike that observed with the nano-structured metallic-coated surface. This suggests that the deflection mechanism could be complex and involve a host of phenomena including laser heating, plasmon or phonon excitation, and surface-charge redistribution. Nevertheless, a simplistic model is constructed to illuminate some features of our experimental data shown in Figure 3.4. Focused by the cylindrical lens, the laser intensity profile on the metallic-coated surface can be approximated with an elliptical Gaussian,

$$I(y,z) = I_0 \times exp\left[-\left(\frac{y}{\Delta y}\right)^2 - \left(\frac{z}{\Delta z}\right)^2\right]. \tag{3.1}$$

where $\Delta y = 170\,\mu$m and $\Delta z = 0.6\,$mm (corresponding to FWHM of $280\,\mu\text{m} \times 1\,\text{mm}$). The maximum intensity is $I_0 = P_0/(\pi \Delta y \Delta z) = 1.6 \times 10^4\,\text{W/m}^2$ and the laser wavelength is $\lambda = 800\,$nm. The intensity gradient of the laser light can exert a pondermotive force[1] on the electrons in a thin surface layer,

$$\mathbf{F}_p = -\frac{e^2\lambda^2}{8\pi^2 m_e c^3 \epsilon_0}\nabla I. \tag{3.2}$$

If we assume a linear restoring force for the electron,

$$\mathbf{F}_r = -\alpha \mathbf{d}, \tag{3.3}$$

[1] When a light wave propagates in the solid, the phase relationship between the electric field and the magnetic field is a complex function of the material properties. For a simplistic model, here we assume that the electric field and the magnetic field are in phase.

where $\alpha$ is a fitting parameter and $\mathbf{d}$ is the displacement, the induced volume dipole moment can be determined,

$$\mathbf{P} = -n_0 e\mathbf{d} = \frac{1}{\alpha}\frac{n_0 e^3 \lambda^2}{8\pi^2 m_e c^3 \epsilon_0}\nabla I, \tag{3.4}$$

where $n_0 = 5.9 \times 10^{28}\,\mathrm{m}^{-3}$ is the free electron density of gold [10]. The volume charge distribution $\rho_{\mathrm{net}}$ is calculated according to $\rho_{\mathrm{net}} = -\nabla \cdot \mathbf{P}$. Assuming that the pondermotive force is effective through a depth of $\delta_{\mathrm{eff}} = 1\,\mathrm{nm}$ into the metal, the effective surface charge distribution on the metallic-coated surface can be obtained,

$$\sigma_{\mathrm{eff}} = \rho_{\mathrm{net}}\delta_{\mathrm{eff}} = -\frac{1}{\alpha}\frac{n_0 e^3 \lambda^2 \delta_{\mathrm{eff}}}{8\pi^2 m_e c^3 \epsilon_0}\nabla^2 I \tag{3.5}$$

The distance between the free electron beam and the surface is $20\,\mu\mathrm{m}$, which is much smaller than the length scale of the surface charge distribution. Thus, close to the surface the free electron beam may experience a electric field approximated by $\mathbf{E} \simeq \sigma_{\mathrm{eff}}/2\epsilon_0(-\hat{\mathbf{x}})$. Assuming that the velocity is constant in the $z$-direction because of the high kinetic energy $K_0 = 3.98\,\mathrm{keV}$ in the incoming $z$-direction, the deflection angle of the electron beam along the $x$-axis is estimated by

$$\theta = \frac{\Delta v_x}{v_0} = \frac{e}{4\epsilon_0 K_0}\int_{-\infty}^{+\infty}\sigma_{\mathrm{eff}}\,dz. \tag{3.6}$$

After integration, the above equation becomes

$$\theta = \theta_0\left[1 - 2\left(\frac{y}{\Delta y}\right)^2\right]e^{-(y/\Delta y)^2}, \tag{3.7}$$

where

$$\begin{aligned} \theta_0 &\equiv \frac{\sqrt{\pi} e E_0 \Delta z}{K_0}, \\ E_0 &\equiv \frac{\sigma_0}{2\epsilon_0}, \\ \sigma_0 &\equiv \frac{1}{\alpha} \frac{n_0 e^3 \lambda^2 \delta_{\text{eff}} I_0}{8\pi^3 \epsilon_0 m_e c^3 \Delta y^2}. \end{aligned} \tag{3.8}$$

The result of this simplistic model is compared with the experimental data in Figure 3.4. The fitting parameter is determined to be $\alpha \simeq 1.52 \times 10^{-16}\,\text{N/m}$. The linear restoring force (Eq. (3.3)) produces a harmonic motion with fundamental frequency $\omega_0 = \sqrt{\alpha/m_e}$. As a damped harmonic oscillator, the frequency response of the electron switch as shown in the inset of Figure 3.2 is limited to $f_{max} = \omega_0/2\pi \simeq 2\,\text{MHz}$.

Despite some qualitative agreements, this crude model does not explain many details, such as the physical origin of linear restoring force (Eq. (3.3)), the increase of the deflection magnitude at very low frequency (Figure 3.2), the asymmetric side-peak heights (Figure 3.4), and the fact that sign reversal of deflection direction is only present on the nano-structured metallic-coated surface but not on the silicon nitride surface. This heuristic model serves to draw attention to these features of our experimental data.

## 3.4 Summary and Discussions

In summary, when a material surface is placed near an electron beam, a deflection of the electron beam occurs as the surface is illuminated by a low-power laser. Thus, the combination of a material surface, a low-power laser, and a chopping device can make a low-power optical electron switch. Such an optical electron switch may be used for electron beam control in electron lithography and in electron microscopy.

The qualitative agreement between our model and the experimental data may be fortuitous, but it suggests that the deflection mechanism is consistent with a surface-charge redistribution that is driven by a mechanism that depends on the intensity gradient of the laser light.

An implication of this work is that instead of using one laser beam for the optical electron switch, one can use multiple laser beams to form spatial-temporal controlled structures on a material surface. The near field of the surface charge may mimic the pattern of the light, and electron matter waves could be coherently controlled in this manner analogous to the Kapitza-Dirac effect or temporal lensing [11, 12], but without the need for high laser intensity. Finally, we speculate that the combination of laser pulses and nano-fabricated structures will make femtosecond manipulation of free electrons accessible at low intensities [7, 13, 14].

# Bibliography

[1] H. A. H. Boot and R. B. R. .S. Harvie, *Charged particles in a non-uniform radio-frequency field*, Nature **180**, 1187 (1957).

[2] G. Sciaini and R. J. Dwayne Miller, *Femtosecond electron diffraction: heralding the era of atomically resolved dynamics*, Rep. Prog. Phys. **74**, 096101 (2011)

[3] D. Freimund, K. Aflatooni, H. Batelaan, *Observation of the Kapitza-Dirac effect*, Nature **413**, 142 (2001).

[4] P. H. Bucksbaum, D. W. Schumacher, and M. Bashkansky, *High intensity Kapitza-Dirac effect*, Phys. Rev. Lett. **61**, 1182 (1988).

[5] MAPPER Lithography, *http://www.mapperlithography.com/*

[6] C. Ropers, D. R. Solli, C. P. Schulz, C. Lienau, and T. Elsaesser, *Localized Multiphoton Emission of Femtosecond Electron Pulses from Metal Nanotips*, Phys. Rev. Lett. **98**, 043907 (2007).

[7] M. Becker, W. Huang, H. Batelaan, E. J. Smythe, and F. Capasso, *Measurement of the ultrafast emporal response of a plasmonic antenna*, Ann. Phys. (Berlin) **525**, A21 (2013).

[8] T. A. Savas, S. N. Shah, M. L. Schattenburg, J. M. Carter, and H. I. Smith, *Achromatic interferometric lithography for 100?nm?period gratings and grids*, J. Vac. Sci. Technol. B **13**, 2732 (1995).

[9] T. A. Savas, M. L. Schattenburg, J. M. Carter, and H. I. Smith, *Large?area achromatic interferometric lithography for 100 nm period gratings and grids*, J. Vac. Sci. Technol. B **14**, 4167 (1996).

[10] N. W. Ashcroft and N. D. Mermin, *Solid State Physics*, (Holt, Rinehart, and Winston, New York), p.5.

[11] H. Batelaan, *Colloquium: Illuminating the Kapitza-Dirac effect with electron matter optics*, Rev. Mod. Phys. **79**, 929 (2007).

[12] P. Baum and A. H. Zewail, *Attosecond electron pulses for 4D diffraction and microscopy*, Proc. Natl. Acad. Sci. **104**, 18409 (2007).

[13] V. A. Lobastov, R. Srinivasan, and A. H. Zewail, *Four-dimensional ultrafast electron microscopy*, Proc. Natl. Acad. Sci. **102**, 7069 (2005).

[14] O. Muskens, *Towards nanoantenna electron switches*, Ann. Phys. (Berlin) **525**, A21 (2013).

# Chapter 4

# Ultrafast Temporal Response of a Plasmonic Structure

The temporal response of a plasmonic antenna at the femtosecond time scale is measured via cross-correlation technique. The antenna consists of a square array of nanometer-size gold rods. We find that the far-field dispersion of light reflected from the plasmonic antenna is less than that of a $1.2mm$ thick glass slide. Assuming a simple oscillating dipole model, this implies that the near-field of the antenna may be used as an electron switch that responds faster than $20fs$.

## 4.1 Introduction

Light incident on a metallic material is strongly attenuated at the surface. For metallic films of nanometer-scale thickness, all electrons in the material can interact with light at optical frequencies. When this thin metallic film is patterned with nanometer scale boundaries to form a metallic nanoparticle, electron resonance behavior occurs. This phenomenon takes place when the dominant spatial mode of the charge oscillation, i.e. the dipole oscillation mode, corresponds to the boundary shape of the particle [1]. Consequently, metallic nanoparticles that are made of the same material but have different shapes reflect different colors under white light illumination [2, 3].

As the size of metallic particles shrinks down to sub-wavelength dimensions, a strong near-field arises at the poles of the oscillating dipole. The magnitude of this near field exceeds ten times that of the incident field which drives the particle, a phenomena known as near-field enhancement [4, 5]. The near-field enhancement can be even greater if several metallic particles are positioned close to each other [4]. Additionally, the resonant response of a particle assembly can be tuned through variation of the inter-particle distances [6, 7]. Thus, an array of metallic nanoparticles can be used as an antenna, known as a plasmonic antenna [6]. The periodic structure and strong near-field enhancement of a plasmonic antenna during a laser pulse may enable it to act as a pulsed electron diffraction grating. Such a device could be used as an ultrafast electron switch [8] or as a target for ultrafast electron microscopy [9]. In order to utilize a plasmonic antenna as an electron diffraction/deflection device in the ultrafast regime, it is important to know how a plasmonic antenna responds to ultrafast light. In this study, we investigate the temporal response of a plasmonic antenna upon excitation by a femtosecond light pulse.

The temporal response of regular arrays of nanoparticles have been previously

studied with methods sensitive to a variety of nanoparticle shapes [10, 11, 12, 13]. The results from autocorrelation measurements of transmitted second- and third-harmonic generation signals indicated a fast relaxation time of $6fs$. The arrays used had periodicities and gapsizes of hundreds of nanometers. In this study, we use a reflective cross-correlation method, which does not require higher-harmonic generation. We also propose that this arrangement could be used for electron manipulation. Periodic structures with a period of about 100 nm and gaps of tens of nanometers are of particular interest for electron diffraction. The former provides practical diffraction angles, while the latter yields an intensity enhancement that may be suited for femtosecond electron switching. In view of our proposed application, the main objective of the present work is to establish that the enhanced near-fields in the small gaps between elements of the array studied do not significantly lengthen the temporal response of the reflected pulse.

The near-field of nanoscale structures has been probed time-independently with tip-enhanced electron emission microscopy [14] and time-dependently with photon-induced near-field microscopy [15]. As pointed out previously in [15], these techniques may also be used to investigate plasmonic antennas. The simple all-optical technique presented in this study may be useful for selecting plasmonic antennas with an interesting response in the far-field that warrant a more involved study with pulsed electron techniques.

## 4.2 Model and Theory

When excited by a light pulse, the plasmonic antenna generates a strong localized near-field. The far-field is radiated as a reflected pulse. For an array of dipole radiators, the relation between the antenna's near- and far-fields can be deduced by

inspecting the fields of each single oscillating dipole, $p(t) = p_\omega e^{-i(\omega t+\phi_\omega)}$ [16],

$$\begin{aligned}\mathbf{E}_{dip,\omega}(\mathbf{r},t) &= \frac{1}{4\pi\epsilon_0}\left\{\frac{k^2}{r}(\hat{\mathbf{r}}\times\hat{\mathbf{z}})\times\hat{\mathbf{r}}\right. \\ &\quad \left.+\left(\frac{1}{r^3}-\frac{ik}{r^2}\right)[3(\hat{\mathbf{r}}\cdot\hat{\mathbf{z}})\hat{\mathbf{r}}-\hat{\mathbf{z}}]\right\} p_\omega e^{-i(\omega t+\phi_\omega)}e^{ikr} \\ &= E_{far}(\mathbf{r})p_\omega\omega^2 e^{i\phi_\omega}e^{-i\omega(t-r/c)} \\ &\quad + E_{mid}(\mathbf{r})p_\omega\omega e^{i\pi/2}e^{i\phi_\omega}e^{-i\omega(t-r/c)} \\ &\quad + E_{near}(\mathbf{r})p_\omega e^{i\phi_\omega}e^{-i\omega(t-r/c)},\end{aligned} \tag{4.1}$$

where $k = \omega/c$, $\omega$ is the frequency of the incident field, $p_\omega$ is the dipole strength of the nanoparticle, $\phi_\omega$ is the relative phase between the incident field and the induced dipole, $\hat{\mathbf{z}}$ is the unit vector along the direction of the dipole, and $\hat{\mathbf{r}}$ is the unit vector in the radial direction from the center of the dipole. $E_{far}(\mathbf{r})$, $E_{mid}(\mathbf{r})$, and $E_{near}(\mathbf{r})$ are the spatial patterns of the far-, intermediate-, and near-fields, respectively. It is clear from Eq. (4.1) that the near- and far-fields have the same phase spectrum. Although the power spectra of the near- and far-fields differ by a factor of $\omega^2$, this difference is negligible for a plasmonic resonance curve that is about $100nm$ wide and centered at $800nm$. Thus, the near- and far-fields of a nanoparticle can have an identical temporal pulse shape. The field reflected from the plasmonic antenna is the sum of the fields from many dipole radiators. When the plasmonic antenna is excited by a pulse incident at an angle, the far-fields from all the radiators have the same time delay in the direction specified by the law of reflection. In other directions, the far-fields interfere destructively. Thus, the far-field of the plasmonic antenna has the same temporal shape as the far-field of the individual radiators. The near-field close to the surface of the antenna has contributions from the incident field and the nearest radiators of the antenna. The field in the immediate vicinity of one particular

radiator has also a contribution from a neighboring radiator. However that field has a time delay that depends on the distance between the next neighbor pairs. For an array of nanoparticles in an antenna, these distances can be in the subwavelength region. Then the contribution of a next neighbor radiator is delayed in time at most by their distance divided by the speed of light, and therefore, within the sub-cycle oscillation. This contribution would be in phase and not reduce the local field. The near-fields from more distant neighbors can have a significant time delay and may potentially cause the temporal duration of the near-field to broaden. However, the strength of the near-field of any radiator decays quickly over the distance of one wavelength, so the contribution from the far neighbors can be ignored. Consequently, the near-field of the plasmonic antenna has the same temporal shape as the near-field of the individual radiator. Assuming that the antenna is an array of independent dipole radiators, the temporal response of the antenna's far-field equals the temporal response of the antenna's near-field.

Information about the temporal width of the antenna's far-field may be obtained from comparing the cross-correlation signal of the reflected pulse to the auto-correlation signal of the incident pulse. Comparison between the cross-correlation signal and the auto-correlation signal shows the contrast between the reflected pulse and the incident pulse, revealing any broadening that may have occurred. However, without knowing the specific shape of the pulse, its temporal width cannot be inferred directly from the cross-correlation signal. In this study, the cross-correlation signal is modeled by reconstructing the pulse fields from the experimentally obtained power spectrum and the theoretically computed phase spectrum. The phase spectrum of the reflected pulse is modeled by calculating the phase dispersion of a pulse which

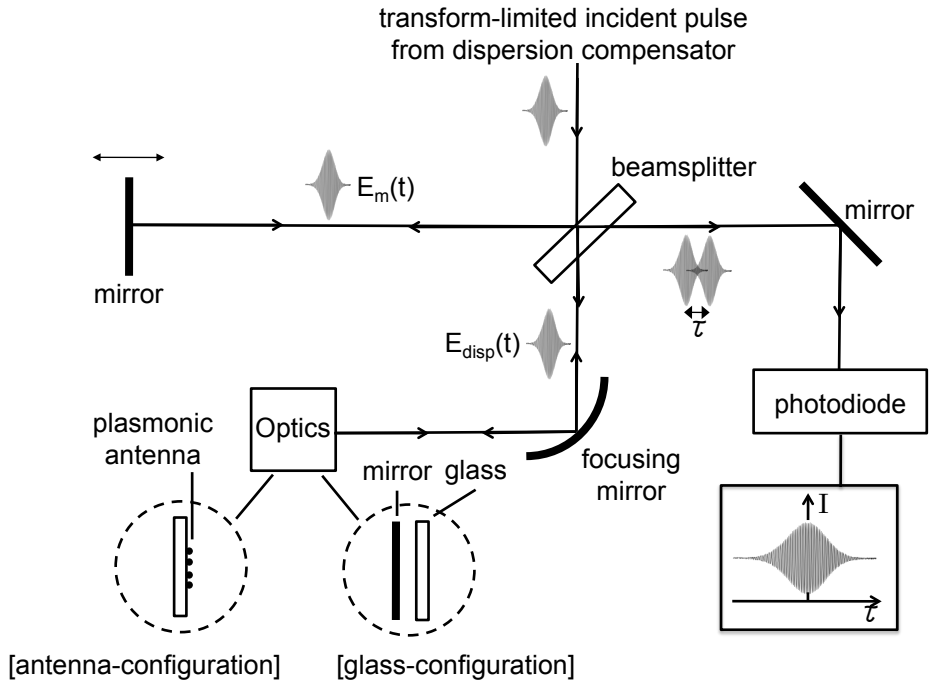


Figure 4.1: Experimental setups. Experiments are performed for the antenna-configuration and the glass-configuration configuration. The experiment with the glass-configuration tests the validity of the glass-model, while the experiment of the antenna-configuration measures the temporal width of the plasmonic antenna's far field.

passes through a glass slide (fused silica) twice,

$$\phi_{disp}(\omega) = \frac{2\omega d}{c} n(\omega) + \phi_{bs}(\omega), \tag{4.2}$$

where $d$ is the thickness of the glass slide, $\omega$ is the frequency, $\phi_{bs}(\omega)$ is the phase dispersion due to the beamsplitter (BK7), and $n(\omega)$ is the index of refraction of the glass (fused silica). The "modeling" is here intended to provide a convenient parametrization of the pulsed laser field, not to model the physical process of reflection in the plasmonic antenna. The thickness of the glass, $d$, is the only fitting parameter in this "glass-model" and is determined by comparing theoretical and experimental cross-correlation signals.

## 4.3 Experiment

To test the validity of this glass-model, experiments were performed in the antenna-configuration and the glass-configuration, shown in Figure 4.1. After the pulse passed through a dispersion compensator [17], a beamsplitter splits the pulse to two arms. In the antenna-configuration, the pulse reflected from the plasmonic antenna arm is interfered with the pulse reflected from the mirror arm. The temporal interference pattern is the cross-correlation signal,

$$C(\tau) = \int_{-\infty}^{+\infty} E_m(t-\tau)E_{disp}(t)\,d\tau, \tag{4.3}$$

where $E_m(t)$ is the pulse from the mirror arm, and $E_{disp}(t)$ is the pulse from the antenna arm of the interferometer. Note that the real part of the field is used in this expression. If the plasmonic antenna changes either the power or phase spectrum of the incident pulse, the pulse from the antenna arm, $E_{disp}(t)$, would have a different shape than the pulse from the mirror arm, $E_m(t)$. This would result in a cross-correlation signal between $E_m(t)$ and $E_{pl}(t)$ that is broader than the auto-correlation signal of $E_m(t)$,

$$A(\tau) = \int_{-\infty}^{+\infty} E_m(t-\tau)E_m(t)\,d\tau. \tag{4.4}$$

The same applies to the glass-configuration except that glass causes a known changes in the phase spectrum while leaving the power spectrum unaltered.

In our experiment, we use a light pulse which has a full-width-half-maximum spectral bandwidth of $\Delta\lambda = 63nm$ and a central frequency of $\lambda_c = 800nm$. Assuming a transform-limited pulse shape, the full-width-half-maximum temporal width of the pulse field is $\Delta t \simeq 20fs$. The plasmonic antenna used in the experiment was fabricated using electron-beam lithography as described in [6]. Images ob-

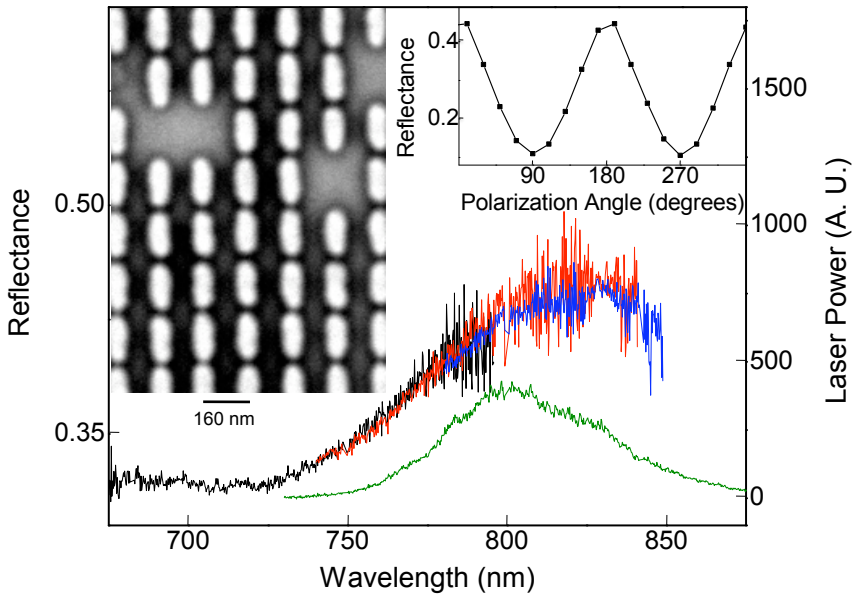


Figure 4.2: Antenna characterization. Left top: An SEM micrograph of a localized area of the array of gold nanorods that make up the plasmonic antenna. Missing nanorods can be observed. Main graph: The power spectrum of the input laser pulse (green line) is centered around $800nm$ and supports a minimum pulse duration of $20fs$. The reflectance of incident unpolarized white light from the plasmonic antenna (black, red, and blue lines) shows a broad resonance structure. Right top: The reflectance of linearly polarized light at a wavelength of $800nm$ shows a maximal reflection when the incident polarization is aligned along the length nanorods.

tained with a scanning-electron microscope (see Figure 4.2) indicate rod dimensions of $170nm \times 80nm$. The rod array has a period of $160nm$ in the direction perpendicular to the rod length and a spacing of $10 - 20nm$ along their length. The entire array has a size of $100\mu m \times 100\mu m$. Defects, such as missing rods and scratches, were present and are likely a result of the fabrication process and/or damage incurred during handling the device. The broadband reflectance spectrum was measured by focusing white light from a xenon lamp with a $50\times$ microscope objective onto the plasmonic antenna (Figure 4.2). Reflected light was collected into a fiber-coupled spectrometer and the resulting spectrum was normalized with the spectrum reflected

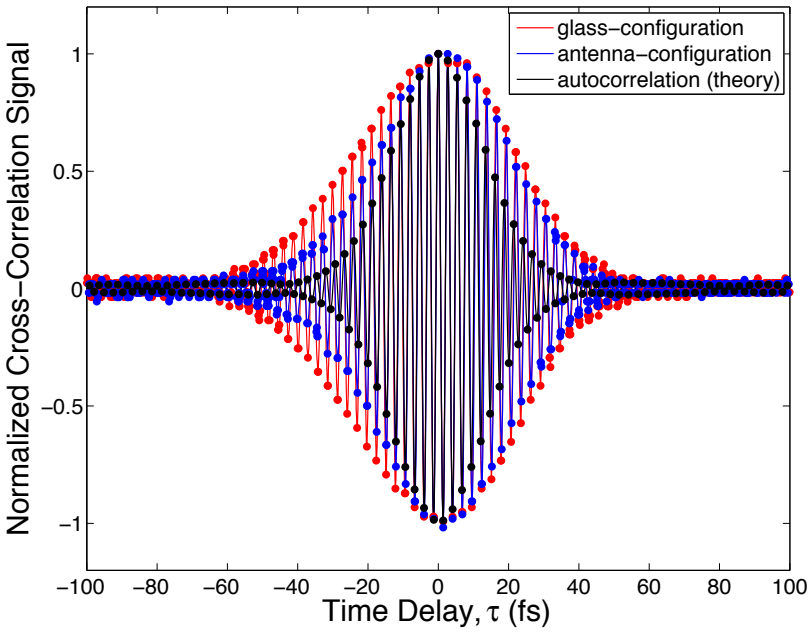


Figure 4.3: Experimental data of the cross-correlation signals from the antenna-configuration (blue line) and the glass-configuration (red line). The auto-correlation signal of the incident pulse (black line) is computed from the measured power spectrum according to the Wiener-Khinchin theorem.

by a silver mirror. The result is consistent with the relations between resonance and rod dimensions and spacing reported in [6]. Comparison of the input laser spectrum with the plasmonic antenna reflectance spectrum shows that the laser pulse contained frequencies appropriate for generating near-field enhancement in the antenna. The reflection of the array was also measured using a focused beam of linearly polarized light with a wavelength of $800nm$ (Figure 4.2). The polarization-dependence of the reflected power is indicative of the resonance behavior of the antenna.

## 4.4 Results

The experimental results are shown in Figure 4.3. The autocorrelation signal is obtained by taking a Fourier transform of the measured power spectrum according

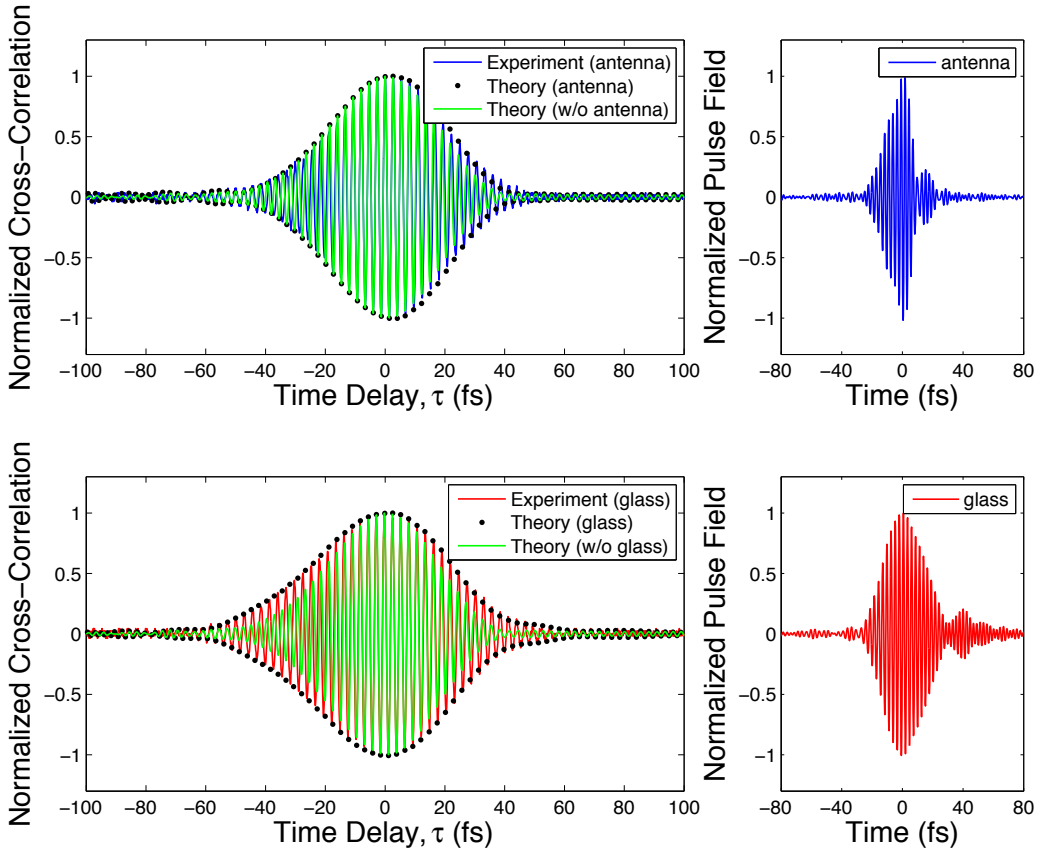


Figure 4.4: Field reconstruction from the glass-model. Left: The theoretically calculated cross-correlation signal shown in black dots, is fit to the experimental data (blue and red lines) to determine the glass thickness in the glass-model (see text). For comparison the theoretical cross-correlation signal for zero glass thickness is shown (green line). Right: Reflected pulses are reconstructed with the fit parameter obtained from the glass-model in the absence of dispersion from other optical components in the system. The pulse reflected from the array is shown in blue, and the pulse from the glass in red.

to the Wiener-Khinchin theorem. The width of the autocorrelation signal is about $30fs$. The cross-correlation widths measured in the antenna- and glass-configuration are about $40fs$ and $50fs$, respectively. To interpret this result, the glass-model is used. Agreement between the model and the experimental data is found when the fitting parameter is set at $1.145mm$, as shown in Figure 4.4. This is indeed close to the measured thickness of the glass slide used in the experiment, which is $1.14mm$.

When this model is applied to the cross-correlation spectrum acquired in the antenna-configuration, the effect of reflection from the antenna can be modeled well by the glass-model when the fitting parameter is set to $0.25mm$. Use of this model enables the reconstruction of the reflected pulse by the nanorod array without inclusion of dispersion from other optical components in the system. The temporal width of the pulse reflected by the antenna (shown in Figure 4.4) is found to be close to that of the incident pulse.

## 4.5 Discussion: Plasmonic Femtosecond Electron Swtich

Our result indicates that it may be feasible to use the plasmonic antenna as a femtosecond electron switch. Consider an electron pulse that is cross fired with a laser pulse in such a way that the electron pulse and the laser pulse meet at the plasmonic antenna (Figure 4.5). Upon excitation by the laser pulse, the antenna will provide a spatially modulated near-field defined by the periodicity of the antenna array. An antenna can enhance the laser intensity at its near field by a factor of $\kappa \simeq 800$ [4], although for the antenna array characterized above an enhancement factor of about 50 is expected [6]. As an electron comes close to the antenna surface, it will experience a force from the antenna's near-field. For an electron wave with a small coherence length the interaction time will be shorter than the laser period ($2.7fs$) and the electron will interact with the enhanced electric field of the array. If the electron wave is more delocalized, the electron will experience the cycle-averaged ponderomotive potential of the array [18, 19]. The maximum diffraction angle by the ponderomotive

potential $\Delta\theta_m$ may be estimated by [20]

$$\Delta\theta_m = \frac{\Delta v}{v} = \frac{\tau}{mv}\frac{\Delta U_p}{\Delta x} = \frac{\tau}{mv}\frac{e^2(\kappa I)}{2m\epsilon_0 c\omega^2 \Delta x}, \tag{4.5}$$

where $\tau$ is the interaction time, $v$ is the electron's speed, $m$ is the electron's mass, $\omega$ is the laser frequency, $I$ is the laser intensity, $U_p$ is the pondermotive potential of the near-field, and $\Delta x$ is the distance over which the pondermotive potential drops to a small value. For a non-amplified femtosecond laser oscillator operated at $800nm$, the laser pulse has an energy of $10nJ$ and thus an intensity of $I = 2 \times 10^{11}(W/cm^2)$ for a duration of $50fs$ and a focus of $10\mu m$. This intensity approaches the damage threshold of most materials, including a plasmonic antenna. However, cooling the antenna, optimizing the enhancement, or simply working at somewhat lower intensity may be possible. Assuming that the typical interaction length scale between the potential and the electron wave is about $100nm$, the interaction time can be estimated to be $\tau = 10(fs)$ for a $500eV$ electron pulse. Given an enhancement factor of $\kappa \simeq 800$, a significant diffraction angle of $\Delta\theta_m = 10(mrad)$ can be expected. For a more moderate intensity enhancement of $\kappa = 40$, the ponderomotive diffraction is reduced to a measurable $\Delta\theta_m = 0.5(mrad)$. This is considered to be a lower limit for the expected electron diffraction angle.

If the electron wave interaction is limited to the enhanced field within the $10nm$ gap between the nanoparticles, the interaction time will be $1fs$ and classical deflection by the antenna's electric field could be considered. In this case the deflection angle is given by

$$\Delta\theta_E = \frac{\Delta v}{v} = \frac{eE\tau}{mv}, \tag{4.6}$$

where the electric field $E = \sqrt{\kappa\epsilon_0 cI}$. For a moderate enhancement of $\kappa \simeq 50$ the result is a large deflection of $\Delta\theta_E = 50(mrad)$. These rough estimates indicate that

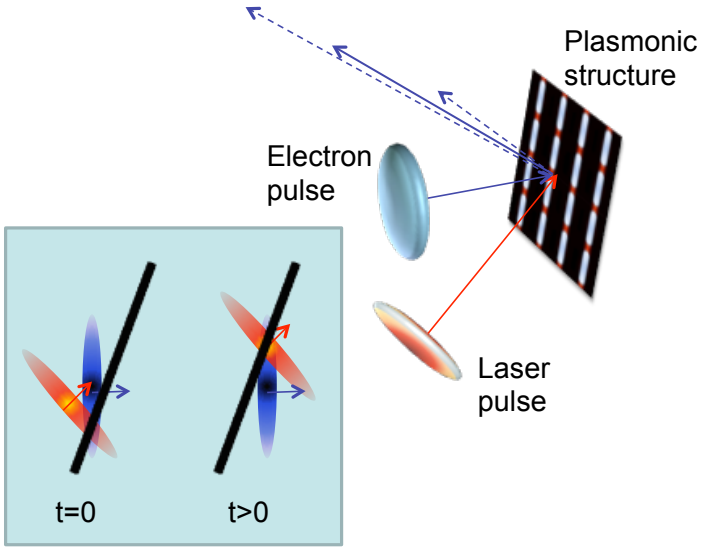


Figure 4.5: Proposed femtosecond electron switch. A laser pulse affects the scattering of an electron pulse through the pondermotive potential provided by the enhanced near field of a plasmonic antenna. The intersection of a laser pulse and electron pulse can be directed onto a planar structure. Following an idea of Zewail [21], the electron velocity and interaction angle can be chosen in such a way that the pulses remain synchronous as they sweep over the planar plasmonic structure. The consequence is that the temporal resolution of the switched electron beams (dashed blue lines) is set by the laser pulse duration.

it appears reasonable to consider a plasmonic antenna for the purpose of ultrafast electron switching.

In summary, three properties of a plasmonic antenna justify its proposed use as an ultrafast electron switch. First, the periodic structure of the plasmonic antenna ensures a large gradient of the electric field and thus a large force on the electron. Second, the near-field enhancement eliminates the need for strong laser power, enabling the use of a laser with a higher repetition rate and increasing the number of electrons per second detected. Third, the planar geometry allows for femtosecond resolution detection and control of large diameter electron beams by the use of angle tuning [21].

## 4.6 Conclusions

In conclusion, agreement between theory and experimental cross-correlation data in the glass-configuration justifies use of the glass-model to model the phase spectrum of the laser pulse reflected from the plasmonic antenna. According to this model, the temporal width of the antenna's far field is shown to be close to that of the excitation pulse. Under the assumption that the plasmonic antenna is described by a collection of dipole radiators, the near field of the plasmonic antenna responds on the femtosecond scale. This ultrafast enhanced near field may affect the motion of incident electron beams. Femtosecond nanoscale pulsed electron sources have been developed [22, 23]. Electron pulse compression techniques applied to electron beams extracted from pulsed sources have been shown to deliver electron pulses of about $100fs$ [24]. Electron pulse compression techniques have been proposed to deliver sub-femtosecond electron pulses [25, 8, 26]. A plasmonic antenna functioning as an electron switch may be an ideal detection method for these sub-femtosecond electron pulses.

# Bibliography

[1] J. Aizpurua, G. W. Bryant, L. J. Richter, and F. J. Garcia de Abajo, *Optical properties of coupled metallic nanorods for field-enhanced spectroscopy*, Phys. Rev. B. **71**, 235420 (2005).

[2] W. A. Murray and W. L. Barnes, *Plasmonic Materials*, Adv. Mater. **19**, 3771 (2007).

[3] M. I. Stockman, *Nanoplasmonics: The physics behind the applications*, Phys. Today **64**, 39 (2011).

[4] E. Cubukcu, N. Yu, E. J. Smythe, L. Diehl, K. B. Crozier, and F. Capasso, *Plasmonic Laser Antennas and Related Devices*, IEEE J. Sel. Top. Quant. Electron **14**, 1448 (2008).

[5] E. L. Kelly, E. Coronado, L. L. .Zhao, and G. C. Schatz, *The Optical Properties of Metal Nanoparticles: The Influence of Size, Shape, and Dielectric Environment*, J. Phys. Chem. B **107**, 688 (2003).

[6] E. J. Smythe, E. Cubukcu, and F. Capasso, *Optical properties of surface plasmon resonances of coupled metallic nanorods*, Opt. Express **15**, 7439 (2007).

[7] W. Rechberger, A. Hohenau, A. Leitner, J. R. Krenn, B. Lamprecht, and F. R. Aussenegg, *Optical properties of two interacting gold nanoparticles*, Opt. Commun. **220**, 137 (2003).

[8] S. A. Hilbert, C. Uiterwaal, B. Barwick, H. Batelaan, and A. H. Zewail, *Temporal lenses for attosecond and femtosecond electron pulses*, Proc. Natl. Acad. Sci. USA **106**, 10558 (2009).

[9] A. H. Zewail, *4D Ultrafast electron diffraction, crystallography, and microscopy*, Annu. Rev. Phys. Chem. **57**, 65 (2006).

[10] B. Lamprecht, A. Leitner, and F. R. Aussenegg, *Femtosecond decay-time measurement of electron-plasma oscillation in nanolithographically designed silver particles*, Appl. Phys. B **64**, 269 (1997).

[11] B. Lamprecht, A. Leitner, and F. R. Aussenegg, *SHG studies of plasmon dephasing in nanoparticles*, Appl. Phys. B **68**, 419 (1999).

[12] B. Lamprecht, J. R. Krenn, A. Leitner, and F. R. Aussenegg, *Resonant and Off-Resonant Light-Driven Plasmons in Metal Nanoparticles Studied by Femtosecond-Resolution Third-Harmonic Generation*, Phys. Rev. Lett. **83**, 4421 (1999).

[13] B. Lamprecht, J. R. Krenn, A. Leitner, and F. R. Aussenegg, *Particle-plasmon decay-time determination by measuring the optical near-fields autocorrelation: influence of inhomogeneous line broadening*, Appl. Phys. B **69**, 223 (1999).

[14] C. Ropers, D. R. Solli, C. P. Schulz, C. Lienau, and T. Elsaesser, *Localized Multiphoton Emission of Femtosecond Electron Pulses from Metal Nanotips*, Phys. Rev. Lett. **98**, 043907 (2007).

[15] B. Barwick, D. J. Flannigan, and A. H. Zewail, *Photon-induced near-field electron microscopy*, Nature **462**, 902 (2009).

[16] J. D. Jackson, *Classical Electrodynamics*, 3rd ed. (Wiley, New York, 1998), p. 411, Eq. (9.18).

[17] S. Akturk, X. Gu, M. Kimmel, and R. Trebino, *Extremely simple single-prism ultrashort-pulse compressor*, Opt. Express **14**, 10101 (2006).

[18] P. H. Bucksbaum, D. W. Schumacher, and M. Bashkansky, *High intensity Kapitza-Dirac effect*, Phys. Rev. Lett. **61**, 1182 (1988).

[19] D. L. Freimund, K. Aflatooni, and H. Batelaan, *Observation of the Kapitza-Dirac effect*, Nature **413**, 142 (2001).

[20] H. Batelaan, *Colloquium: Illuminating the Kapitza-Dirac effect with electron matter optics*, Rev. Mod. Phys. **79**, 929 (2007).

[21] J. C. Williamson, and A. H. Zewail, *Ultrafast Electron Diffraction. Velocity Mismatch and Temporal Resolution in Cross-Beam Experiments*, Chem. Phys. Lett. **209**, 10 (1993).

[22] P. Hommelhoff, C. Kealhofer, and M. A. Kasevich, *Ultrafast Electron Pulses from a Tungsten Tip Triggered by Low-Power Femtosecond Laser Pulses*, Phys. Rev. Lett. **97**, 247402 (2006).

[23] S. A. Hilbert, A. Neukirch, C. Uiterwaal, and H. Batelaan, *Exploring temporal and rate limits of laser-induced electron emission*, J. Phys. B **42**, 141001 (2009).

[24] T. van Oudheusden, P. L. E. M. Pasmans, S. B. van der Geer, M. J. de Loos, M. J. van der Wiel, and O. J. Luiten, *Compression of Subrelativistic Space-*

*Charge-Dominated Electron Bunches for Single-Shot Femtosecond Electron Diffraction*, Phys. Rev. Lett. **105**, 26 (2010).

[25] P. Baum and A. H. Zewail, *Breaking resolution limits in ultrafast electron diffraction and microscopy*, Proc. Natl. Acad. Sci. USA **103**, 16105 (2006).

[26] L. Veisz, G. Kurkin, K. Chernov, V. Tarnetsky, A. Apolonski, F. Krausz, and E. Fill, *Hybrid dcac electron gun for fs-electron pulse generation*, New J. Phys. **9**, 451 (2007).

# Appendix A

# The Vacuum Field in Unbounded and Bounded Space

In "unbounded" space, the modes are continuous and the field is expressed in terms of an integral. In "bounded" space, the modes are discrete and the field is expressed in terms of a summation. In both cases, the expression for the field amplitude needs to be obtained (see Appendix A.1 and A.2). The integral expression helps comparison with analytical calculations in previous papers [2, 6, 7, 8, 3], while the summation expression is what we use in our numerical work.

## A.1 Unbounded Space

The homogeneous solution of Maxwell's equations in unbounded space is equivalent to the solution for a wave equation,

$$\begin{aligned}\mathbf{E}(\mathbf{r},t) =& \frac{1}{2}\sum_{\lambda=1}^{2}\int d^3k\ \boldsymbol{\varepsilon}(\mathbf{k},\lambda)\left(\tilde{A}(\mathbf{k},\lambda)e^{i(\mathbf{k}\cdot\mathbf{r}-\omega t)}+\tilde{A}^*(\mathbf{k},\lambda)e^{-i(\mathbf{k}\cdot\mathbf{r}-\omega t)}\right)\\ \mathbf{B}(\mathbf{r},t) =& \frac{1}{2c}\sum_{\lambda=1}^{2}\int d^3k\ (\hat{\mathbf{k}}\times\boldsymbol{\varepsilon}(\mathbf{k},\lambda))\left(\tilde{A}(\mathbf{k},\lambda)e^{i(\mathbf{k}\cdot\mathbf{r}-\omega t)}+\tilde{A}^*(\mathbf{k},\lambda)e^{-i(\mathbf{k}\cdot\mathbf{r}-\omega t)}\right),\end{aligned} \tag{A.1}$$

where $\tilde{A}(\mathbf{k},\lambda)$ is the undetermined field amplitude for the mode $(\mathbf{k},\lambda)$ and has the unit of electric field (V/m), $\hat{\mathbf{k}}$ is defined as the unit vector of $\mathbf{k}$, and the two vectors, $\boldsymbol{\varepsilon}(\mathbf{k},1)$ and $\boldsymbol{\varepsilon}(\mathbf{k},2)$, describe an orthonormal polarization basis in a plane that is perpendicular to the wave vector $\mathbf{k}$.

Without loss of generality, a random phase $e^{i\tilde{\theta}(\mathbf{k},\lambda)}$ can be factored out from the field amplitude $\tilde{A}(\mathbf{k},\lambda)=A(\mathbf{k},\lambda)e^{i\tilde{\theta}(\mathbf{k},\lambda)}$,

$$\begin{aligned}\mathbf{E}(\mathbf{r},t) =& \frac{1}{2}\sum_{\lambda=1}^{2}\int d^3k\ \boldsymbol{\varepsilon}(\mathbf{k},\lambda)\left(A(\mathbf{k},\lambda)e^{i(\mathbf{k}\cdot\mathbf{r}-\omega t)}e^{i\tilde{\theta}(\mathbf{k},\lambda)}+A^*(\mathbf{k},\lambda)e^{-i(\mathbf{k}\cdot\mathbf{r}-\omega t)}e^{-i\tilde{\theta}(\mathbf{k},\lambda)}\right)\\ \mathbf{B}(\mathbf{r},t) =& \frac{1}{2c}\sum_{\lambda=1}^{2}\int d^3k\ \boldsymbol{\xi}(\mathbf{k},\lambda)\left(A(\mathbf{k},\lambda)e^{i(\mathbf{k}\cdot\mathbf{r}-\omega t)}e^{i\tilde{\theta}(\mathbf{k},\lambda)}+A^*(\mathbf{k},\lambda)e^{-i(\mathbf{k}\cdot\mathbf{r}-\omega t)}e^{-i\tilde{\theta}(\mathbf{k},\lambda)}\right).\end{aligned} \tag{A.2}$$

where $\boldsymbol{\xi}(\mathbf{k},\lambda)\equiv\hat{\mathbf{k}}\times\boldsymbol{\varepsilon}(\mathbf{k},\lambda)$. The field amplitude $A(\mathbf{k},\lambda)$ can be determined through the phase averaged energy density,

$$\langle u\rangle_{\tilde{\theta}}=\frac{\epsilon_0}{2}\big\langle|\mathbf{E}|^2\big\rangle_{\tilde{\theta}}+\frac{1}{2\mu_0}\big\langle|\mathbf{B}|^2\big\rangle_{\tilde{\theta}}, \tag{A.3}$$

where $\epsilon_0$ is the vacuum permittivity, $\mu_0$ is the vacuum permeability, and $\tilde{\theta}$ is the

random phase in Eq. (A.2). To evaluate the phase averaged energy density $\langle u \rangle_{\tilde{\theta}}$, we first calculate $|\mathbf{E}|^2$ and $|\mathbf{B}|^2$ using Eq. (A.2),

$$\begin{aligned} |\mathbf{E}|^2(\mathbf{r},t) &= \mathbf{E}(\mathbf{r},t)\mathbf{E}^*(\mathbf{r},t) = \frac{1}{4}\sum_{\lambda,\lambda'}\int d^3k \int d^3k' \; (\boldsymbol{\varepsilon}(\mathbf{k},\lambda)\cdot\boldsymbol{\varepsilon}(\mathbf{k}',\lambda'))f, \\ |\mathbf{B}|^2(\mathbf{r},t) &= \mathbf{B}(\mathbf{r},t)\mathbf{B}^*(\mathbf{r},t) = \frac{1}{4c^2}\sum_{\lambda,\lambda'}\int d^3k \int d^3k' \; (\boldsymbol{\xi}(\mathbf{k},\lambda)\cdot\boldsymbol{\xi}(\mathbf{k}',\lambda'))f, \end{aligned} \tag{A.4}$$

where $f \equiv f(\mathbf{k},\lambda;\mathbf{k}',\lambda';\mathbf{r},t)$,

$$\begin{aligned} f(\mathbf{k},\lambda;\mathbf{k}',\lambda';\mathbf{r},t) = {} & A(\mathbf{k},\lambda)A^*(\mathbf{k}',\lambda')e^{i(\mathbf{k}\cdot\mathbf{r}-\omega t+\tilde{\theta}(\mathbf{k},\lambda))}e^{-i(\mathbf{k}'\cdot\mathbf{r}-\omega' t+\tilde{\theta}(\mathbf{k}',\lambda'))} \\ & + A(\mathbf{k},\lambda)A(\mathbf{k}',\lambda')e^{i(\mathbf{k}\cdot\mathbf{r}-\omega t+\tilde{\theta}(\mathbf{k},\lambda))}e^{i(\mathbf{k}'\cdot\mathbf{r}-\omega' t+\tilde{\theta}(\mathbf{k}',\lambda'))} \\ & + A^*(\mathbf{k},\lambda)A^*(\mathbf{k}',\lambda')e^{-i(\mathbf{k}\cdot\mathbf{r}-\omega t+\tilde{\theta}(\mathbf{k},\lambda))}e^{-i(\mathbf{k}'\cdot\mathbf{r}-\omega' t+\tilde{\theta}(\mathbf{k}',\lambda'))} \\ & + A^*(\mathbf{k},\lambda)A(\mathbf{k}',\lambda')e^{-i(\mathbf{k}\cdot\mathbf{r}-\omega t+\tilde{\theta}(\mathbf{k},\lambda))}e^{i(\mathbf{k}'\cdot\mathbf{r}-\omega' t+\tilde{\theta}(\mathbf{k}',\lambda'))}. \end{aligned} \tag{A.5}$$

The random phase average can be calculated with the following relation [3],

$$\begin{aligned} \left\langle e^{\pm i(\tilde{\theta}(\mathbf{k},\lambda)+\tilde{\theta}(\mathbf{k}',\lambda'))}\right\rangle_{\tilde{\theta}} &= 0, \\ \left\langle e^{\pm i(\tilde{\theta}(\mathbf{k},\lambda)-\tilde{\theta}(\mathbf{k}',\lambda'))}\right\rangle_{\tilde{\theta}} &= \delta_{\lambda',\lambda}\delta^3(\mathbf{k}'-\mathbf{k}). \end{aligned} \tag{A.6}$$

Applying Eq. (A.6) to Eq. (A.5), we obtain

$$\begin{aligned} \langle f(\mathbf{k},\lambda;\mathbf{k}',\lambda';\mathbf{r},t)\rangle_{\tilde{\theta}} = {} & A(\mathbf{k},\lambda)A^*(\mathbf{k}',\lambda')e^{i(\mathbf{k}\cdot\mathbf{r}-\omega t)}e^{-i(\mathbf{k}'\cdot\mathbf{r}-\omega' t)}\delta_{\lambda',\lambda}\delta^3(\mathbf{k}'-\mathbf{k}) \\ & + A^*(\mathbf{k},\lambda)A(\mathbf{k}',\lambda')e^{-i(\mathbf{k}\cdot\mathbf{r}-\omega t)}e^{i(\mathbf{k}'\cdot\mathbf{r}-\omega' t)}\delta_{\lambda',\lambda}\delta^3(\mathbf{k}'-\mathbf{k}). \end{aligned} \tag{A.7}$$

Consequently, $\left\langle |\mathbf{E}|^2 \right\rangle_{\tilde{\theta}}$ and $\left\langle |\mathbf{B}|^2 \right\rangle_{\tilde{\theta}}$ can be evaluated using Eqs. (A.4) and (A.7),

$$\begin{aligned}
\left\langle |\mathbf{E}|^2 \right\rangle_{\tilde{\theta}} &= \frac{1}{4} \sum_{\lambda,\lambda'} \int d^3k \int d^3k' \ (\boldsymbol{\varepsilon}(\mathbf{k},\lambda) \cdot \boldsymbol{\varepsilon}(\mathbf{k}',\lambda')) \langle f \rangle_{\tilde{\theta}} = \frac{1}{2} \sum_{\lambda=1}^{2} \int d^3k \ \left| A(\mathbf{k},\lambda) \right|^2 , \\
\left\langle |\mathbf{B}|^2 \right\rangle_{\tilde{\theta}} &= \frac{1}{4c^2} \sum_{\lambda,\lambda'} \int d^3k \int d^3k' \ (\boldsymbol{\xi}(\mathbf{k},\lambda) \cdot \boldsymbol{\xi}(\mathbf{k}',\lambda')) \langle f \rangle_{\tilde{\theta}} = \frac{1}{2c^2} \sum_{\lambda=1}^{2} \int d^3k \ \left| A(\mathbf{k},\lambda) \right|^2 .
\end{aligned} \tag{A.8}$$

The above calculation leads to a relation between the field amplitude $A(\mathbf{k},\lambda)$ and the phase averaged energy density $\langle u \rangle_{\tilde{\theta}}$ in unbounded space,

$$\langle u \rangle_{\tilde{\theta}} = \frac{\epsilon_0}{2} \sum_{\lambda=1}^{2} \int d^3k \ \left| A(\mathbf{k},\lambda) \right|^2 . \tag{A.9}$$

Now, if we postulate that the vacuum energy is $\hbar\omega/2$ for each mode $(\mathbf{k},\lambda)$, then in a bounded cubic space of volume $V$ the vacuum energy density is

$$u_{vac} = \frac{1}{V} \sum_{\mathbf{k},\lambda} \frac{\hbar\omega}{2} = \frac{1}{V} \sum_{\mathbf{k},\lambda} \frac{\hbar\omega}{2} \left( \frac{L_x}{2\pi} \Delta k_x \right) \left( \frac{L_y}{2\pi} \Delta k_y \right) \left( \frac{L_z}{2\pi} \Delta k_z \right) = \sum_{\lambda=1}^{2} \frac{1}{(2\pi)^3} \sum_{\mathbf{k}} \Delta^3 k \frac{\hbar\omega}{2}. \tag{A.10}$$

In the limit of unbounded space (i.e. $V \to \infty$), the volume element $\Delta^3 k$ becomes differential (i.e. $\Delta^3 k \to d^3 k$) and the vacuum energy density becomes

$$u_{vac} = \sum_{\lambda=1}^{2} \frac{1}{(2\pi)^3} \int d^3k \frac{\hbar\omega}{2}. \tag{A.11}$$

Comparing this result with Eq. (A.9), we find

$$|A_{vac}(\mathbf{k},\lambda)|^2 = \frac{\hbar\omega}{(2\pi)^3 \epsilon_0}. \tag{A.12}$$

Assuming $A_{vac}(\mathbf{k},\lambda)$ is a positive real number, the vacuum field amplitude in un-

bounded space is determined,

$$A_{vac}(\mathbf{k},\lambda) = \sqrt{\frac{\hbar\omega}{8\pi^3\epsilon_0}}. \tag{A.13}$$

Therefore, the vacuum field in unbounded space is found to be

$$\begin{aligned}
\mathbf{E}_{vac}(\mathbf{r},t) =& \frac{1}{2}\sum_{\lambda=1}^{2}\int d^3k\ \boldsymbol{\varepsilon}(\mathbf{k},\lambda)\sqrt{\frac{\hbar\omega}{8\pi^3\epsilon_0}}\left(e^{i(\mathbf{k}\cdot\mathbf{r}-\omega t)}e^{i\tilde{\theta}(\mathbf{k},\lambda)} + e^{-i(\mathbf{k}\cdot\mathbf{r}-\omega t)}e^{-i\tilde{\theta}(\mathbf{k},\lambda)}\right) \\
\mathbf{B}_{vac}(\mathbf{r},t) =& \frac{1}{2c}\sum_{\lambda=1}^{2}\int d^3k\ \boldsymbol{\xi}(\mathbf{k},\lambda)\sqrt{\frac{\hbar\omega}{8\pi^3\epsilon_0}}\left(e^{i(\mathbf{k}\cdot\mathbf{r}-\omega t)}e^{i\tilde{\theta}(\mathbf{k},\lambda)} + e^{-i(\mathbf{k}\cdot\mathbf{r}-\omega t)}e^{-i\tilde{\theta}(\mathbf{k},\lambda)}\right),
\end{aligned} \tag{A.14}$$

which is Eq. (1.1).

## A.2 Bounded Space

The solution of homogeneous Maxwell's equations in bounded space has the summation form,

$$\begin{aligned}
\mathbf{E}(\mathbf{r},t) &= \frac{1}{2}\sum_{\mathbf{k},\lambda}\left(\tilde{A}_{\mathbf{k}\lambda}e^{i(\mathbf{k}\cdot\mathbf{r}-\omega t)} + \tilde{A}^{*}_{\mathbf{k}\lambda}e^{-i(\mathbf{k}\cdot\mathbf{r}-\omega t)}\right)\boldsymbol{\varepsilon}_{\mathbf{k}\lambda}, \\
\mathbf{B}(\mathbf{r},t) &= \frac{1}{2c}\sum_{\mathbf{k},\lambda}\left(\tilde{A}_{\mathbf{k}\lambda}e^{i(\mathbf{k}\cdot\mathbf{r}-\omega t)} + \tilde{A}^{*}_{\mathbf{k}\lambda}e^{-i(\mathbf{k}\cdot\mathbf{r}-\omega t)}\right)\boldsymbol{\xi}_{\mathbf{k}\lambda},
\end{aligned} \tag{A.15}$$

where $\boldsymbol{\xi}_{\mathbf{k}\lambda} = \hat{\mathbf{k}} \times \boldsymbol{\varepsilon}_{\mathbf{k}\lambda}$, $\tilde{A}_{\mathbf{k}\lambda}$ is the undetermined field amplitude for the mode $(\mathbf{k},\lambda)$ and has the unit of electric field (V/m), $\hat{\mathbf{k}}$ is defined as the unit vector of $\mathbf{k}$, and the two vectors, $\boldsymbol{\varepsilon}_{\mathbf{k},1}$ and $\boldsymbol{\varepsilon}_{\mathbf{k},2}$, describe an orthonormal polarization basis in a plane that is perpendicular to the wave vector $\mathbf{k}$.

Using the relation[1]

$$\begin{aligned}\left\langle e^{\pm i(\tilde{\theta}_{\mathbf{k}\lambda}+\tilde{\theta}_{\mathbf{k}',\lambda'})}\right\rangle_{\tilde{\theta}} &= 0 \\ \left\langle e^{\pm i(\tilde{\theta}_{\mathbf{k}\lambda}-\tilde{\theta}_{\mathbf{k}',\lambda'})}\right\rangle_{\tilde{\theta}} &= \delta_{\lambda',\lambda}\delta_{\mathbf{k}',\mathbf{k}},\end{aligned} \tag{A.16}$$

we can follow the same argument in Appendix A.1 and obtain the phase averaged energy density in bounded space

$$\langle u\rangle_{\tilde{\theta}} = \frac{\epsilon_0}{2}\sum_{\mathbf{k},\lambda}\left|A_{\mathbf{k}\lambda}\right|^2, \tag{A.17}$$

where $\tilde{A}_{\mathbf{k}\lambda} = A_{\mathbf{k}\lambda}e^{i\tilde{\theta}_{\mathbf{k}\lambda}}$. Again, if we postulate that the vacuum energy is $\hbar\omega/2$ for each mode $(\mathbf{k},\lambda)$, then in a bounded space of volume $V$ the vacuum energy density is

$$u_{vac} = \frac{1}{V}\sum_{\mathbf{k},\lambda}\frac{\hbar\omega}{2}. \tag{A.18}$$

Comparing Eq. (A.17) and Eq. (A.18), the vacuum field amplitude in bounded space is determined,

$$A_{vac_{\mathbf{k}\lambda}} = \sqrt{\frac{\hbar\omega}{\epsilon_0 V}}. \tag{A.19}$$

Therefore, the RED vacuum field in bounded space is

$$\begin{aligned}\mathbf{E}_{vac}(\mathbf{r},t) &= \frac{1}{2}\sum_{\mathbf{k},\lambda}\left(\sqrt{\frac{\hbar\omega}{\epsilon_0 V}}e^{i(\mathbf{k}\cdot\mathbf{r}-\omega t)}e^{i\tilde{\theta}_{\mathbf{k}\lambda}} + c.c.\right)\boldsymbol{\varepsilon}_{\mathbf{k}\lambda}, \\ \mathbf{B}_{vac}(\mathbf{r},t) &= \frac{1}{2c}\sum_{\mathbf{k},\lambda}\left(\sqrt{\frac{\hbar\omega}{\epsilon_0 V}}e^{i(\mathbf{k}\cdot\mathbf{r}-\omega t)}e^{i\tilde{\theta}_{\mathbf{k}\lambda}} + c.c\right)\boldsymbol{\xi}_{\mathbf{k}\lambda}.\end{aligned} \tag{A.20}$$

[1] If the two modes are not identical (i.e. $\mathbf{k}' \neq \mathbf{k}$ or $\lambda' \neq \lambda$), then $e^{i\theta_{\mathbf{k},\lambda}}$ and $e^{i\theta_{\mathbf{k}',\lambda'}}$ are independent, which leads to the factorization $\langle e^{i(\theta_{\mathbf{k},\lambda}\pm\theta_{\mathbf{k}',\lambda'})}\rangle_{\tilde{\theta}} = \langle e^{i\theta_{\mathbf{k},\lambda}}\rangle_{\tilde{\theta}}\langle e^{\pm i\theta_{\mathbf{k}',\lambda'}}\rangle_{\tilde{\theta}} = 0$.

# Appendix B

# Isotropic Polarization Vectors

A wave vector chosen along the $z$-axis,

$$\tilde{\mathbf{k}} = \begin{pmatrix} \tilde{k}_x \\ \tilde{k}_y \\ \tilde{k}_z \end{pmatrix} = \begin{pmatrix} 0 \\ 0 \\ k \end{pmatrix}, \tag{B.1}$$

has an orthonormal polarization basis in the $xy$-plane,

$$\tilde{\boldsymbol{\varepsilon}}_{\mathbf{k},1} = \begin{pmatrix} \cos\chi \\ \sin\chi \\ 0 \end{pmatrix}, \tilde{\boldsymbol{\varepsilon}}_{\mathbf{k},2} = \begin{pmatrix} -\sin\chi \\ \cos\chi \\ 0 \end{pmatrix}, \tag{B.2}$$

where the random angle $\chi$ is uniformly distributed in $[0, 2\pi]$. To obtain the wave vector $\mathbf{k}$ in Eq. (1.34), $\tilde{\mathbf{k}}$ can be first rotated counterclockwise about the $y$-axis by an angle $\theta$, then counterclockwise about the $z$-axis by an angle $\phi$. The corresponding

rotation matrix is described by

$$\begin{aligned}\hat{R} &= \hat{R}_{\phi}^{(z)}\hat{R}_{\theta}^{(y)} \\ &= \begin{pmatrix}\cos\phi & -\sin\phi & 0\\ \sin\phi & \cos\phi & 0\\ 0 & 0 & 1\end{pmatrix}\begin{pmatrix}\cos\theta & 0 & \sin\theta\\ 0 & 1 & 0\\ -\sin\theta & 0 & \cos\theta\end{pmatrix} \\ &= \begin{pmatrix}\cos\theta\cos\phi & -\sin\phi & \cos\phi\sin\theta\\ \cos\theta\sin\phi & \cos\phi & \sin\phi\sin\theta\\ -\sin\theta & 0 & \cos\theta\end{pmatrix},\end{aligned} \tag{B.3}$$

and $\mathbf{k}$ is obtained accordingly,

$$\mathbf{k} = \hat{R}\tilde{\mathbf{k}} = \begin{pmatrix}k\sin\theta\cos\phi\\ k\sin\theta\sin\phi\\ k\cos\theta\end{pmatrix}. \tag{B.4}$$

In the same manner, we can rotate $\tilde{\boldsymbol{\varepsilon}}_{\mathbf{k},1}$ and $\tilde{\boldsymbol{\varepsilon}}_{\mathbf{k},2}$ with the rotation matrix $\hat{R}$, and obtain an isotropically distributed[1] polarization basis as described in Eq. (1.39),

$$\begin{aligned}\boldsymbol{\varepsilon}_{\mathbf{k},1} &= \hat{R}\tilde{\boldsymbol{\varepsilon}}_{\mathbf{k},1} = \begin{pmatrix}\cos\theta\cos\phi\cos\chi - \sin\phi\sin\chi\\ \cos\theta\sin\phi\cos\chi + \cos\phi\sin\chi\\ -\sin\theta\cos\chi\end{pmatrix} \\ \boldsymbol{\varepsilon}_{\mathbf{k},2} &= \hat{R}\tilde{\boldsymbol{\varepsilon}}_{\mathbf{k},2} = \begin{pmatrix}-\cos\theta\cos\phi\sin\chi - \sin\phi\cos\chi\\ -\cos\theta\sin\phi\sin\chi + \cos\phi\cos\chi\\ \sin\theta\sin\chi\end{pmatrix}.\end{aligned} \tag{B.5}$$

[1] After the rotation, the uniformly distributed circle will span into a uniformly distributed spherical surface.

# Appendix C

# Repetitive Time

A field composed of finite discrete frequencies,

$$E(t) = \sum_{k=1}^{N} E_k \cos(\omega_k t), \tag{C.1}$$

repeats itself at the least common multiple (LCM) of all the periods of its frequency components,

$$E(t + \tau_{rep}) = E(t), \tag{C.2}$$

$$\tau_{rep} = [T_1, T_2, \ldots, T_N]_{LCM}, \tag{C.3}$$

where $T_k = \dfrac{2\pi}{\omega_k}$. An example of a two-frequency beat wave is given in Figure C.1. Given the frequency spectrum of $E(t)$, one can draw a relation between the repetition time $\tau_{rep}$ and the greatest common divider (GCD) of the frequencies,

$$\tau_{rep} = \frac{2\pi}{(\omega_1, \omega_2, \ldots, \omega_N)_{GCD}}. \tag{C.4}$$

The derivation of the relation in Eq. (C.4) is the following. First, we factorize the sum of all the frequencies into two terms,

$$\omega_1+\omega_2+\ldots+\omega_N = \frac{2\pi}{T_1}+\frac{2\pi}{T_2}+\ldots+\frac{2\pi}{T_N} = \frac{2\pi}{[T_1,T_2,\ldots,T_N]_{LCM}}(n_1+n_2+\ldots+n_N), \quad \text{(C.5)}$$

where $n_k$ are positive integers,

$$n_k = \frac{[T_1,T_2,\ldots,T_N]_{LCM}}{T_k}. \quad \text{(C.6)}$$

Now, it is true that $(n_1,n_2,\ldots,n_N)_{GCD}=1$, otherwise it would lead to a contradiction to Eq. (C.6). Therefore, one can conclude that

$$\Delta\omega_{gcd} \equiv (\omega_1,\omega_2,\ldots,\omega_N)_{GCD} = \frac{2\pi}{[T_1,T_2,\ldots,T_N]_{LCM}}. \quad \text{(C.7)}$$

From Eq. (C.3) and Eq. (C.7), the relation in Eq. (C.4)

$$\tau_{rep} = \frac{2\pi}{\Delta\omega_{gcd}} \quad \text{(C.8)}$$

is drawn. Since the simulation should only be carried through an integration time $\tau_{int} \leq \tau_{rep}$ to avoid repetitive solutions, in our case the choice of the integration time (Eq. (1.62))

$$\tau_{int} = \frac{2\pi}{\Delta\omega}, \quad \text{(C.9)}$$

where $\Delta\omega$ is the smallest frequency gap ($\Delta\omega \leq \Delta\omega_{gcd}$), suffices our purpose. The frequency gap as a function of $\kappa$ can be estimated using Eq. (1.35),

$$\Delta\omega(\kappa) = \omega(\kappa) - \omega(\kappa-\Delta\kappa) = c(3\kappa)^{1/3} - c(3\kappa)^{1/3}\left(1-\frac{\Delta\kappa}{\kappa}\right)^{1/3}. \quad \text{(C.10)}$$

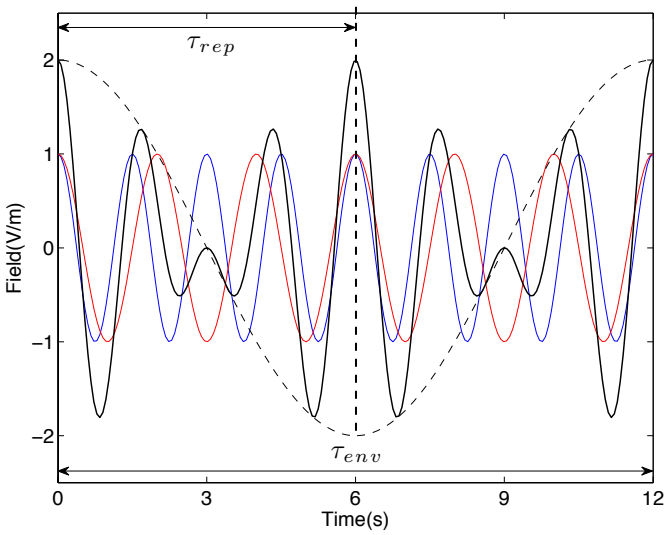


Figure C.1: Repetition time of a beat wave. A beat wave (black solid line) is made of two frequency components (red and blue solid line). The oscillation periods of the two frequency components are $T_1 = 1.5$ and $T_2 = 2$, thus the repetition time is $\tau_{rep} = [T_1, T_2]_{LCM} = 6$. Note that the periodicity of the envelope (black dash line) is $\tau_{env} = 12$, which is different from the repetition time $\tau_{rep} = 6$.

Applying the sharp resonance condition (Eq. (1.10)) to Eqs. (1.24) and (1.36), it can be further shown that $\Delta\kappa$ is much smaller than $\kappa_0$ and $\kappa \simeq \kappa_0$,

$$\frac{\Delta\kappa}{\kappa_0} = \left(\frac{3}{N_{\mathbf{k}} - 1}\right)\frac{\Delta}{\omega_0} \ll 1, \tag{C.11}$$

$$\kappa = \kappa_0 + O\left(\frac{\Delta}{\omega_0}\right), \tag{C.12}$$

where $\kappa_0 = \frac{1}{3}\left(\frac{\omega_0}{c}\right)^3$. Therefore, the size of $\Delta\omega(\kappa)$ is approximately fixed within the sampled frequency range $\Delta$, and the smallest frequency gap $\Delta\omega$ can be approximated as

$$\Delta\omega \simeq \frac{c(3\kappa_0)^{1/3}}{3}\frac{\Delta\kappa}{\kappa_0}. \tag{C.13}$$

# Appendix D

# Parallel Computing of the QM/SED Excitation Spectrum

The following is the Fortran 90 code used in the simulation of the quantized excitation spectrum as described in Chapter 2.

```
Module matrix_functions
    implicit none
    contains

    FUNCTION expM(order, A, N)
        implicit none
        integer, intent(in) :: order, N
        real*8, dimension(N,N), intent(in) :: A
        real*8, dimension(N,N) :: expM, idtyM
        real*8, dimension(order+1,N,N) :: OrdM
        integer i, j, k
        real*8 kd, factrl

        do i = 1, N                     !build identity matrix
            do j = 1, N
                idtyM(i,j) = kd(i*1d0,j*1d0)
            enddo
        enddo
        do k = 0, order                 !build matrix at different order
            if (k >= 1) then
                OrdM(k+1,:,:) = idtyM
                do i = 1, k
                    OrdM(k+1,:,:) = matmul(OrdM(k+1,:,:), A)
                enddo
            else
                OrdM(k+1,:,:) = idtyM
            endif
        enddo
        do k = 0,order                  !put on the factorial factor on each order of matrix
            OrdM(k+1,:,:) = OrdM(k+1,:,:)/factrl(k)
        enddo
        expM = sum(OrdM,1)
    RETURN
    END FUNCTION

    FUNCTION cexpM(order, A, N)
        implicit none
        integer, intent(in) :: order, N
        complex*16, dimension(N,N), intent(in) :: A
        real*8, dimension(N,N) :: idtyM
        complex*16, dimension(N,N) :: cexpM
        complex*16, dimension(order+1,N,N) :: OrdM
        integer i, j, k
        real*8 kd, factrl

        do i = 1, N                     !build identity matrix
            do j = 1, N
                idtyM(i,j) = kd(i*1d0,j*1d0)
            enddo
        enddo
        do k = 0, order                 !build matrix at different order
            if (k >= 1) then
                OrdM(k+1,:,:) = idtyM
                do i = 1, k
                    OrdM(k+1,:,:) = matmul(OrdM(k+1,:,:), A)
                enddo
            else
                OrdM(k+1,:,:) = idtyM
            endif
        enddo
        do k = 0,order                  !put on the factorial factor on each order of matrix
            OrdM(k+1,:,:) = OrdM(k+1,:,:)/factrl(k)
        enddo
        cexpM = sum(OrdM,1)
```

```
    RETURN
    END FUNCTION

    FUNCTION matmul3(dim, A, B, C)
        integer, intent(in) :: dim
        complex*16, dimension(dim, dim), intent(in) :: A
        real*8, dimension(dim, dim), intent(in) :: B, C
        complex*16, dimension(dim, dim) :: matmul3

        matmul3 = matmul( (matmul(A,B)), C )

    RETURN
    END FUNCTION


    FUNCTION matmulN(N, dim, A)
        integer, intent(in) :: N, dim
        real*8, dimension(N, dim, dim) :: A
        real*8, dimension(dim, dim) :: matmulN
        integer i

!       matmulN = matmul( matmul(A(1,:,:),A(2,:,:)), A(3,:,:) )

        matmulN = A(1,:,:)
        do i = 2,N
            matmulN = matmul( matmulN, A(i,:,:) )
        enddo
    RETURN
    END FUNCTION

End Module

Module vector_functions
    implicit none
    contains

    Function dot(A,B)
        implicit none
        real*8, intent(in), dimension(3) :: A,B
        real*8 dot
        dot = dot_product(A,B)
    Return
    End Function

    Function cross(A,B)
        implicit none
        real*8, intent(in), dimension(3) :: A,B
        real*8, dimension(3) :: cross

        cross(1) = A(2)*B(3)-A(3)*B(2)
        cross(2) = A(3)*B(1)-A(1)*B(3)
        cross(3) = A(1)*B(2)-A(2)*B(1)
    Return
    End Function

    Function norm(A)
        implicit none
        real*8, intent(in), dimension(3) :: A
        real*8 norm
        norm = dsqrt(dot_product(A,A))
    Return
    End Function
End Module
```

```
PROGRAM QM_Spectrum_higher_order_mpi
    use mpi
    implicit none
    integer, parameter :: Nw = 4000
    real*8 wmid,wlow,wstep
    real*8 w,weng
    integer i, ii
    real*8, dimension(Nw,3) :: qeng
    real*8, dimension(:,:), allocatable :: qeng_local
    integer numnodes,myid,rc,ierr,start_local,end_local,Nw_local
    real*8 wsigma
    common/sigmaE/ wsigma

    call mpi_init( ierr )
    call mpi_comm_rank ( mpi_comm_world, myid, ierr )
    call mpi_comm_size ( mpi_comm_world, numnodes, ierr )

    Nw_local = Nw/numnodes
    allocate ( qeng_local(Nw_local,3) )
    start_local = Nw_local*myid + 1
    end_local =  Nw_local*myid + Nw_local

    open(unit=12,file='data.dat')

    wmid = 1d16*2d0;
    wlow = wmid*0.05d0
    wstep = 2*dabs(wmid-wlow)/(Nw-1d0)
    do i = start_local,end_local
        w = wlow + (i-1)*wstep
        ii = i - Nw_local*myid
        qeng_local(ii,1) = w
        qeng_local(ii,2) = weng(w)
        qeng_local(ii,3) = wsigma

!   if ( MOD(i,Nw/10) == 0) then
!   write(6,105) (i*100)/Nw
!   endif
    enddo

    do i = 1,3
        call mpi_gather ( qeng_local(:,i), Nw_local, mpi_real8, qeng(:,i), Nw_local, &
                          & mpi_real8, 0, mpi_comm_world, ierr )
    enddo
    if (myid == 0) then
        do i = 1,Nw
            write(12,102) qeng(i,:)
        enddo
    endif


    call mpi_finalize(rc)
    deallocate( qeng_local )

    666 format(A, 10E25.15E4)
    102 format(10E25.15E4)
    105  format(I4,'%')


STOP
END

FUNCTION weng(w)
    implicit none
```

```
    real*8, intent(in) :: w
    real*8 weng
    integer, parameter :: NN = 20
    integer, parameter :: neq = 2*NN
    real*8 y(neq),dydt(neq)
    external derivs,rkqs
    integer nbad,nok
    real*8 tbgn,tstep,tend,tol
    integer i
    real*8 Eng2(NN),Eng(NN),hbar,c,w0,q,mm,pi,t0,E0,A0,Dt,Dx,phs,k_phi,k_theta,pol_phi, &
           & pol_theta,kv(3),pol(3)
    common/par/ Eng2,Eng,hbar,c,w0,q,mm,pi,t0,E0,A0,Dt,Dx,phs,k_phi,k_theta,pol_phi, &
           & pol_theta,kv,pol
    real*8, dimension(NN,NN) :: wnm
    common/wmtrix/ wnm
    real*8 t,tmax
    integer Nt
    complex*16, parameter :: lj = (0d0,1d0)
    complex*16 Cn(NN)
    real*8 Pn(NN)
    real*8 wsigma
    common/sigmaE/ wsigma
    real*8 tmid
    common/center/ tmid
    real*8 ww
    common/freq/ ww

    ww = w

    call parameters(w)
    tol = 1d-3  !tol = 1d-6 for FINAL CHECK
    tbgn = 0d0
    do i = 1,neq
        y(i) = 0d0
    enddo
    y(1) = 1d0

    Nt = int(4e4);
    tstep = (2*pi/w0/80)/t0;       !dimensionless
    tmax = Nt*tstep;
    tmid = tmax/2d0*t0
    do i = 1,Nt
    tend = tbgn + tstep
    t = tbgn
    call Hmatrix(t*t0)      ! in-loop (derivs) for FINAL CHECK
    call odeint(y,neq,tbgn,tend,tol,tstep,0d0,nok,nbad,derivs,rkqs)
    tbgn = tend   !odient does not change (tbgn,tend)
    enddo
    do i = 0,NN-1
        Cn(i+1) = y(i+1)+lj*y(i+1+NN)
        Pn(i+1) = cdabs(Cn(i+1))**2
    enddo
    weng = dot_product(Pn,Eng)
    wsigma = dsqrt( abs( dot_product(Pn,Eng2)-weng**2d0 ) )
RETURN
END FUNCTION


SUBROUTINE parameters(w)
    implicit none
    real*8 w
    integer, parameter :: NN = 20
    real*8, dimension(NN,NN) :: wnm
    common/wmtrix/ wnm
```

```
    real*8 Eng2(NN),Eng(NN),hbar,c,w0,q,mm,pi,t0,E0,A0,Dt,Dx,phs,k_phi,k_theta,pol_phi, &
           & pol_theta,kv(3),pol(3)
    common/par/ Eng2,Eng,hbar,c,w0,q,mm,pi,t0,E0,A0,Dt,Dx,phs,k_phi,k_theta,pol_phi, &
           & pol_theta,kv,pol
    integer i,j
    real*8 n, m
    real*8, dimension(NN,NN) :: ap, an
    real*8, dimension(NN,NN) :: xMtrix
    complex*16, dimension(NN,NN) :: pMtrix
    common/xp/ xMtrix, pMtrix
    complex*16, parameter :: lj = (0d0,1d0)
    real*8 kd

    hbar = 1.05457d-34
    c = 2.99792d8
    w0 = 1d16
    q = 1.60218d-19
    mm = 9.10938d-31*1d-4
    pi=dacos(-1d0)
    t0 = 1d-16
    E0 = hbar/t0
    A0 = 1.5d-9
    Dt = 1d-14
    Dx = c*Dt
    phs = 0d0
    k_phi = 0
    k_theta = pi/4          !NOTE: k_theta = zero at x-axis
    pol_phi = 0
    pol_theta = k_theta+pi/2    !NOTE: k_theta = zero at x-axis
    kv(1) = w/c*dcos(k_theta)*dcos(k_phi)
    kv(2) = w/c*dcos(k_theta)*dsin(k_phi)
    kv(3) = w/c*dsin(k_theta)
    pol(1) = dcos(pol_theta)*dcos(pol_phi)
    pol(2) = dcos(pol_theta)*dsin(pol_phi)
    pol(3) = dsin(pol_theta)
    do i = 0,NN-1
        n = i*1d0;
        Eng(i+1) = hbar*w0*(n+0.5d0)
        Eng2(i+1) = Eng(i+1)**2d0
    enddo
    do i = 0,NN-1
        do j = 0,NN-1
            wnm(i+1,j+1) = (Eng(i+1)-Eng(j+1))/hbar
        enddo
    enddo
    do i = 0,NN-1
        do j = 0,NN-1
            n = i*1d0
            m = j*1d0
            ap(i+1,j+1) = dsqrt(n)*kd(n-1,m)
            an(i+1,j+1) = dsqrt(n+1)*kd(n+1,m)
        enddo
    enddo
    xMtrix = dsqrt(hbar/(2d0*mm*w0))*(ap + an)
    pMtrix = lj*dsqrt(hbar*mm*w0/2d0)*(ap - an)

RETURN
END SUBROUTINE


SUBROUTINE derivs(t,y,dydt)
    implicit none
    integer, parameter :: NN = 20
    integer, parameter :: neq = 2*NN
```

```
    real*8 t,y(neq),dydt(neq)
    real*8, dimension(2*NN,2*NN) :: Hint
    common/Hmtrix/ Hint
    real*8 Eng2(NN),Eng(NN),hbar,c,w0,q,mm,pi,t0,E0,A0,Dt,Dx,phs,k_phi,k_theta,pol_phi, &
           & pol_theta,kv(3),pol(3)
    common/par/ Eng2,Eng,hbar,c,w0,q,mm,pi,t0,E0,A0,Dt,Dx,phs,k_phi,k_theta,pol_phi, &
           & pol_theta,kv,pol
    integer i

!   call Hmatrix(t*t0)  !for FINAL CHECK
    dydt = matmul(Hint,y)

RETURN
END SUBROUTINE


SUBROUTINE Hmatrix(t)
    use vector_functions
    use matrix_functions
    implicit none
    real*8, intent(in) :: t
    integer, parameter :: NN = 20
    complex*16, parameter :: lj = (0d0,1d0)
    real*8 kd
    real*8 Eng2(NN),Eng(NN),hbar,c,w0,q,mm,pi,t0,E0,A0,Dt,Dx,phs,k_phi,k_theta,pol_phi, &
           & pol_theta,kv(3),pol(3)
    common/par/ Eng2,Eng,hbar,c,w0,q,mm,pi,t0,E0,A0,Dt,Dx,phs,k_phi,k_theta,pol_phi, &
           & pol_theta,kv,pol
    real*8 xv(3)
    integer i,j
    real*8 n,m
    real*8, dimension(NN,NN) :: wnm
    common/wmtrix/ wnm
    real*8, dimension(NN,NN) :: xMtrix
    complex*16, dimension(NN,NN) :: pMtrix
    common/xp/ xMtrix, pMtrix
    real*8, dimension(NN,NN) :: kr, kxDx, Ax2, kxtDxDt, Ax3, AMtrix
    complex*16, dimension(NN,NN) :: ikr, Ax1, AMtrixC
    complex*16, dimension(NN,NN) :: Hnm1, Hnm2, Hnm
    real*8, dimension(NN,NN) :: HnmR, HnmI
    real*8, dimension(NN,NN) :: HintR, HintI
    real*8, dimension(2*NN,2*NN) :: Hint
    common/Hmtrix/ Hint
    real*8, dimension(2*NN,1) :: vc
    real*8 tmid
    common/center/ tmid
    real*8 ww
    common/freq/ ww

    xv = (/1d0,0d0,0d0/)
    kr = dot(kv,xv)*xMtrix
    ikr = lj*kr
    Ax1 = cexpM(20,ikr,NN)                  !Order of Approximation, Spatial Effect
    kxDx = dot(kv,xv)/(norm(kv)*Dx)*xMtrix
    Ax2 = expM(20,-matmul(kxDx,kxDx),NN)        !Order of Approximation, Spatial Effect
    kxtDxDt = 2d0*(t-tmid)/Dt*kxDx
    Ax3 = expM(20,kxtDxDt,NN)               !Order of Approximation, Spatial Effect
    AMtrixC = A0*cdexp(lj*ww*(t-tmid))*dexp(-( (t-tmid)/Dt )**2d0)*matmul3(NN, Ax1, Ax2, Ax3)
    AMtrix = dreal(AMtrixC)

    Hnm1 = -q/(2d0*mm)*( 2d0*dot(pol,xv)*matmul(AMtrix,pMtrix) )
    Hnm2 = -q/(2d0*mm)*( -q*matmul(AMtrix,AMtrix) )
    Hnm = Hnm1 + Hnm2
    do i = 0,NN-1
```

```
        do j = 0,NN-1
            n = i*1d0
            m = j*1d0
            Hnm(i+1,j+1) = Hnm(i+1,j+1)*cdexp(lj*wnm(i+1,j+1)*t)
        enddo
    enddo
    HnmR = dreal(Hnm)
    HnmI = dimag(Hnm)
    do j = 1,NN
        vc = reshape( (/HnmI(:,j),-HnmR(:,j)/), (/2*NN,1/) )
        Hint(:,j) = vc(:,1)
    enddo
    do j = 1,NN
        vc = reshape( (/HnmR(:,j),HnmI(:,j)/), (/2*NN,1/) )
        Hint(:,j+NN) = vc(:,1)
    enddo

    Hint = 1d0/hbar*(Hint/E0)*(E0*t0)
RETURN
END SUBROUTINE




!~~~~~~~~~~~~~~~~~~~~~~~~~~~~~~~~~~~~~~~~~~~~~~~~~~~~~~~~~~~~
!~~~~~~~~~~~~~~~~~~~~~~~~~~~~~~~~~~~~~~~~~~~~~~~~~~~~~~~~~~~~
SUBROUTINE odeint(ystart,nvar,x1,x2,eps,h1,hmin,nok,nbad,derivs,rkqs)
    INTEGER nbad,nok,nvar,KMAXX,MAXSTP,NMAX
    REAL*8 eps,h1,hmin,x1,x2,ystart(nvar),TINY
    EXTERNAL derivs,rkqs
    PARAMETER(MAXSTP=1000000000,NMAX=50,KMAXX=200,TINY=1d-30)
                !use MAXSTP=10 to get the solver running then increase to MAXSTP=10000
    INTEGER i,kmax,kount,nstp
    REAL*8 dxsav,h,hdid,hnext,x,xsav,dydx(NMAX),xp(KMAXX),y(NMAX),yp(NMAX,KMAXX),yscal(NMAX)
!   COMMON/path/kmax,kount,dxsav,xp,yp
    PARAMETER (dxsav=0.1d0,kmax=100)
    x=x1
    h=sign(h1,x2-x1)
    nok=0
    nbad=0
    kount=0
    do i=1,nvar
        y(i)=ystart(i)
    enddo
    if (kmax.gt.0) xsav=x-2d0*dxsav
    do nstp=1,MAXSTP
        call derivs(x,y,dydx)
        do i=1,nvar
            yscal(i)=abs(y(i))+abs(h*dydx(i))+TINY
!           yscal(i)=1d0
        enddo
        if(kmax.gt.0)then
            if(abs(x-xsav).gt.abs(dxsav))then
                if(kount.lt.kmax-1)then
                    kount=kount+1
                    xp(kount)=x
                    do i=1,nvar
                        yp(i,kount)=y(i)
                    enddo
                    xsav=x
                endif
            endif
        endif
```

```
        if((x+h-x2)*(x+h-x1).gt.0.)h=x2-x
        call rkqs(y,dydx,nvar,x,h,eps,yscal,hdid,hnext,derivs)
        if(hdid.eq.h)then
            nok=nok+1
        else
            nbad=nbad+1
        endif
        if((x-x2)*(x2-x1).ge.0.)then
            do i=1,nvar
            ystart(i)=y(i)
            enddo
            if(kmax.ne.0)then
                kount=kount+1
                xp(kount)=x
                do i=1,nvar
                    yp(i,kount)=y(i)
                enddo
            endif
            return
        endif
!pause -> write(6,*)
        if(abs(hnext).lt.hmin) write(6,*) "stepsize smaller than minimum in odeint"
        h=hnext
    enddo
!pause => write(6,*)
    write(6,*) "too many steps in odeint"
    return
END SUBROUTINE odeint

SUBROUTINE rkqs(y,dydx,n,x,htry,eps,yscal,hdid,hnext,derivs)
    INTEGER n,NMAX
    REAL*8 eps,hdid,hnext,htry,x,dydx(n),y(n),yscal(n)
    EXTERNAL derivs
    PARAMETER(NMAX=50)
    INTEGER i
    REAL*8 errmax,h,htemp,xnew,yerr(NMAX),ytemp(NMAX),SAFETY,PGROW,PSHRNK,ERRCON
    PARAMETER(SAFETY=0.9d0,PGROW=-0.2d0,PSHRNK=-0.25d0,ERRCON=1.89d-4)
    h=htry
    1 call rkck(y,dydx,n,x,h,ytemp,yerr,derivs)
    errmax=0.
    do i=1,n
        errmax=max(errmax,abs(yerr(i)/yscal(i)))
    enddo
    errmax=errmax/eps
    if(errmax.gt.1d0)then
        htemp=SAFETY*h*(errmax**PSHRNK)
        h=sign(max(abs(htemp),0.1d0*abs(h)),h)
        xnew=x+h
!pause -> write(6,*)
        if(xnew.eq.x) write(6,*) "step size underflow in rkqs"
        go to 1
    else
        if(errmax.gt.ERRCON)then
            hnext=SAFETY*h*(errmax**PGROW)
        else
            hnext=5d0*h
        endif
        hdid=h
        x=x+h
        do i=1,n
            y(i)=ytemp(i)
        enddo
        return
    endif
```

```
END SUBROUTINE rkqs

SUBROUTINE rkck(y,dydx,n,x,h,yout,yerr,derivs)
    INTEGER n,NMAX
    REAL*8 h,x,dydx(n),y(n),yerr(n),yout(n)
    EXTERNAL derivs
    PARAMETER(NMAX=50)
    INTEGER i
    REAL*8 ak2(NMAX),ak3(NMAX),ak4(NMAX),ak5(NMAX),ak6(NMAX),ytemp(NMAX),A2,A3,A4,A5,A6,B21, &
    & B31,B32,B41,B42,B43,B51,B52,B53,B54,B61,B62,B63,B64,B65,C1,C3,C4,C6,DC1,DC3,DC4,DC5,DC6
    PARAMETER(A2=0.2d0,A3=0.3d0,A4=0.6d0,A5=1.0d0,A6=0.875d0,B21=0.2d0,B31=3.0d0/40.0d0,&
    & B32=9.0d0/40.0d0,B41=0.3d0,B42=-0.9d0,B43=1.2d0,B51=-11.0d0/54.0d0,B52=2.5d0, &
    & B53=-70.0d0/27.0d0,B54=35.0d0/27.0d0,B61=1631.0d0/55296.0d0,B62=175.0d0/512.0d0, &
    & B63=575.0d0/13824.0d0,B64=44275.0d0/110592.0d0,B65=253.0d0/4096.0d0,C1=37.0d0/378.0d0, &
    & C3=250.0d0/621.0d0,C4=125.0d0/594.0d0,C6=512.0d0/1771.0d0,DC1=C1-2825.0d0/27648.0d0, &
    & DC3=C3-18575.0d0/48384.0d0,DC4=C4-13525.0d0/55296.0d0,DC5=-277.0d0/14336.0d0,DC6=C6-0.25d0)
    do i=1,n
    ytemp(i)=y(i)+B21*h*dydx(i)
    enddo
    call derivs(x+A2*h,ytemp,ak2)
        do i=1,n
        ytemp(i)=y(i)+h*(B31*dydx(i)+B32*ak2(i))
    enddo
    call derivs(x+A3*h,ytemp,ak3)
    do i=1,n
        ytemp(i)=y(i)+h*(B41*dydx(i)+B42*ak2(i)+B43*ak3(i))
    enddo
    call derivs(x+A4*h,ytemp,ak4)
    do i=1,n
        ytemp(i)=y(i)+h*(B51*dydx(i)+B52*ak2(i)+B53*ak3(i)+B54*ak4(i))
    enddo
    call derivs(x+A5*h,ytemp,ak5)
    do i=1,n
        ytemp(i)=y(i)+h*(B61*dydx(i)+B62*ak2(i)+B63*ak3(i)+B64*ak4(i)+B65*ak5(i))
    enddo
    call derivs(x+A6*h,ytemp,ak6)
    do i=1,n
        yout(i)=y(i)+h*(C1*dydx(i)+C3*ak3(i)+C4*ak4(i)+C6*ak6(i))
    enddo
    do i=1,n
        yerr(i)=h*(DC1*dydx(i)+DC3*ak3(i)+DC4*ak4(i)+DC5*ak5(i)+DC6*ak6(i))
    enddo
    return
END SUBROUTINE rkck
!~~~~~~~~~~~~~~~~~~~~~~~~~~~~~~~~~~~~~~~~~~~~~~~~~~~~~~~~~~~~~~~~~~~~~~~~~~~
!~~~~~~~~~~~~~~~~~~~~~~~~~~~~~~~~~~~~~~~~~~~~~~~~~~~~~~~~~~~~~~~~~~~~~~~~~~~

!~~~~~~~~~~~~~~~~~~~
!include for matrix_functions (below)
!~~~~~~~~~~~~~~~~~~~
FUNCTION kd(n,m)
    implicit none
    real*8, intent(in) :: n,m
    real*8 kd

    if (n == m) then
        kd = 1d0;
    else
        kd = 0d0;
    endif
RETURN
END FUNCTION

FUNCTION factrl(n)
```

```
    implicit none
    integer n
    real*8 factrl
    integer j,ntop
    real*8 a(33),gammln
    save ntop,a
    data ntop,a(1)/0,1./
    if (n.lt.0) then
        return
        write(6,*) 'negative factorial in factrl'
    else if (n.le.ntop) then
        factrl=a(n+1)
    else if (n.le.32) then
        do  j=ntop+1,n
            a(j+1)=j*a(j)
        enddo
        ntop=n
        factrl=a(n+1)
    else
        factrl=exp(gammln(n+1d0))
    endif
RETURN
END FUNCTION

FUNCTION gammln(xx)
    implicit none
    real*8 gammln,xx
    integer j
    real*8 ser,stp,tmp,x,y,cof(6)
    save cof,stp
    data cof,stp/76.18009172947146d0,-86.50532032941677d0,24.01409824083091d0 &
            ,-1.231739572450155d0,.1208650973866179d-2,-.5395239384953d-5,2.506628274631000 5d0/
    x=xx
    y=x
    tmp=x+5.5d0
    tmp=(x+0.5d0)*log(tmp)-tmp
    ser=1.000000000190015d0
    do j=1,6
        y=y+1.d0
        ser=ser+cof(j)/y
    enddo
    gammln=tmp+log(stp*ser/x)
RETURN
END FUNCTION

!~~~~~~~~~~~~~~~~~~~
!include for matrix_functions (above)
!~~~~~~~~~~~~~~~~~~~


SUBROUTINE mwrite(A,N,M)
    implicit none
    integer, intent(in) :: N, M
    real*8, dimension(N,M), intent(in) :: A
    integer i

    do i = lbound(A,1),ubound(A,1)
        write(6,*) A(i,:)
    enddo
RETURN
END SUBROUTINE


SUBROUTINE cmwrite(A,N,M)
```

```
    implicit none
    integer, intent(in) :: N, M
    complex*16, dimension(N,M), intent(in) :: A
    integer i
    do i = lbound(A,1),ubound(A,1)
        write(6,*) A(i,:)
    enddo
RETURN
END SUBROUTINE
```

```
Module vector_functions
    implicit none
    contains

    Function dot(A,B)
        real*8,intent(in),dimension(3) :: A,B
        real*8 dot
        dot = dot_product(A,B)
    Return
    End Function

    Function cross(A,B)
        real*8,intent(in),dimension(3) :: A,B
        real*8,dimension(3) :: cross

        cross(1) = A(2)*B(3)-A(3)*B(2)
        cross(2) = A(3)*B(1)-A(1)*B(3)
        cross(3) = A(1)*B(2)-A(2)*B(1)
    Return
    End Function

    Function norm(A)
        real*8,intent(in),dimension(3) :: A
        real*8 norm
        norm = dsqrt(dot_product(A,A))
    Return
    End Function
End Module


Program RED_spectrum_mpi
    use mpi
    use vector_functions
    implicit none
    integer, parameter :: Nw = 3000
    real*8 wmid, wbgn, wend, wstep, wp
    real*8, dimension(Nw,3) :: gEng, eEng, gEng2, eEng2
    integer, parameter :: Np = 2000
    integer i, k
    real*8 c, hbar, eps, pi, w0, q, mm, Gamma, Dw0, cohtime, a0, t0, Smtrix(3,3), Dmtrix(3,3)
    common/pra/ c, hbar, eps, pi, w0, q, mm, Gamma, Dw0, cohtime, a0, t0, Smtrix, Dmtrix
    real*8, dimension(:,:), allocatable :: gr_local, gp_local, er_local, ep_local
    integer numnodes, myid, rc, ierr, Np_local
    real*8, dimension(3) :: tgEng, teEng, tgEng2, teEng2
    integer particleid, id_local
    real*8 ran1
    integer workerseed, particleseed
    real*8, dimension(3) :: gavgE, gavgE2, gsigmaE, eavgE, eavgE2, esigmaE

    call mpi_init( ierr )
    call mpi_comm_rank ( mpi_comm_world, myid, ierr )
    call mpi_comm_size ( mpi_comm_world, numnodes, ierr )
    Np_local = Np/numnodes
    allocate ( gr_local(Np_local,3) )
    allocate ( gp_local(Np_local,3) )
    allocate ( er_local(Np_local,3) )
    allocate ( ep_local(Np_local,3) )

    open(unit=11, file ='Spectrum_x.dat')
    open(unit=12, file ='Spectrum_y.dat')
    open(unit=13, file ='Spectrum_z.dat')

    workerseed = -(myid+1)
```

```
    call parameters

    wmid = w0*2d0
    wbgn = wmid*0.05d0
    wend = wbgn + 2d0*dabs(wmid-wbgn)
    wstep = dabs(wbgn-wend)/(Nw-1d0)
    gEng = 0d0
    eEng = 0d0
    gEng2 = 0d0
    eEng2 = 0d0
    do k = 1, Nw
        wp = wbgn + (k-1d0)*wstep
        gr_local = 0d0
        gp_local = 0d0
        er_local = 0d0
        ep_local = 0d0
        do i = 1, Np_local
            id_local = i
            particleseed = int(ran1(workerseed)*1d6)
            call RED_worker(wp, id_local, Np_local, particleseed, gr_local, gp_local, er_local, ep_local)
!           particleid = myid*Np_local + id_local               !for checking purpose
!           write(6,*) 'frequency', k, particleid, particleseed
            !the same particle would experience different vacuum field at different laser frequency
        enddo
        do i = 1,3
            gEng(k,i) = sum( 5d-1*mm*w0**2d0*gr_local(:,i)**2d0 + 5d-1/mm*gp_local(:,i)**2d0 )
            eEng(k,i) = sum( 5d-1*mm*w0**2d0*er_local(:,i)**2d0 + 5d-1/mm*ep_local(:,i)**2d0 )
            gEng2(k,i) = sum( (5d-1*mm*w0**2d0*gr_local(:,i)**2d0 + 5d-1/mm*gp_local(:,i)**2d0)**2d0 )
            eEng2(k,i) = sum( (5d-1*mm*w0**2d0*er_local(:,i)**2d0 + 5d-1/mm*ep_local(:,i)**2d0)**2d0 )

        enddo
        do i = 1,3
            call mpi_reduce( gEng(k,i), tgEng(i), 1, mpi_real8, mpi_sum, 0, mpi_comm_world, ierr )
            call mpi_reduce( eEng(k,i), teEng(i), 1, mpi_real8, mpi_sum, 0, mpi_comm_world, ierr )
            call mpi_reduce( gEng2(k,i), tgEng2(i), 1, mpi_real8, mpi_sum, 0, mpi_comm_world, ierr )
            call mpi_reduce( eEng2(k,i), teEng2(i), 1, mpi_real8, mpi_sum, 0, mpi_comm_world, ierr )
        enddo
        if ( myid == 0 ) then
            do i = 1,3
                gavgE(i) = tgEng(i)/(Np*1d0)
                eavgE(i) = teEng(i)/(Np*1d0)
                gavgE2(i) = tgEng2(i)/(Np*1d0)
                eavgE2(i) = teEng2(i)/(Np*1d0)
                gsigmaE(i) = dsqrt( gavgE2(i) - gavgE(i)**2d0)
                esigmaE(i) = dsqrt( eavgE2(i) - eavgE(i)**2d0)
            enddo
            write(11,102) wp, gavgE(1), eavgE(1), gsigmaE(1), esigmaE(1)
            write(12,102) wp, gavgE(2), eavgE(2), gsigmaE(2), esigmaE(2)
            write(13,102) wp, gavgE(3), eavgE(3), gsigmaE(3), esigmaE(3)
        endif
        tgEng = 0d0
        teEng = 0d0
        tgEng2 = 0d0
        teEng2 = 0d0
        gavgE = 0d0
        eavgE = 0d0
        gavgE2 = 0d0
        eavgE2 = 0d0
        gsigmaE = 0d0
        esigmaE = 0d0

    enddo
    102 format(10E25.15E4)
    104 format(10E25.15E4)
```

```
    if ( myid == 0 ) then
        write(6,*) '# of pulse frequency, Nw =', Nw
        write(6,*) '# of particle, Np =', Np
    endif


    call mpi_finalize(rc)
    deallocate( gr_local )
    deallocate( gp_local )
    deallocate( er_local )
    deallocate( ep_local )

Stop
End Program



SUBROUTINE RED_worker(wp, id_local, Np_local, particleseed, gr, gp, er, ep)
    implicit none
    real*8, intent(in) :: wp
    integer, intent(in) ::  id_local, Np_local, particleseed
    real*8, dimension(Np_local,3) :: gr, gp, er, ep
    integer, parameter :: neq = 6
    real*8 t, y(neq), dydt(neq)
    external derivs,rkqs
    integer nbad,nok
    real*8 tbgn,tstep,tend,tol
    integer i, Nt
    real*8 w, AA, Dt, Dx, k_phi, k_theta, pol_phi, pol_theta
    real*8, dimension(3) :: kv, pol
    common/pulse_pra/ w, AA, Dt, Dx, k_phi, k_theta, pol_phi, pol_theta, kv, pol
    real*8 c, hbar, eps, pi, w0, q, mm, Gamma, Dw0, cohtime, a0, t0, Smtrix(3,3), Dmtrix(3,3)
    common/pra/ c, hbar, eps, pi, w0, q, mm, Gamma, Dw0, cohtime, a0, t0, Smtrix, Dmtrix
    real*8, dimension(3) :: r, v
    real*8 tmax
    integer, parameter :: Wmodes = 500   !INPUT
    real*8 gprobe, eprobe, gap
    real*8 tmid
    common/center/tmid


    call pulseParameters(wp)
    call vacParameters(particleseed)
    tol = 1d-3  !tol = 1d-6 for FINAL CHECK
    y = 0d0     !IC, dimensionless
    tbgn = 0d0
    tmax = (cohtime*7d0)/t0         !make tmax > cohtime*2d0
    tstep = (2d0*pi/w0/2d1)/t0      !dimensionless
    Nt = int(tmax/tstep)
    tmid = (cohtime)*2d0 + (tmax*t0-(cohtime)*2d0)/2d0
    gprobe = tmid/t0 - 3d0*(Dt/t0)
    eprobe = tmid/t0 + 2d0*(Dt/t0)
    gap = (2d0*pi/w0)/t0
    do i = 1,Nt
        tend = tbgn + tstep
        t = tbgn
        r = (/y(1),y(2),y(3)/)
        v = (/y(4),y(5),y(6)/)
        if ( (gprobe < t).and.(t < gprobe+gap ) ) then
            gr(id_local,:) = r*a0
            gp(id_local,:) = v*mm*(a0/t0)
        endif
        if ( (eprobe < t).and.(t < eprobe+gap ) ) then
```

```
            er(id_local,:) = r*a0
            ep(id_local,:) = v*mm*(a0/t0)
        endif
        call vacfield(r*a0,t*t0)    !in-loop (dervis) for FINAL CHECK
        call pulsefield(r*a0,t*t0)  !in-loop (dervis) for FINAL CHECK
        call odeint(y,neq,tbgn,tend,tol,tstep,0d0,nok,nbad,derivs,rkqs)
        tbgn = tend
    enddo
RETURN
END SUBROUTINE


SUBROUTINE parameters
    implicit none
    real*8 c, hbar, eps, pi, w0, q, mm, Gamma, Dw0, cohtime, a0, t0, Smtrix(3,3), Dmtrix(3,3)
    common/pra/ c, hbar, eps, pi, w0, q, mm, Gamma, Dw0, cohtime, a0, t0, Smtrix, Dmtrix
    real*8, dimension(3) :: Sprgx, Sprgy, Sprgz, Dmpx, Dmpy, Dmpz

    c = 2.99792d8
    hbar = 1.05457d-34
    eps = 8.85419d-12
    pi = dacos(-1d0)
    w0 = 1d16
    q = 1.60218d-19
    mm = 9.10938d-31*1d-4 !it was 9.11d-31
    Gamma = 2d0/3d0*(q**2d0)/(mm*c**3d0)/(4d0*pi*eps)
    Dw0 = Gamma*w0**2d0
    cohtime = 2d0/Dw0
    a0 = dsqrt(hbar/(2d0*mm*w0))
    t0 = 1d0/w0

    Sprgx = (/1d0,0d0,0d0/)*1d0
    Sprgy = (/0d0,1d0,0d0/)*0d0
    Sprgz = (/0d0,0d0,1d0/)*0d0
    Smtrix = reshape((/Sprgx,Sprgy,Sprgz/),(/3,3/))  !3D harmonic oscillator

    Dmpx = (/1d0,0d0,0d0/)*1d0
    Dmpy = (/0d0,1d0,0d0/)*1d0
    Dmpz = (/0d0,0d0,1d0/)*1d0
    Dmtrix = reshape((/Dmpx,Dmpy,Dmpz/),(/3,3/))  !3D damper
RETURN
END SUBROUTINE


SUBROUTINE vacParameters(particleseed)
    implicit none
    integer, intent(in) :: particleseed
    integer, parameter :: Wmodes = 500
    real*8 ran1
    integer seed
    real*8 vacDw, wc, kbgn, kend, volk, volr, dkapa, kapa, kapa_theta, kapa_phi
    real*8, dimension(Wmodes) :: kmvac, thetavac, phivac, wvac, phir, Amvac, Emvac, Bmvac
    real*8, dimension(Wmodes,3) :: kvac
    real*8, dimension(Wmodes,2) :: phsvac
    real*8, dimension(Wmodes,3,2) :: polvac
    common/vac_pra/ kmvac, thetavac, phivac, wvac, phir, Amvac, Emvac, Bmvac, kvac, phsvac, polvac
    real*8 c, hbar, eps, pi, w0, q, mm, Gamma, Dw0, cohtime, a0, t0, Smtrix(3,3), Dmtrix(3,3)
    common/pra/ c, hbar, eps, pi, w0, q, mm, Gamma, Dw0, cohtime, a0, t0, Smtrix, Dmtrix
    integer i

    seed = -particleseed
    vacDw = Dw0*22d1   !INPUT
    wc = w0*1d0
    kbgn = (wc - vacDw/2d0)/c
```

```
    kend = (wc + vacDw/2d0)/c
    volk = 4d0*pi/3d0*(kend**3d0-kbgn**3d0)
    volr = (2d0*pi)**3d0*(Wmodes*1d0)/volk
    dkapa = ( kend**3d0/3d0 - kbgn**3d0/3d0 )/(Wmodes*1d0 - 1d0)

    do i=1,Wmodes
            kapa = kbgn**3d0/3d0 + (i*1d0-1d0)*dkapa
            kapa_theta = (ran1(seed) - 5d-1)*2d0
            kapa_phi = ran1(seed)*2d0*pi

            kmvac(i) =  (3d0*kapa)**(1d0/3d0)
            thetavac(i) = dacos(kapa_theta)
            phivac(i) = kapa_phi
            kvac(i,1) = kmvac(i)*dsin(thetavac(i))*dcos(phivac(i))
            kvac(i,2) = kmvac(i)*dsin(thetavac(i))*dsin(phivac(i))
            kvac(i,3) = kmvac(i)*dcos(thetavac(i))
            wvac(i) = kmvac(i)*c

            phsvac(i,1) = ran1(seed)*2d0*pi
            phsvac(i,2) = ran1(seed)*2d0*pi

            phir(i) = ran1(seed)*2d0*pi
            polvac(i,1,1) = dcos(thetavac(i))*dcos(phivac(i))*dcos(phir(i)) - dsin(phivac(i))*dsin(phir(i))
            polvac(i,2,1) = dcos(thetavac(i))*dsin(phivac(i))*dcos(phir(i)) + dcos(phivac(i))*dsin(phir(i))
            polvac(i,3,1) = -dsin(thetavac(i))*dcos(phir(i))
            polvac(i,1,2) = -dcos(thetavac(i))*dcos(phivac(i))*dsin(phir(i)) - dsin(phivac(i))*dcos(phir(i))
            polvac(i,2,2) =  -dcos(thetavac(i))*dsin(phivac(i))*dsin(phir(i)) + dcos(phivac(i))*dcos(phir(i))
            polvac(i,3,2) =  dsin(thetavac(i))*dsin(phir(i))

            Amvac(i) = dsqrt( hbar/wvac(i)/eps/volr )
            Emvac(i) = Amvac(i)*wvac(i)
            Bmvac(i) = Amvac(i)
    enddo



RETURN
END

SUBROUTINE vacField(r,t)    !(r,t) have original dimension
    use vector_functions
    implicit none
    real*8, intent(in) :: r(3),t
    integer, parameter :: Wmodes = 500
    real*8, dimension(3) :: Evac, Bvac
    common/vac_field/ Evac, Bvac
    real*8, dimension(Wmodes) :: kmvac, thetavac, phivac, wvac, phir, Amvac, Emvac, Bmvac
    real*8, dimension(Wmodes,3) :: kvac
    real*8, dimension(Wmodes,2) :: phsvac
    real*8, dimension(Wmodes,3,2) :: polvac
    common/vac_pra/ kmvac, thetavac, phivac, wvac, phir, Amvac, Emvac, Bmvac, kvac, phsvac, polvac
    real*8, dimension(Wmodes) :: kr,wt
    real*8, dimension(Wmodes,3) :: E1, E2, B1, B2, Ek, Bk
    integer i

    do i = 1, Wmodes
        kr(i) = dot(kvac(i,:),r)
        wt(i) = wvac(i)*t
        E1(i,:) = -Emvac(i)*dsin( kr(i)-wt(i)+phsvac(i,1) )*polvac(i,:,1)
        E2(i,:) = -Emvac(i)*dsin( kr(i)-wt(i)+phsvac(i,2) )*polvac(i,:,2)
        B1(i,:) = -Bmvac(i)*dsin( kr(i)-wt(i)+phsvac(i,1) )*cross(kvac(i,:),polvac(i,:,1))
        B2(i,:) = -Bmvac(i)*dsin( kr(i)-wt(i)+phsvac(i,2) )*cross(kvac(i,:),polvac(i,:,2))
    enddo
    Ek = E1 + E2
```

```
    Evac = sum(Ek,1)
    Bk = B1 + B2
    Bvac = sum(Bk,1)
RETURN
END

SUBROUTINE pulseParameters(wp)
    implicit none
    real*8, intent(in) :: wp
    real*8 w, AA, Dt, Dx, k_phi, k_theta, pol_phi, pol_theta
    real*8, dimension(3) :: kv, pol
    common/pulse_pra/ w, AA, Dt, Dx, k_phi, k_theta, pol_phi, pol_theta, kv, pol
    real*8 c, hbar, eps, pi, w0, q, mm, Gamma, Dw0, cohtime, a0, t0, Smtrix(3,3), Dmtrix(3,3)
    common/pra/ c, hbar, eps, pi, w0, q, mm, Gamma, Dw0, cohtime, a0, t0, Smtrix, Dmtrix

    w = wp
    AA = 1.5d-9
    Dt = 1d-14
    Dx = c*Dt
    k_phi = 0
    k_theta = pi/4              !NOTE: k_theta follows the convention in Matlab
    pol_phi = 0
    pol_theta = k_theta+pi/2    !NOTE: pol_theta follows the convention in Matlab
    kv(1) = w/c*dcos(k_theta)*dcos(k_phi)
    kv(2) = w/c*dcos(k_theta)*dsin(k_phi)
    kv(3) = w/c*dsin(k_theta)
    pol(1) = dcos(pol_theta)*dcos(pol_phi)
    pol(2) = dcos(pol_theta)*dsin(pol_phi)
    pol(3) = dsin(pol_theta)
RETURN
END

SUBROUTINE pulseField(r,t)  !(r, t, tmid) have original dimension
    use vector_functions
    implicit none
    real*8, intent(in) :: r(3), t
    real*8, dimension(3) :: Epulse, Bpulse
    common/pulse_field/ Epulse, Bpulse
    real*8 w, AA, Dt, Dx, k_phi, k_theta, pol_phi, pol_theta
    real*8, dimension(3) :: kv, pol
    common/pulse_pra/ w, AA, Dt, Dx, k_phi, k_theta, pol_phi, pol_theta, kv, pol
    real*8, dimension(3) :: Apulse
    real*8 kr, wt, DxDt
    real*8 tmid
    common/center/tmid

    wt = w*(t-tmid)
    kr = dot(kv,r)
    DxDt = kr/norm(kv)/Dx - (t-tmid)/Dt
    Apulse =  ( AA*dcos(kr-wt)*dexp(-DxDt**2d0) )*pol
    Epulse = -AA*( w*dsin(kr-wt) + 2d0/Dt*DxDt*dcos(kr-wt) )*dexp(-DxDt**2d0)*pol
    Bpulse = -AA*( dsin(kr-wt) + 2d0/norm(kv)/Dx*DxDt*dcos(kr-wt) )*dexp(-DxDt**2d0)*cross(kv,pol)
RETURN
END


SUBROUTINE derivs(t,y,dydt)
    use vector_functions
    implicit none
    integer, parameter :: neq = 6
    real*8 t, y(neq), dydt(neq)
    real*8 evolution(neq)
    real*8 c, hbar, eps, pi, w0, q, mm, Gamma, Dw0, cohtime, a0, t0, Smtrix(3,3), Dmtrix(3,3)
    common/pra/ c, hbar, eps, pi, w0, q, mm, Gamma, Dw0, cohtime, a0, t0, Smtrix, Dmtrix
```

```
    real*8, dimension(3) :: Evac, Bvac
    common/vac_field/ Evac, Bvac
    real*8, dimension(3) :: Epulse, Bpulse
    common/pulse_field/ Epulse, Bpulse
    real*8, dimension(3) :: r, v
    real*8, dimension(3) :: F, Fspring, Fdamp, Fvac, Fpulse


    r = (/y(1),y(2),y(3)/)*a0
    v = (/y(4),y(5),y(6)/)*(a0/t0)

!   call vacfield(r,t*t0)   ! for FINAL CHECK
!   call pulsefield(r,t*t0) ! for FINAL CHECK


    Fspring = -mm*w0**2*r
    Fspring = matmul(Smtrix,Fspring)
    Fdamp = -mm*Gamma*w0**2*v
    Fdamp = matmul(Dmtrix,Fdamp)
    Fvac = q*Evac + q*cross(v,Bvac)*0d0
    Fvac = matmul(Smtrix,Fvac)
    Fpulse = q*Epulse + q*cross(v,Bpulse)*0d0
    Fpulse = matmul(Smtrix,Fpulse)
    F = Fspring + Fdamp + Fvac + Fpulse

    evolution = (/y(4),y(5),y(6),F*(t0**2d0/a0/mm)/)
    dydt = evolution
RETURN
END


!~~~~~~~~~~~~~~~~~~~~~~~~~~~~~~~~~~~~~~~~~~~~~~~~~~~~~~~~~~~~
!~~~~~~~~~~~~~~~~~~~~~~~~~~~~~~~~~~~~~~~~~~~~~~~~~~~~~~~~~~~~
SUBROUTINE odeint(ystart,nvar,x1,x2,eps,h1,hmin,nok,nbad,derivs,rkqs)
    INTEGER nbad,nok,nvar,KMAXX,MAXSTP,NMAX
    REAL*8 eps,h1,hmin,x1,x2,ystart(nvar),TINY
    EXTERNAL derivs,rkqs
    PARAMETER(MAXSTP=1000000000,NMAX=50,KMAXX=200,TINY=1d-30)
    !use MAXSTP=10 to get the solver running then increase to MAXSTP=10000
    INTEGER i,kmax,kount,nstp
    REAL*8 dxsav,h,hdid,hnext,x,xsav,dydx(NMAX),xp(KMAXX),y(NMAX),yp(NMAX,KMAXX),yscal(NMAX)
!   COMMON/path/kmax,kount,dxsav,xp,yp
    PARAMETER (dxsav=0.1d0,kmax=100)
    x=x1
    h=sign(h1,x2-x1)
    nok=0
    nbad=0
    kount=0
    do i=1,nvar
        y(i)=ystart(i)
    enddo
    if (kmax.gt.0) xsav=x-2d0*dxsav
    do nstp=1,MAXSTP
        call derivs(x,y,dydx)
        do i=1,nvar
            yscal(i)=abs(y(i))+abs(h*dydx(i))+TINY
!           yscal(i)=1d0
        enddo
        if(kmax.gt.0)then
            if(abs(x-xsav).gt.abs(dxsav))then
                if(kount.lt.kmax-1)then
                    kount=kount+1
                    xp(kount)=x
                    do i=1,nvar
```

```
                        yp(i,kount)=y(i)
                    enddo
                    xsav=x
                endif
            endif
        endif
        if((x+h-x2)*(x+h-x1).gt.0.)h=x2-x
        call rkqs(y,dydx,nvar,x,h,eps,yscal,hdid,hnext,derivs)
        if(hdid.eq.h)then
            nok=nok+1
        else
            nbad=nbad+1
        endif
        if((x-x2)*(x2-x1).ge.0.)then
            do i=1,nvar
            ystart(i)=y(i)
            enddo
            if(kmax.ne.0)then
                kount=kount+1
                xp(kount)=x
                do i=1,nvar
                    yp(i,kount)=y(i)
                enddo
            endif
            return
        endif
!pause -> write(6,*)
        if(abs(hnext).lt.hmin) write(6,*) "stepsize smaller than minimum in odeint"
        h=hnext
    enddo
!pause => write(6,*)
    write(6,*) "too many steps in odeint"
    return
END SUBROUTINE odeint

SUBROUTINE rkqs(y,dydx,n,x,htry,eps,yscal,hdid,hnext,derivs)
    INTEGER n,NMAX
    REAL*8 eps,hdid,hnext,htry,x,dydx(n),y(n),yscal(n)
    EXTERNAL derivs
    PARAMETER(NMAX=50)
    INTEGER i
    REAL*8 errmax,h,htemp,xnew,yerr(NMAX),ytemp(NMAX),SAFETY,PGROW,PSHRNK,ERRCON
    PARAMETER(SAFETY=0.9d0,PGROW=-0.2d0,PSHRNK=-0.25d0,ERRCON=1.89d-4)
    h=htry
    1 call rkck(y,dydx,n,x,h,ytemp,yerr,derivs)
    errmax=0.
    do i=1,n
        errmax=max(errmax,abs(yerr(i)/yscal(i)))
    enddo
    errmax=errmax/eps
    if(errmax.gt.1d0)then
        htemp=SAFETY*h*(errmax**PSHRNK)
        h=sign(max(abs(htemp),0.1d0*abs(h)),h)
        xnew=x+h
!pause -> write(6,*)
        if(xnew.eq.x) write(6,*) "step size underflow in rkqs"
        go to 1
    else
        if(errmax.gt.ERRCON)then
            hnext=SAFETY*h*(errmax**PGROW)
        else
            hnext=5d0*h
        endif
        hdid=h
```

```
        x=x+h
        do i=1,n
            y(i)=ytemp(i)
        enddo
        return
    endif
END SUBROUTINE rkqs

SUBROUTINE rkck(y,dydx,n,x,h,yout,yerr,derivs)
    INTEGER n,NMAX
    REAL*8 h,x,dydx(n),y(n),yerr(n),yout(n)
    EXTERNAL derivs
    PARAMETER(NMAX=50)
    INTEGER i
    REAL*8 ak2(NMAX),ak3(NMAX),ak4(NMAX),ak5(NMAX),ak6(NMAX),ytemp(NMAX),A2,A3,A4,A5,A6,B21, &
    & B31,B32,B41,B42,B43,B51,B52,B53,B54,B61,B62,B63,B64,B65,C1,C3,C4,C6,DC1,DC3,DC4,DC5,DC6
    PARAMETER(A2=0.2d0,A3=0.3d0,A4=0.6d0,A5=1.0d0,A6=0.875d0,B21=0.2d0,B31=3.0d0/40.0d0,&
    & B32=9.0d0/40.0d0,B41=0.3d0,B42=-0.9d0,B43=1.2d0,B51=-11.0d0/54.0d0,B52=2.5d0, &
    & B53=-70.0d0/27.0d0,B54=35.0d0/27.0d0,B61=1631.0d0/55296.0d0,B62=175.0d0/512.0d0, &
    & B63=575.0d0/13824.0d0,B64=44275.0d0/110592.0d0,B65=253.0d0/4096.0d0,C1=37.0d0/378.0d0, &
    & C3=250.0d0/621.0d0,C4=125.0d0/594.0d0,C6=512.0d0/1771.0d0,DC1=C1-2825.0d0/27648.0d0, &
    & DC3=C3-18575.0d0/48384.0d0,DC4=C4-13525.0d0/55296.0d0,DC5=-277.0d0/14336.0d0,DC6=C6-0.25d0)
    do i=1,n
    ytemp(i)=y(i)+B21*h*dydx(i)
    enddo
    call derivs(x+A2*h,ytemp,ak2)
        do i=1,n
        ytemp(i)=y(i)+h*(B31*dydx(i)+B32*ak2(i))
    enddo
    call derivs(x+A3*h,ytemp,ak3)
    do i=1,n
        ytemp(i)=y(i)+h*(B41*dydx(i)+B42*ak2(i)+B43*ak3(i))
    enddo
    call derivs(x+A4*h,ytemp,ak4)
    do i=1,n
        ytemp(i)=y(i)+h*(B51*dydx(i)+B52*ak2(i)+B53*ak3(i)+B54*ak4(i))
    enddo
    call derivs(x+A5*h,ytemp,ak5)
    do i=1,n
        ytemp(i)=y(i)+h*(B61*dydx(i)+B62*ak2(i)+B63*ak3(i)+B64*ak4(i)+B65*ak5(i))
    enddo
    call derivs(x+A6*h,ytemp,ak6)
    do i=1,n
        yout(i)=y(i)+h*(C1*dydx(i)+C3*ak3(i)+C4*ak4(i)+C6*ak6(i))
    enddo
    do i=1,n
        yerr(i)=h*(DC1*dydx(i)+DC3*ak3(i)+DC4*ak4(i)+DC5*ak5(i)+DC6*ak6(i))
    enddo
    return
END SUBROUTINE rkck

!~~~~~~~~~~~~~~~~~~~~~~~~~~~~~~~~~~~~~~~~~~~~~~~~~~~~~~~~~~~~
!~~~~~~~~~~~~~~~~~~~~~~~~~~~~~~~~~~~~~~~~~~~~~~~~~~~~~~~~~~~~
FUNCTION ran1(idum)
    INTEGER idum,IA,IM,IQ,IR,NTAB,NDIV
    REAL*8 ran1,AM,EPS,RNMX
    PARAMETER(IA=16807,IM=2147483647,AM=1.0d0/IM,IQ=127773,IR=2836,NTAB=32, &
                & NDIV=1+(IM-1)/NTAB,EPS=1.2d-7,RNMX=1.d0-EPS)
    INTEGER j,k,iv(NTAB),iy
    SAVE iv,iy
    DATA iv/NTAB*0/,iy/0/
    if(idum.le.0.or.iy.eq.0)then
        idum=max(-idum,1)
        do j=NTAB+8,1,-1
```

```
            k=idum/IQ
            idum=IA*(idum-k*IQ)-IR*k
            if(idum.lt.0)idum=idum+IM
            if(j.le.NTAB)iv(j)=idum
         enddo
         iy=iv(1)
    endif
    k=idum/IQ
    idum=IA*(idum-k*IQ)-IR*k
    if (idum.lt.0) idum=idum+IM
    j=1+iy/NDIV
    iy=iv(j)
    iv(j)=idum
    ran1=min(AM*iy,RNMX)
    return
END FUNCTION ran1
```

# Appendix E

# Plasmonic Antenna Work Highlighted in Annalen der Physik

Our work on the ultrafast temporal response of a plasmonic antenna is chosen to be the cover article in the 2013 February Issue of Annalen der Physik. An "Expert Opinion" by Otto Muskens is also written to highlight our work.

www.ann-phys.org

FEB | 2013

adp

# annalen der physik

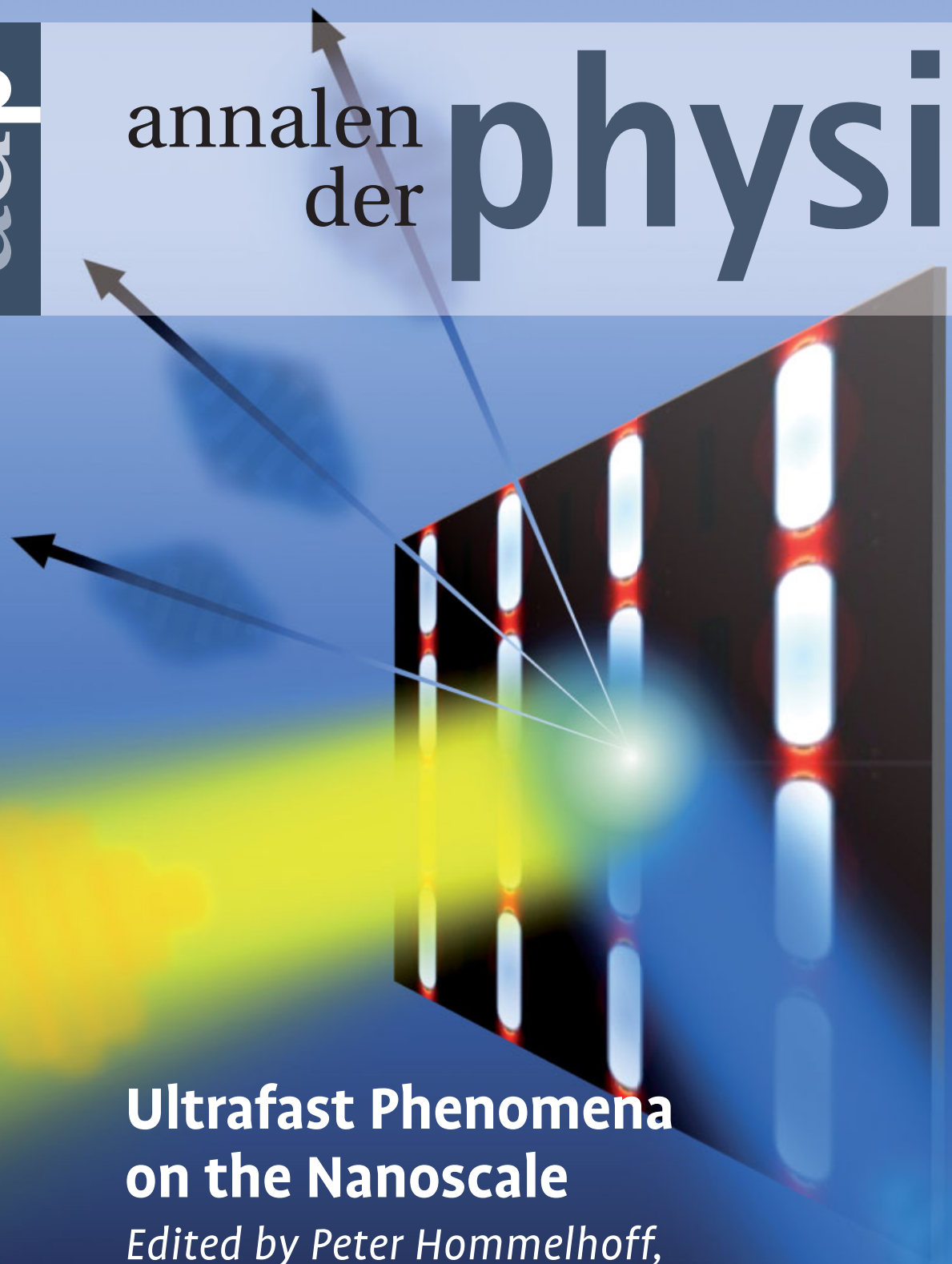

## Ultrafast Phenomena on the Nanoscale

*Edited by Peter Hommelhoff, Matthias Kling and Mark Stockman*

WILEY-VCH

ISSN 0003-3804 · Ann. Phys. (Berlin), 525, No 1-2 (February), 1-202 (2013)

Ann. Phys. (Berlin) **525**, No. 1–2, A21–A22 (2013) / DOI 10.1002/andp.201300706

annalen der physik



EXPERT OPINION

# Towards nanoantenna electron switches

*Otto Muskens*

The electromagnetic 'ponderomotive force' was discovered in 1957 in a radio-frequency experiment by Boot and Harvie [1]. The force arises due to gradients in an inhomogeneous oscillating electric field, and can be used to control and accelerate electrons, with applications in ion traps, plasma accelerators and high-harmonic generation. However, being a second-order nonlinear effect in the applied field, the ponderomotive force is relatively weak. The availability of high-power, short laser pulses has enabled new practical realizations of this effect [2].

In a Letter in this issue, Batelaan and co-workers predict that metal nanoantennas can produce sufficient ponderomotive force to deflect electrons [4]. The phenomenon relies on the surface plasmon resonance properties of the nanoantenna, which produces a high local field enhancement combined with large field gradients in a small volume around the nanoantenna. To achieve the required field strengths, they propose to use high energy laser pulses of femtosecond time duration, tuned to the surface plasmon resonance wavelength. These short laser pulses offer yet another advantage, as they allow producing an ultrafast modulation of an incident electron beam. Such an electron switch would be of interest for a range of applications, for example ultrafast electron microscopy [4]. Ultrafast electron microscopy is a powerful tool for characterizing chemical and physical processes at nanometer length scales and ultrafast time scales. Currently, the generation of ultrafast electron pulses is done by directly exciting the electron emission source with a high-power UV laser pulse. Plasmonic electron switches may be a feasibly alternative route toward the development of ultrafast electron beams at higher repetition frequencies and using lower-power femtosecond oscillators.

As a first step, the authors measured the coherence time of surface plasmon modes in an array of nanoparticles, so-called optical antennas [3]. A short, resonant laser pulse can drive a coherent plasmon oscillation, however this oscillation rapidly dephases via collisions of the electrons (intraband) or

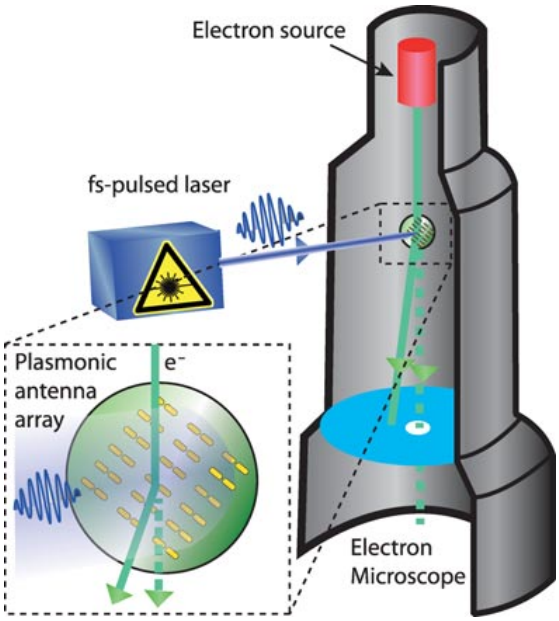


**Figure 1** (online color at: www.ann-phys.org)) Layout of an ultrafast electron microscope where a plasmonic antenna array is used as an ultrafast electron switch.

through excitation of electron-hole pairs (interband). Surface plasmons in isolated metal nanospheres have a dephasing time of several femtoseconds, depending on the type of metal antenna under study and details of the damping mechanism. Detailed measurements of plasmon dephasing were pioneered in the 1990s by Franz Aussenegg and coworkers, who used high harmonic generation as a nonlinear process to make an autocorrelation of the plasmon pulse [5]. High-harmonic generation in nanoparticles is complicated, since second-harmonic requires noncentrosymmetric structures, while third harmonic signals are comparably weak. Becker et al. use a different, more direct method of measuring both the amplitude and phase of the plasmon field using cross-correlation of the plasmon field with a reference pulse with known width taken directly from the laser.

The prospect of electron beam modulation using ultrafast plasmon fields is promising as a fundamental phenomenon and may further open up the field of ultrafast electron microscopy. Both the coherence time and local field enhancement can be tailored by the geometry of the nanoantenna, allowing for a rational design of nanostructures optimized for specific applications [6]. Of particular interest will also be the application of techniques from coherent control to achieve local plasmonic hot-spots in both space and time [7], potentially resulting in even stronger field gradients at shorter time scales. Several hurdles will have to be overcome, related to the high field strengths required and the breakdown of metal nanoantenna arrays under such high power excitation. Similar problems are encountered in higher-harmonic generation experiments, and require careful optimization of material properties of the antennas and substrate. However, if successful, the plasmonic antenna approach may result in a new generation of electron modulation devices.

*Otto Muskens*
*Quantum Light and Matter Group,*
*School of Phyics and Astronomy*
*University of Southampton, Highfield,*
*Southampton SO 17 1BJ, United Kingdom*
*E-mail: O.Muskens@soton.ac.uk*

## References

[1] H. A. H. Boot, R. B. R.-S. Harvie, Nature **180**, 1187 (1957).
[2] D. L. Freimund, K. Aflatooni, H. Batelaan, Nature **413**, 142–143 (2001).
[3] M. Becker, W. C.-W. Huang, H. Batelaan, E. J. Smythe, F. Capasso, Ann. Phys. (Berlin), **525**, L6–L11 (2013).
[4] O.-H. Kwon, A. H. Zewail, Science **328**, 1668–1673 (2010).
[5] B. Lamprecht, J. R. Krenn, A. Leitner, and F. R. Aussenegg, Phys. Rev. Lett. **83**, 4421 (1999).
[6] T. Hanke, J. Cesar, V. Knittel, A. Trügler, U. Hohenester, A. Leitenstorfer, R. Bratschitsch, Nano Lett. **12**, 992 (2012).
[7] M. Aeschlimann, M. Bauer, D. Bayer, T. Brixner, F. J. García de Abajo, W. Pfeiffer, M. Rohmer, C. Spindler & F. Steeb, Nature **446**, 301–304 (2007).